2015-07-01

Analytical Approaches in Investigating the Kinetics of Water-Molecule Complexes in Tropospheric Reactions

William J. Keeton
Brigham Young University - Provo

BYU ScholarsArchive Citation

Keeton, William J., "Analytical Approaches in Investigating the Kinetics of Water-Molecule Complexes in Tropospheric Reactions" (2015). *All Theses and Dissertations*. 5527.
https://scholarsarchive.byu.edu/etd/5527

Analytical Approaches in Investigating the Kinetics of Water-Molecule Complexes in Tropospheric Reactions

William J. Keeton

A thesis submitted to the faculty of
Brigham Young University
in partial fulfillment of the requirements for the degree of

Master of Science

Jaron C. Hansen, Chair
Steven R. Goates
Lee D. Hansen

Department of Chemistry and Biochemistry

Brigham Young University

July 2015

ABSTRACT

Analytical Approaches in Investigating the Kinetics of Water-Molecule Complexes in Tropospheric Reactions

William J. Keeton
Department of Chemistry and Biochemistry, BYU
Master of Science

Ozone is a heavily monitored pollutant. Ozone is not directly emitted into the atmosphere, but rather the product of chemical reactions. Ground level ozone occurs when nitrogen oxides (NO_x) and volatile organic compounds (VOCs) react with each other in the presence of sunlight. The primary precursors of ozone are anthropogenically emitted, and as a result, tropospheric ozone has cost millions of dollars in damages and has hurt the health of countless people.

This thesis is a collection of work that aims to provide insight into atmospheric reactions that result in tropospheric ozone and the instrumentation to study such reactions. While these reactions are well studied, this research is novel in its attempt to understand water vapor's influence in tropospheric ozone reactions. As the troposphere continues to get warmer and wetter from global climate change, water vapor will play a larger role in tropospheric reactions, which in turn may perturb the global reactions.

Work is presented on the self-reaction of β-hydroxyethyl peroxy radical (β-HEP), an ozone precursor, and the increase in reaction rate catalyzed by water vapor. β-HEP serves as a model system for understanding the roles of water vapor in perturbing the kinetics and product branching ratio of ozone forming reactions. The self-reaction rate coefficient of β-HEP was investigated between 274-296 K with 1.0×10^{15} to 2.5×10^{17} molecules cm^{-3} of water vapor at 200 Torr total pressure by slow-flow laser flash photolysis coupled with UV time-resolved spectroscopy and long-path, wavelength-modulated, diode-laser spectroscopy. The overall rate constant is expressed as the product of temperature-dependent and water vapor-dependent terms giving $k(T,H_2O) = 7.8 \times 10^{-14}(e^{8.2\ (\pm 2.5)\ \mathrm{kJ/RT}})(1 + 1.4 \times 10^{-34} \times e^{92\ (\pm 11)\ \mathrm{kJ/RT}}\,[H_2O])$. The results suggest that formation of a β-HEP-H_2O complex is responsible for the observed water vapor enhancement of the self-reaction rate coefficient.

A new discharge flow mass-spectrometer was engineered in collaboration with the California Institute of Technology and NASA's Jet Propulsion Laboratory. This instrument allows for rapid study of water vapor influence on the kinetics of atmospheric reactions. This instrument will be used in further studying the β-HEP + NO reaction as a function of water vapor concentration.

Keywords: discharge flow mass-spectrometer, atmospheric kinetics, ozone, β-hydroxyethyl peroxy

ACKNOWLEDGEMENTS

I would like to thank all the people who contributed in some way to the work described in this thesis. First and foremost, I thank my academic advisor, Dr. Jaron C. Hansen, for accepting me into his group. He contributed greatly to my rewarding graduate school experience by giving me intellectual freedom, engaging me in new ideas, and demanding high quality work in my endeavors. I would like to thank my committee members Dr. Steven R. Goates and Dr. Lee D. Hansen for their friendship, mentorship, and their interest in me as an individual and my work.

I owe a large part of the results described below to Dr. Stan P. Sander of NASA's Jet Propulsion Laboratory. He openly accepted me into his group, into his facilities, and provided me with the tools and funding necessary to succeed. I especially would like to Dr. Kyle D. Bayes. His enthusiasm and work ethic for research was contagious and motivational, and I am extremely grateful for the daily interaction and lessons he shared with me.

In regards to the Hansen group, I would like to thank Taylor Cline, Paul Cropper, Sambhav Kumbhani, Marie Killian, Joseph Mosley, Braden Myers, and Emily Burrell for providing a great work environment. I am thankful for the BYU Chemistry Department, Janet Fonoimoana, Sue Mortensen, Peggy Erickson, Dr. Steven G. Wood, and the entire faculty that contributed to my graduate school experience.

Finally, I would like to thank my parents, Ken and Maria. Their sacrifices are uncountable, and their love unsurpassable. I thank my siblings for making me who I am today. And lastly, I thank my beautiful wife, Brooke. She has always believed in me and has sacrificed much of her own career to help pursue my own.

TABLE OF CONTENTS

LIST OF TABLES

LIST OF FIGURES

1 INTRODUCTION

1.1 The Atmosphere and Us

In the cold London December of 1952, a series of events lead to the death of almost 12,000 people.[2] No shots were fired, no knives were brandished, and in the end the culprit was themselves. The Great London Smog of 1952 came to be known as the worst air-pollution event in the United Kingdom. The cold air and windless conditions allowed fog to condense near the ground. The fog then mixed with domestic smoke, factory emissions, and vehicular exhaust. Normally the fog and pollutants would rise and be dispersed in the upper atmosphere, but the cold temperatures kept the fog near the ground. Over a four day period, the trapped airborne pollutants killed thousands of people.

At the time, pollution was not a new concept; however, the Great Smog showed that pollution can be deadly. This event impacted science, public perception, and government regulations in regards to pollution and the atmosphere. Since then, scientists have learned much more about the causes and impacts of atmospheric pollution. A pioneer in photochemistry, Philip Leighton,[3] stated:

> "One of the most striking developments of the past decade, both in the field of air pollution and in that of atmospheric chemistry, has been the recognition that photochemical reactions, produced by sunlight, may convert relatively innocuous

> pollutants into substances which constitute a nuisance, create a possible health hazard, and cause economic loss to man"

The chemistry of the atmosphere is complex and varies with location, altitude, season, geology, and human activity. The ability to solve or prevent pollution is dependent upon the understanding of these atmospheric reactions. Furthermore, some solutions are not universal. Solutions to pollution problems in Utah may not apply to problems in Los Angeles, and vice versa. There needs to be an understanding of local atmospheric chemistry, along with the measurement of local pollution sources. To integrate strategies for air pollution effectively, policy makers need extensive information about key pollutants and their interactions in the atmosphere.

1.2 National Ambient Air Quality Standards

In 1963, the United States Congress voted in the Clean Air Act, which commissioned research into tropospheric pollution. In 1970, this act was further amended to consolidate all federal research, monitoring, enforcement, and standard-setting into one agency, the Environmental Protection Agency (EPA). Since then, the EPA has set the National Ambient Air Quality Standards (NAAQS) for six pollutants.[4] These pollutants include carbon monoxide, lead, nitrogen dioxide, ozone, particulate matter, and sulfur dioxide. Standards are set for these pollutants, both as primary and secondary emissions. Primary emissions affect public health, including asthmatics, children, and the elderly. Secondary emissions also disrupt public health, along with plants, animals, buildings, and visibility. States and areas that fail to maintain the NAAQS are declared, "nonattainment areas," and are required by law to develop plans to meet those standards or lose government funding. These plans to attain or maintain NAAQS are known as State Implementation Plans (SIPs).[5] In order to develop realistic SIPs, policy makers must understand the chemical formation and loss mechanisms of the six pollutants. This thesis aims to contribute to both the kinetic modeling and sampling of ozone; one of the criteria pollutants.

1.3 Ozone

The discovery of ozone dates back over 150 years. Ozone was discovered in 1840 when Schonbein[6] noticed a distinct smell during the electrolysis of water, and named the substance ozone after the Greek word "ozein" for smell. Previous scientists had noted a similar smell after lightning struck or the smell between two arcing electrodes. These smells were thought to be the result of electricity and not a chemical reaction.[7] It wasn't until Leighton's work in the mid-1900s that ozone was attributed to the ozone layer and ozone pollution in the troposphere.[8]

Ozone is a unique molecule. In the stratosphere, ozone protects living organisms from deep UV-light ($\lambda < 300$nm). But, in the lower troposphere, ozone is a harmful pollutant. Ozone is a strong oxidizer, harming both human health and vegetation. Inhalation of ozone temporarily decreases lung capacity, inflames the airways, and makes people more susceptible to allergens.[9] The EPA characterizes the symptoms of ozone inhalation as coughing, respiratory irritation while breathing deeply, and shortness of breath.[4] Children exposed to ozone, have an increase of respiratory problems not only as kids, but as adults.[10] One recent study concluded that ozone exposure has greater medium- to long-term effects on subjects than short-term affects.[11] Ozone may also harm the growth of lungs in children.[9] In a study of 95 urban communities in the

United States over 13 years,[12] mortality rates increased with increased ozone levels, particularly cardiovascular and respiratory mortality.

Ozone also harms vegetation and decreases crop yield. Ozone slows photosynthesis and causes physical damage to the plant tissue. Forest areas near large cities, such as Los Angeles and Mexico City, show growth decline and visible damage from elevated ozone levels.[13] The physical damage changes the appearance of plants, decreasing their economic value, especially of horticultural crops.[14] In 2000, 79–121 million metric tons of crops were globally lost to ozone, a $11 – 18 billion loss to the economy.[15] In was estimated that ozone reduced the yield of the soybean crop by 8.5–14%, the wheat crop by 3.9–15%, and the maize crop by 2.2–5.5%. In another study, Avnery et al.[16] predict that crop yields will continue to decrease due to ozone damage, with a projected annual global loss of $12 – 13 billion in 2030.

1.4 Peroxy Radicals and the HO_x and NO_x Cycles

Tropospheric ozone is the byproduct of the HO_x and NO_x cycles.[17] Ozone episodes were first noticed in the 1940s in Los Angeles. The pollution of Los Angeles was strongly oxidizing, eye-watering, and plant killing. These pollution episodes occurred mostly at midday with warm temperatures and bright sunshine. The 1950s produced significant achievements in understanding the role of radical chemistry on ozone production. The importance of peroxy radical (RO_2) chemistry was established in the late 1970s, and forms the basis of the HO_x and NO_x cycles.[18] The formation of peroxy radicals by either of these pathways sets in motion the HO_x and NO_x cycles.

Although N_2, O_2, and Ar make up 99.96% of the Earth's atmosphere, the concentrations of trace species drive the pollution mechanisms in the atmosphere. The lower atmosphere can be thought of as a low temperature combustion system initiated through photochemistry.[19] The photolysis of trace species initiates radical propagation, terminating in closed-shell species that pollute the atmosphere. Free radicals have extremely high reactivity and accordingly have short lifetimes and, therefore, are found in the troposphere at concentrations typically less than 100 parts per trillion. Their high reactivity causes the chemistry of the troposphere to be complex, but can be simplified by discovering common reactions for the removal of organics found in the atmosphere. Two prominent cycles that are commonly used to model the troposphere are the HO_x cycle (the reactions governing the radicals OH, HO_2, and hydrogen atoms) and the NO_x cycle (the reactions describing the interconversion of NO and NO_2). These cycles are interconnected but discussed separately here.

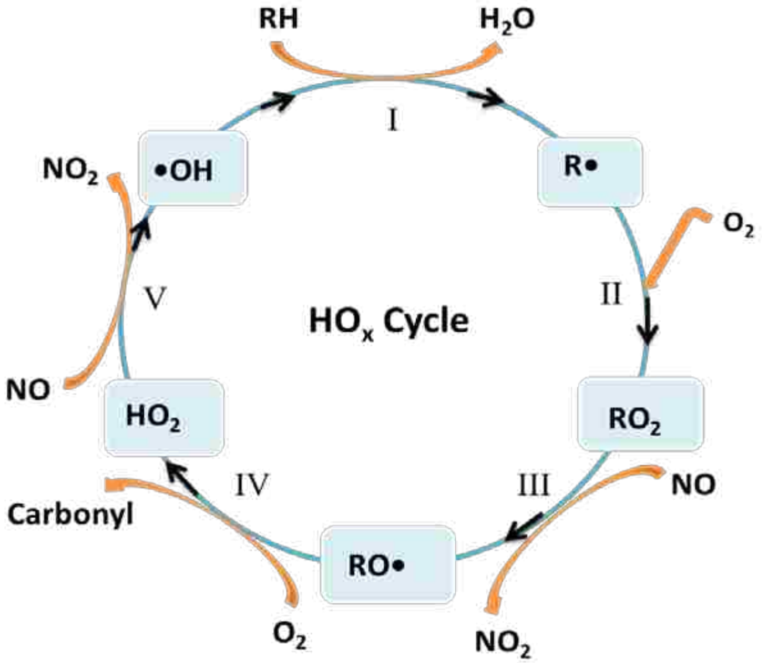

Figure 1.1 - The HO_x cycle (Author original)

The HO_x cycle is depicted schematically in Figure 1.1. The initiator of this cycle is the hydroxyl radical (OH) initially formed by photolysis of ozone in the presence of water.[20]

$$O_3 + hv(\lambda < 320\text{nm}) \rightarrow O(^1D) + O_2(^1\Delta g) \qquad (1.1)$$

$$O(^1D) + H_2O \rightarrow OH + OH \qquad (1.2)$$

OH concentrations typically range from less than 1×10^4 molecules cm^{-3} at night to approx. 3×10^6 molecules cm^{-3} at midday.[21] OH predominately reacts with CO to form hydrogen atoms that add to O_2 to form HO_2.

$$OH + CO \rightarrow CO_2 + H \qquad (1.3)$$

$$H + O_2 \rightarrow HO_2 \qquad (1.4)$$

Organic species, whether from biogenic or anthropogenic sources, are removed from the troposphere by reaction with OH, creating an alkyl radical (R).

$$OH + RH\ (\text{Organics}) \rightarrow H_2O + R \qquad (1.5)$$

With 21% of the atmosphere being O_2, the only significant reaction of alkyl radicals is the addition of O_2 to form peroxy radicals.

$$R + O_2 \rightarrow RO_2 \qquad (1.6)$$

RO_2 and the peroxy radical, HO_2, are found in concentrations from 0.2 - 2.5 × 10^8 molecules cm^3.[20] These molecules react with themselves and with each other, especially in pristine environments (low NO_x). The self-reaction of one of the most prominent peroxy radicals, $HOCH_2CH_2O_2$, is the focus of the research in Chapter 2. In more polluted conditions (high NO_x) the self-reactions of peroxy radicals compete with the reaction with NO to oxidize NO to NO_2 and produce an alkoxy radical (RO).

$$RO_2 + NO \rightarrow RO + NO_2 \qquad (1.7)$$

Reaction 1.7 has a second minor pathway that produces an organic nitrate ($RONO_2$) and is the focus of the research described in chapter 3. Alkoxy radicals react with O_2 to form HO_2 and a carbonyl containing compound.

$$RO + O_2 \rightarrow HO_2 + \text{Carbonyl Compound} \qquad (1.8)$$

The carbonyl compound formed will depend on the R group of the original organic molecule, but often form aldehydes. Many aldehydes are known to photolyze in the daytime to produce many other radical-chain pathways. Other carbonyl compounds are oxidized by OH as the HO_x cycle continues. The cycle completes back to where it started when HO_2 is reduced by oxidizing NO to NO_2.

$$HO_2 + NO \rightarrow OH + NO_2 \qquad (1.9)$$

Chain termination occurs with peroxide formation from the self-reaction of HO_2 and in many cross reactions of RO_2.

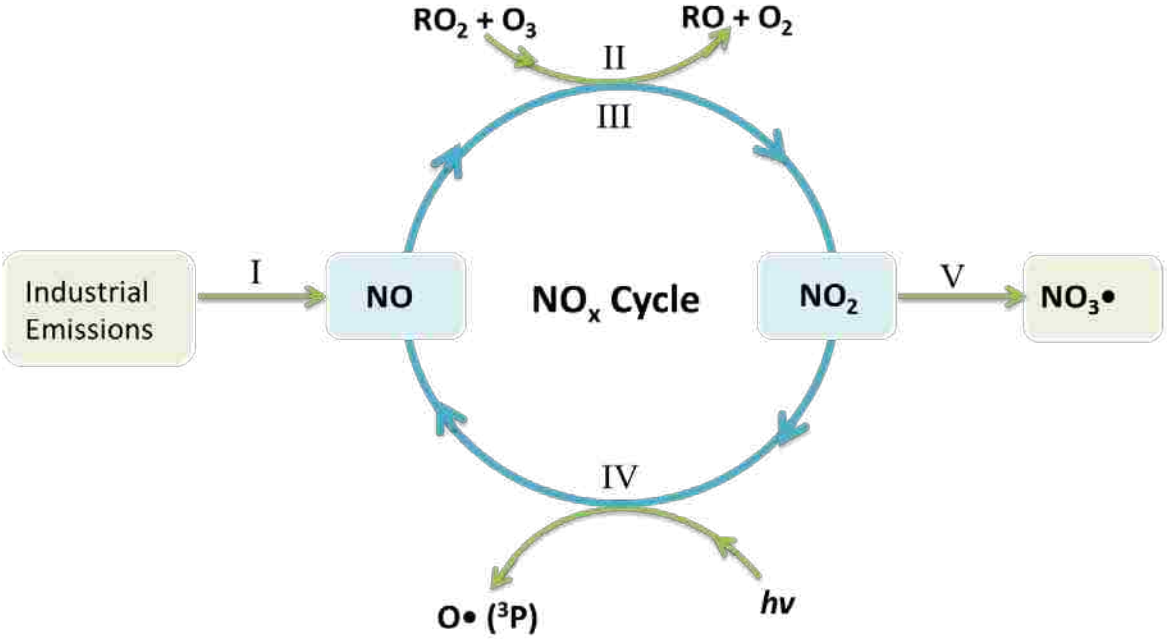

Figure 1.2 - The NO_x Cycle (Author Original)

The NO_x cycle is depicted as a schematic in Figure 1.2. This cycle is initiated by the emission of NO into the troposphere. NO and NO_2 are formed when N_2 and O_2 are present together at elevated temperature ($T > 2800$ °F), which commonly occurs in internal combustion engines and power plant boilers. As previously mentioned, Reactions 1.7 and 1.9 oxidize NO to NO_2. Additionally, ozone may oxidize NO to NO_2, but at slower rates. NO_2 is readily photolyzed to form a radical oxygen that subsequently forms ozone.[22]

$$NO_2 + h\nu\ (\lambda < 410\text{nm}) \rightarrow NO + O(^3P) \qquad (1.10)$$

$$O(^3P) + O_2 + M \rightarrow O_3 + M \qquad (1.11)$$

This reaction is the predominant mechanism for tropospheric ozone formation.[20] For every carbon in a hydrocarbon that passes through the HO_x cycle, two molecules of ozone are formed. As the sun sets and the supply of OH is depleted, these cycles do not terminate because of night-time chemistry. NO_2 is no longer photolyzed at night but can react with ozone to form the nitrate radical (NO_3).

$$NO_2 + O_3 \rightarrow NO_3 + O_2 \qquad (1.12)$$

Nitrate subsequently takes the role of OH in the HO_x cycle in oxidizing hydrocarbons through hydrogen abstraction to alkyl radicals. Nitrate chemistry ceases at dawn because of its large absorption cross section of visible light and high photolysis yield.[23]

1.5 Water Vapor

Many of these tropospheric reactions that lead to ozone formation have been thoroughly studied; however, these reactions have not been investigated in the presence of water vapor. Water molecules have the ability to complex with atmospheric molecules via hydrogen bonds. The H_2O molecule then acts as a third body, and possibly alters the kinetics and branching ratios of tropospheric ozone forming reactions.

1.6 Layout of Thesis

Chapter 2 is a published work, while chapters 3 and 4 are supplemental work that is currently being prepared for publication. Chapter 2 details the work done on the kinetics of the self-reaction of β-hydroxyethyl peroxy radicals in the presence of water vapor. Chapter 3 constitutes the principle focus of this thesis, and outlines the engineering of an instrument capable of measuring the kinetics and product branching ratio of key atmospheric reactions. Chapter 3 outlines future applications of the instrument discussed in Chapter 3, specifically the application in studying the β-hydroxyethyl peroxy radical + NO reaction in the presence of water vapor.

2 WATER VAPOR ENHANCEMENT OF RATES OF PEROXY RADICAL REACTIONS

2.1 Disclaimer

The work presented in this chapter has been accepted by the International Journal of Chemical Kinetics. It is be presented in its entirety.

2.2 Abstract

Peroxy radicals can complex with water vapor. These complexes affect tropospheric chemistry. In this study, β-HEP (hydroxyethyl peroxy radical) serves as a model system for investigating the effect of water vapor on the kinetics and product branching ratio of the self-reaction of peroxy radicals. The self-reaction rate coefficient was determined at 274–296 K with water vapor between 1.0×10^{15} and 2.5×10^{17} molecules cm^{-3} at 200 torr total pressure by slow-flow laser flash photolysis coupled with UV time-resolved spectroscopy and long-path, wavelength modulated, diode-laser spectroscopy. The overall self-reaction rate constant expressed as the product of both a temperature dependent and water vapor dependent term is $k_o = 7.8 \times 10^{-14} exp((8.3 \pm 2.5\ kJ/mol)/RT) + \{(13.2 \pm 1.56) \times 10^{-44} \times exp((79.3 \pm 17.18\ kJ/mol)/RT) \times [H_2O]\}$ suggesting formation of a β-HEP-H_2O complex is responsible for the increase in the self-reaction rate coefficient with increasing water concentration. Complex formation is supported by computational results identifying three local energy minima for the β-HEP-H_2O complex. As the troposphere continues to get warmer and wetter, more of the peroxy radicals present will be complexed with water. Investigating the effect of water vapor on kinetics

of atmospherically relevant radicals and determining the effects of these altered kinetics on tropospheric ozone concentrations is thus important.

2.3 Introduction

A direct relationship has been established between surface temperature and tropospheric water vapor. As the Earth continues to warm and tropospheric water vapor increases, water mediated chemistry has the potential to perturb the chemistry of the troposphere.[24] Organic peroxy radicals (RO_2) are intermediates in the oxidation of hydrocarbons and are precursors for tropospheric ozone formation.[25] This work provides experimental evidence for an increased self-reaction rate of the organic peroxy radical, hydroxyethyl peroxy radical (β-HEP; $HOCH_2CH_2O_2$), in the presence of water vapor. β-HEP is a derivative of ethylene and plays a significant role in tropospheric chemistry. Ethylene is released both naturally from vegetation and from combustion of wood and fossil fuels with an estimated total emission of 18–25 Tg yr^{-1}.[26] A typical urban environment contains 50 μg m^{-3} of ethylene with peak concentrations up to 1000 μg m^{-3} during high traffic hours, whereas rural environments range from 1–5 μg m^{-3}. As the troposphere continues to get warmer and wetter, more complexes with water will form, which in turn may perturb the kinetics and product branching ratios of atmospherically important reactions. For example, all unsaturated hydrocarbons will add OH across the double bond, and the addition of O_2 will produce β-hydroxy peroxy radicals. Isoprenes and terpenes are two major examples of biogenic sources that will produce β-hydroxy peroxy radicals. If β-HEP demonstrates a self-reaction rate enhancement, we hypothesize that peroxy radicals formed from other unsaturated hydrocarbons will also show enhanced rates with water vapor.

In 1975, Hamilton[27] discovered that water vapor increases the self-reaction rate of hydroperoxy radical (HO_2). Since then, numerous studies have verified and refined the findings of this first study.[28-32] The complete rate expression, including the temperature and pressure dependence of this reaction, was published in 1984.[30] More recent studies have evaluated the equilibrium constant for formation of the HO_2-H_2O complex as well as the rate enhancement by NH_3 and CH_3OH.[33] Hamilton's original work stated that enhancement of the HO_2 self-reaction rate occurs with polar gases and hypothesized that the increased reaction rate was caused by formation of a complex between HO_2 and H_2O. Existence of an HO_2-H_2O complex has since been experimentally verified by Suma *et al.*[34]

The catalytic effect of water has been discussed at length without agreement on a general theory for predicting a change in the rate of specific reactions in response to changes in water vapor concentration.[35-37] Stockwell[38] modeled the water vapor enhancement of the HO_2 self-reaction as it affects atmospheric HO_x and O_3 budgets, and predicted decreased concentrations of HO_2 and H_2O_2 under saturated water conditions and thereby decreasing the O_3 concentration. The concentrations of O_3 and HO_x were previously overestimated by as much as 75% at the surface and 30% at 10 km. Butkovskaya *et al.*[39] recently showed that 50% relative humidity (4×10^{17} molecules cm^{-3} at 298 K), displaced the branching ratio of the reaction of $HO_2 + NO$ away from NO_2 production and increased the production of HNO_3 by 800%. They hypothesized that a water molecule complexed to HO_2 serves as an energy sink and consequently drives formation of HNO_3 at the expense of OH and NO_2.

Although the HO_2 self-reaction rate is increased by water, water has no measurable effect on the self-reaction rate of methyl peroxy radical (CH_3O_2) or the reaction of $CH_3O_2 + HO_2$.[37] The absence of catalysis by water is explained by the small fraction of CH_3O_2 complexed with water owing to the small binding energy, calculated to be 8.8 kJ mol^{-1}. At 100% relative humidity and 298 K, the percentage of CH_3O_2-H_2O complex is only 0.02%, substantially less than the 8–15% calculated for the HO_2-H_2O complex,[40] which is calculated to be bound by 28.9 kJ mol^{-1}. This is comparable to the binding energy calculated for the β-HEP-H_2O complex (27.4 kJ mol^{-1}). Recent computational work[41] indicates that other alkyl peroxy radicals can also complex with water vapor. Khan *et al.*[42] in a recent atmospheric global modeling study using the STOCHEM-CRI model, predicted that as much as 17% of peroxy radicals in the upper troposphere can exist as complexes.

β-HEP serves as a model system for investigating the possible role of water vapor in perturbing the kinetics and product branching ratios of other alkyl peroxy radicals. For water vapor enhancement to be observed, a significant portion of reactants must form a radical-molecule complex.[43] β-HEP is chosen as a model radical to test the theory that strongly hydrogen-bonded complexes increase the rate of self-reaction. Clark *et al.*[41] demonstrated that the optimized structure predicted for the β-HEP-H_2O complex is stabilized by the formation of two intermolecular hydrogen bonds, as is the HO_2-H_2O complex. The self-reaction rate constant of β-HEP has previously been established in several studies.[44-49] However, the kinetics of the effects of water vapor on the self-reaction of β-HEP has not been studied. Khan *et al.*[42] concluded in their modeling study "the reaction between $RO_2.H_2O$ and NO, RO_2/HO_2 are worthy of investigation."

This study presents experimental evidence for the catalytic effect of water vapor on the β-HEP self-reaction. We derive an empirical equation from experimental measurements expressing the β-HEP self-reaction rate constant as a function of temperature and water vapor. High level *ab initio* calculations are used to calculate the equilibrium constant for the formation of the β-HEP-

H_2O complex. The temperature range and water vapor concentrations were chosen because of their significance to conditions in the troposphere.

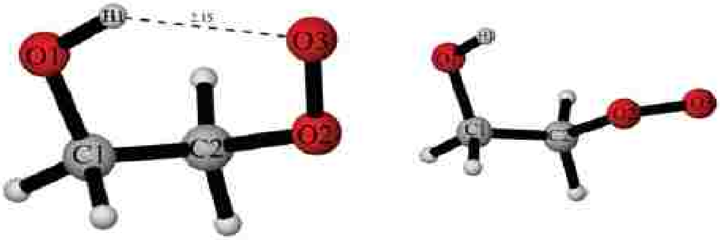

Global minimum

Local minimum

Figure 2.1- Optimized geometries of β-HEP. The bond length is reported in angstroms.

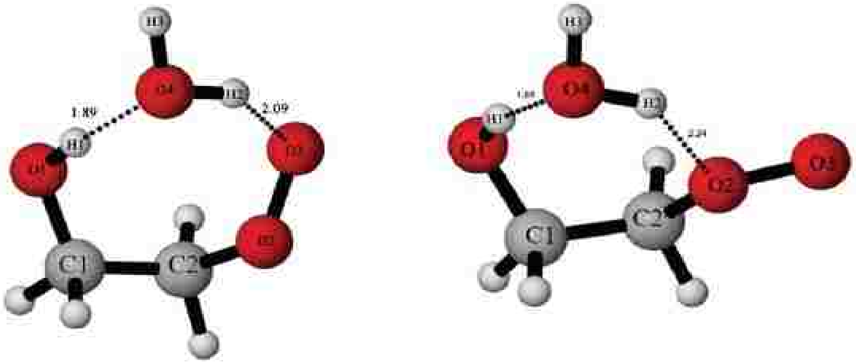

Global Minimum

Local Minimum 1

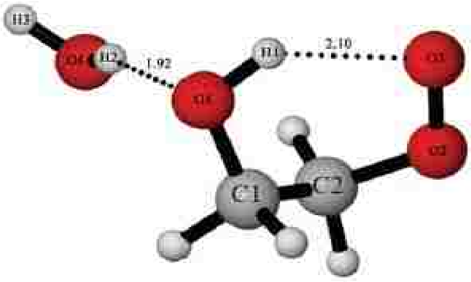

Local Minimum 2

Figure 2.2- Optimized geometries of β-HEP-H_2O complex. Bond lengths are reported in angstroms.

2.4 Methods

2.4.1 Computational Methods

Gaussian 03[50] was used to compute the equilibrium constant for complexation of β-HEP with H_2O. Both harmonic and anharmonic vibrational frequencies and rotational constants of both the β-HEP molecule and the β-HEP-H_2O complex were optimized with the B3LYP/aug-cc-pVDZ method and basis set. The energies were refined by performing single-point energy calculations with the MP2 and CCSD(T) methods. One global minimum and one local minimum structure were identified for the β-HEP molecule. These structures are shown in Figure 2.1. One global and two local minima energy structures for β-HEP-H_2O (Figure 2.2) complex were identified by Gaussian optimizations through Random Constrained Sampling (RCS) methodology[36] (see Figure 2.2). The energies of each local and global minimum energy structure were zero-point energy corrected and basis set superposition error corrected[51] from energies calculated with the B3LYP/aug-cc-pVDZ method and basis set in Gaussian 03. All local minima with energies within *k*T (2.5 kJ/mol) of the global minimum geometry have measurable probability of being populated at room temperature, and therefore all the geometries were used in the equilibrium constant calculation. Additional details about the partition function calculations and equilibrium constant calculations[52] are reported in Supplemental material section S-1.

2.4.2 Instrumentation

Figure 2.3 shows the principal components and layout of the experimental apparatus. The photolysis cell is 244 cm long including the end boxes (20 cm × 18 cm) used to house long-pass Herriott cell optics. The end boxes support the glass photolysis cell and are purged with nitrogen to protect optical surfaces from corrosive gases. The Pyrex cylindrical reaction tube (187 cm in length, 5.1 cm in diameter) between the end boxes constitutes the effective path length for zphotolysis and absorption experiments. The reaction tube is surrounded by a Pyrex jacket through which methanol, or a glycol/water mixture is circulated for temperature regulation. z All gases are precooled or heated before entering the reaction cell by a jacketed long-path manifold that is either cooled with methanol or heated with a glycol/water mixture. K-type thermocouples placed at both ends of the cell monitor the temperature of the system. Typically, less than 1°C difference occurs between the gases entering and exiting the cell. CaF_2 windows are used at both ends of the cell to transmit both UV and IR light over the range of interest. Kinematically mounted mirrors in the optical path of the system make it possible to switch between UV and IR detection methods without changing the position and alignment of the flow cell, light sources and detectors. A purge box placed over the IR and UV optics in the path where

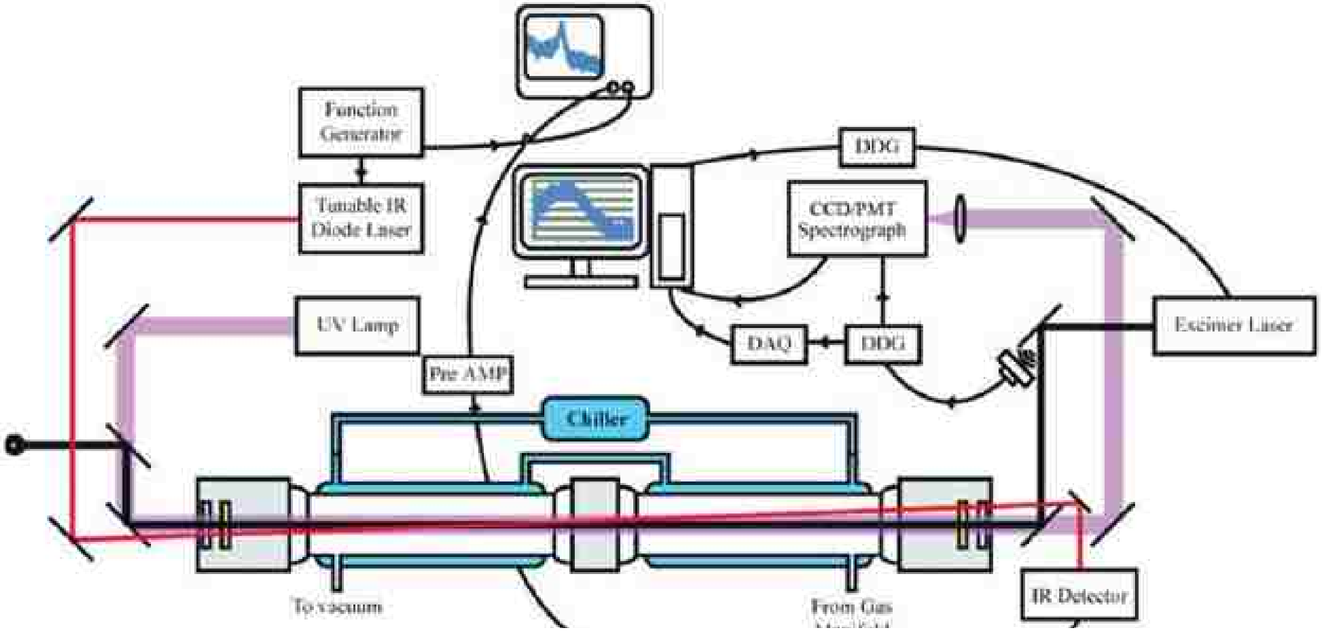

Figure 2.3- Schematic of UV/flash-photolysis system for kinetic measurements.

the excimer-light and D_2-light intersect is purged with a steady flow of nitrogen to reduce production of ozone formed by photolysis of O_2 outside the cell by the excimer laser. Gas mixtures of N_2/O_2/2-chloroethanol/H_2O flow continuously through calibrated Teledyne-Hastings (HFC series) flow controllers at a total flow rate of 14,000 standard cm^3 min^{-1} (sccm). 2-chloroethanol (99% pure) was purchased from Aldrich and used without further purification. Compressed N_2 and O_2 cylinders (99%) were obtained from Airgas. Pressure was maintained at 200 Torr total pressure and measured with an MKS-Baratron 690A pressure transducer.

2.5 Measurements

2.5.1 Radical Generation and Measurement

Flash photolysis/UV absorption spectroscopy was used to create and monitor β-HEP. β-HEP was formed in the reaction cell by introducing a gas mixture containing typically 6.1×10^{18} molecules cm^{-3} of N_2, 6.6×10^{17} molecules cm^{-3} of O_2, and $1{-}6\times10^{15}$ molecules cm^{-3} of 2-chloroethanol ($HOCH_2CH_2Cl$). $HOCH_2CH_2Cl$ was introduced into the gas mixture via dual 100-mL bubblers in series with N_2 at 2000 sccm as the carrier gas. The amount of $HOCH_2CH_2Cl$ is approximate, other gases were metered. Two bubblers in series provide time for carrier N_2 to be saturated with $HOCH_2CH_2Cl$. The temperature of the bubblers was maintained by immersion in a constant temperature bath maintained at 303 K through use of resistive heaters and a PID controller. Total flow rate was maintained at 14,000 sccm, resulting in a residence time of ~4 s in the reaction cell. A 15 ns pulse from the ArF excimer laser (LamdaPhysik, model EMG201MSC) at 193 nm and energy of 200 to 400 mJ $pulse^{-1}$ photolyzes an area 2.5 cm wide by 1 cm high. The excimer was fired at 0.33 Hz, allowing for a mostly fresh (~95%) mixture of gas to be probed with every laser shot. The pulse photolyzed a small fraction of the $HOCH_2CH_2Cl$

molecules to produce $HOCH_2CH_2$ and Cl radicals.[48, 53] Subsequent reaction of $HOCH_2CH_2$ radical with O_2 produced the β-HEP radical. The initial measured concentration of β-HEP radical is 3–6×10^{13} molecules cm^{-3} depending on the concentration of $HOCH_2CH_2Cl$ and the intensity of the excimer laser pulse. Along with β-HEP formed by the cleavage of the C-Cl bond in $HOCH_2CH_2Cl$, trace amounts of derivatives of β-HEP are made by dissociation of a C-H or C-O bond in $HOCH_2CH_2Cl$. Based on the bond dissociation energies for C-H, C-O and C-Cl bonds in $HOCH_2CH_2Cl$, other peroxy radicals including $ClCH(O_2)CH_2OH$, $ClCH_2CH(O_2)COH$ and $ClCH_2CH_2O_2$ are < 0.01% of the β-HEP radical concentration.

Time-resolved detection of the β-HEP radical is done by directing the output from a 30-Watt D_2 lamp (Oriel model 60010) through the center of the reaction cell. The excimer laser photolysis beam is aligned coaxially with the UV probe beam using dielectric mirrors that reflect a 30-nm wide band centered on the 193 nm photolysis beam while passing all other UV wavelengths. UV light absorption is detected by a monochromator (Andor model SR-303i-B with a 1800 mm^{-1} or 600 mm^{-1} grating, depending on the light intensity, which decreases with decreasing wavelength in the D_2 lamp), and either an intensified and gated CCD camera (Andor model CCD30-11) or a photomultiplier tube (PMT Sens-Tech P30A-14).

The CCD was used in exploratory experiments to identify the major species present. The CCD measured absorption over a wide wavelength range, from 220 to 350 nm, enabling identification of secondary chemistry products. Absorption data at many wavelengths permits a least-squares fit to determine multiple species present in the reaction cell. Time resolved data were collected with the CCD by varying the delay from 1 to 10 ms after the excimer laser was fired. The CCD integrated a 5 μs window after the laser was fired, and 500 shots of the laser were averaged to achieve a sufficient signal-to-noise ratio. These experiments are timeconsuming because measurement of a decay of β-HEP requires a minimum of 30 delay times to achieve a reproducible fit. At 0.33 Hz, 12 h are needed to obtain a single fit to the self-reaction decay.

Because of the fast response, the kinetic data for the β-HEP self-reaction reported here were collected exclusively with the PMT. The PMT together with a monochromator and notch filters with selected wavelengths of 220, 230, and 254 nm (Figure 2.4 adapted from previously published data[47, 54, 55]) were used to collect kinetic data. The PMT collected data at 30 MHz after the excimer laser was fired. Deconvolution of species concentrations from the total absorption data collected by the PMT requires a decay curve to be collected at each of the three wavelengths. Sufficient signal to noise was obtained by averaging 300–400 shots of the excimer laser. Dark counts were recorded before each shot, and I_0 was taken as the signal prior to the next laser pulse. Collection of dark counts, blank (I_0) and response (I) was controlled through a LabVIEW routine written in-house.

After collecting decay curves at each of the three wavelengths, recommended cross sections were used from the MPI-Mainz UV-VIS spectral atlas of gaseous molecules[54] to determine concentrations of O_3, HO_2 and β-HEPby a least-squares fit (See supplemental material Section S-2). The β-HEP self-reaction rate constants and β-HEP concentration at time zero were obtained by fitting time-dependent concentrations to a system of differential equations defined by the reactions listed in Table 1.

2.5.2 Water Vapor Generation and Measurement

Water vapor was introduced into the reaction cell by passing N_2 carrier gas through a bubbler immersed in a constant temperature bath. The amount of water vapor in the reaction cell was controlled by both the temperature of the water and the percentage of total flow of the carrier gas passing through the bubbler. The water vapor concentration was varied between 1.0×10^{15} and 2.3×10^{17} molecules cm^{-3}. Water vapor concentration was held constant during each experiment, varying no more than ±8% over the 8 h duration of an experiment.

Wavelength modulated IR diode laser spectroscopy was used to quantify the water vapor in the cell. Figure 2.3 shows the IR system components. IR light was scanned over a narrow frequency band (100 Hz) centered at the 6790.65 cm^{-1} line such that the entire peak of the selected rovibrational transition of water vapor was observed. The IR beam was produced by a New Focus TLB-6326 tunable diode laser with a line width of < 300 kHz. With the use of Herriott cell optics, the IR beam was passed five times through the reaction cell and finally directed towards an IR 1-GHz low-noise photoreceiver (New Focus 1611). The signal from the detector was synchronized with the 100 Hz modulation frequency and visualized and recorded by a digital oscilloscope (TeKtronix model TDS 3024B). Data were processed and converted from absorption measurements to concentrations with a LabVIEW routine. Absorption line strengths were obtained from the HITRAN[56] database and converted to cross sections.

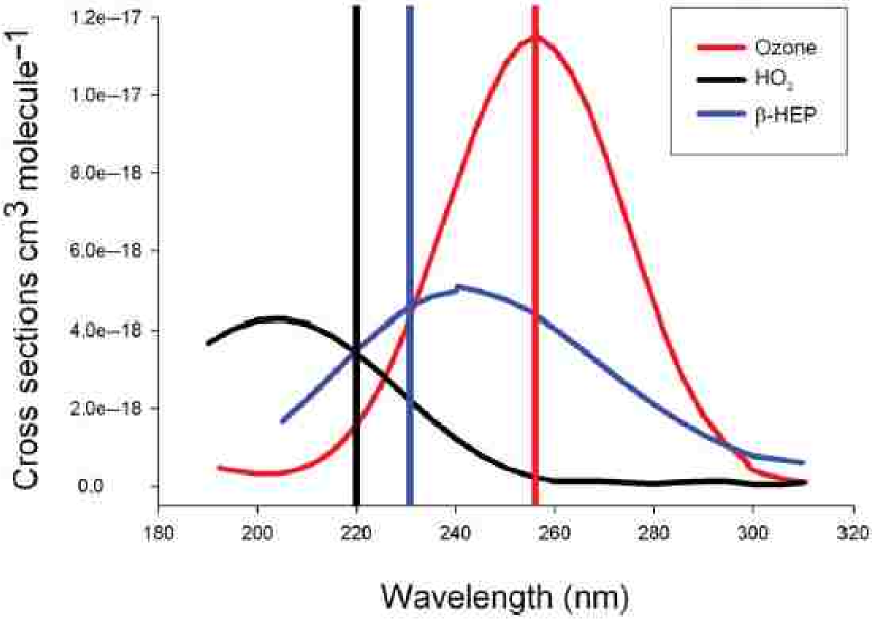

Figure 2.4- Plot of absorption cross sections of β-HEP, O3, and HO2 used to fit absorbtion data to obtain the concentration of each species. The bars superimposed over the plot are bandpass filters used to select the specific wavelengths used for data analysis.

2.5.3 β-HEP Self-Reaction Kinetics Measurements

The experimental set-up was tested and calibrated by measuring the β–HEP self-reaction rate in the absence of water vapor. The dry rate constant measured was (2.25±0.15) × 10^{-12} cm^3 $molecule^{-1}$ s^{-1} at 296 K, which is within the experimental uncertainity of the recommended NIST evaluation value, (2.31 ± 0.3)×10^{-12} cm^3 $molecule^{-1}$ s^{-1}) (see Figure 2.5)

The self-reaction of β-HEP follows two product branches, reactions 1 and 2

$$HOCH_2CH_2O_2 + HOCH_2CH_2O_2 \overset{k1}{\rightarrow} 2\ HOCH_2CH_2O + O_2 \tag{2.1}$$

$$HOCH_2CH_2O_2 + HOCH_2CH_2O_2 \overset{k2}{\rightarrow} HOCH_2CH_2OH + HOCH_2CHO + O_2 \tag{2.2}$$

The overall loss of β-HEP from both reactions was measured in these experiments. The observed rate constant, k_{obs}, is the overall rate constant representing the following four elementary reactions:

$$HOCH_2CH_2O_2 + HOCH_2CH_2O_2 \overset{k3}{\rightarrow} \text{Products} \tag{2.3}$$

$$HOCH_2CH_2O_2 + H_2O = HOCH_2CH_2O_2\text{-}H_2O \tag{2.4}$$

$$HOCH_2CH_2O_2\text{-}H_2O + HOCH_2CH_2O_2 \overset{k5}{\rightarrow} \text{Products} \tag{2.5}$$

$$HOCH_2CH_2O_2\text{-}H_2O + HOCH_2CH_2O_2\text{-}H_2O \overset{k6}{\rightarrow} \text{Products} \tag{2.6}$$

193 nm light was used to initiate production of β-HEP, but O_2 is also photolyzed to form singlet oxygen atoms that combine with O_2 to form ozone. The absorption cross section of ozone overlaps strongly with the cross section of β-HEP and HO_2 (Figure 2.4)(postulated to be formed due to undesirable secondary chemistry), causing an interference with direct absorption measurements. However, O_2 could not be excluded from the reaction gas mixture because O_2 is essential for the production of β-HEP and is used to convert $HOCH_2CH_2$ to β-HEP. Smaller flow rates of O_2 into the reaction mixture lengthened the conversion time of $HOCH_2CH_2$ into β-HEP, and unwanted secondary chemistry of $HOCH_2CH_2$ increased. Higher concentrations of O_2 in the reaction cell led to increased production of O_3 that complicated the analysis due to the overlapping absorption spectrum of O_3 with β-HEP. To reduce ozone formation and minimize

Table 1- Reactions used to fit β-HEP decays to obtain the self-reaction rate constant

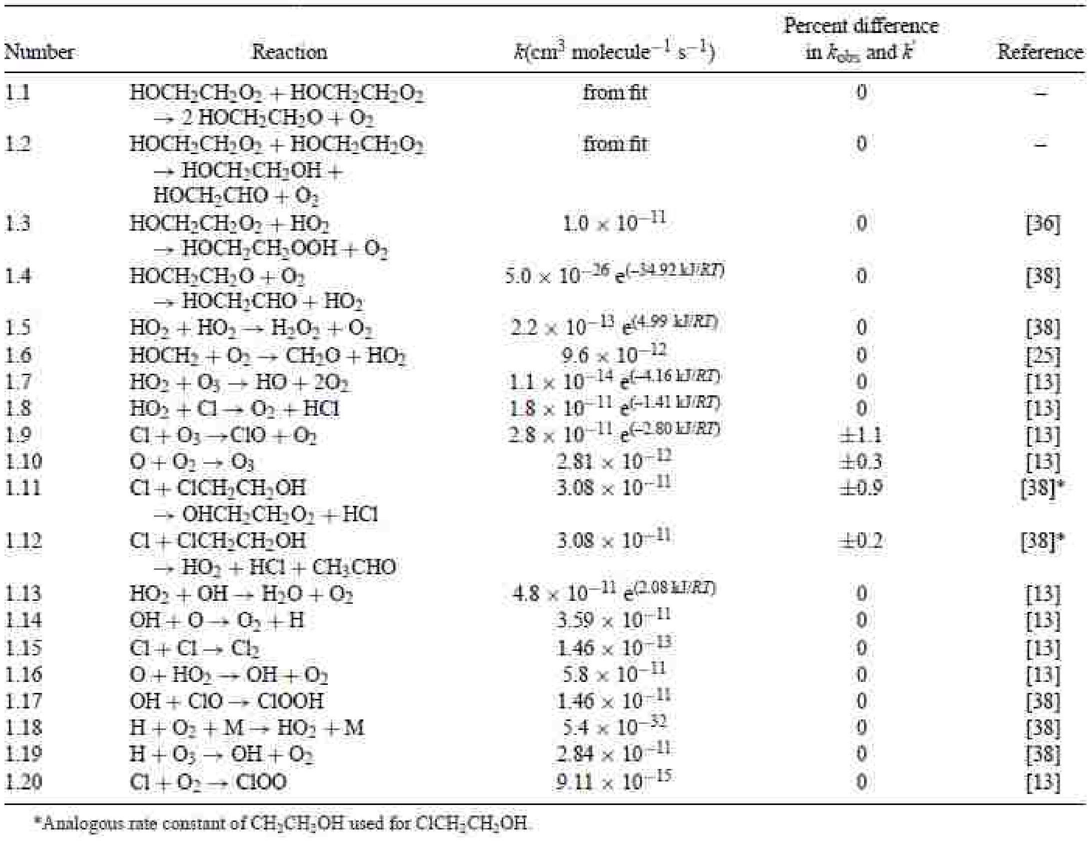

Number	Reaction	k(cm^3 molecule^{-1} s^{-1})	Percent difference in k_{obs} and k'	Reference
1.1	$HOCH_2CH_2O_2 + HOCH_2CH_2O_2 \rightarrow 2\,HOCH_2CH_2O + O_2$	from fit	0	–
1.2	$HOCH_2CH_2O_2 + HOCH_2CH_2O_2 \rightarrow HOCH_2CH_2OH + HOCH_2CHO + O_2$	from fit	0	–
1.3	$HOCH_2CH_2O_2 + HO_2 \rightarrow HOCH_2CH_2OOH + O_2$	1.0×10^{-11}	0	[36]
1.4	$HOCH_2CH_2O + O_2 \rightarrow HOCH_2CHO + HO_2$	$5.0 \times 10^{-26}\, e^{(-34.92\ kJ/RT)}$	0	[38]
1.5	$HO_2 + HO_2 \rightarrow H_2O_2 + O_2$	$2.2 \times 10^{-13}\, e^{(4.99\ kJ/RT)}$	0	[38]
1.6	$HOCH_2 + O_2 \rightarrow CH_2O + HO_2$	9.6×10^{-12}	0	[25]
1.7	$HO_2 + O_3 \rightarrow HO + 2O_2$	$1.1 \times 10^{-14}\, e^{(-4.16\ kJ/RT)}$	0	[13]
1.8	$HO_2 + Cl \rightarrow O_2 + HCl$	$1.8 \times 10^{-11}\, e^{(-1.41\ kJ/RT)}$	0	[13]
1.9	$Cl + O_3 \rightarrow ClO + O_2$	$2.8 \times 10^{-11}\, e^{(-2.80\ kJ/RT)}$	±1.1	[13]
1.10	$O + O_2 \rightarrow O_3$	2.81×10^{-12}	±0.3	[13]
1.11	$Cl + ClCH_2CH_2OH \rightarrow OHCH_2CH_2O_2 + HCl$	3.08×10^{-11}	±0.9	[38]*
1.12	$Cl + ClCH_2CH_2OH \rightarrow HO_2 + HCl + CH_3CHO$	3.08×10^{-11}	±0.2	[38]*
1.13	$HO_2 + OH \rightarrow H_2O + O_2$	$4.8 \times 10^{-11}\, e^{(2.08\ kJ/RT)}$	0	[13]
1.14	$OH + O \rightarrow O_2 + H$	3.59×10^{-11}	0	[13]
1.15	$Cl + Cl \rightarrow Cl_2$	1.46×10^{-13}	0	[13]
1.16	$O + HO_2 \rightarrow OH + O_2$	5.8×10^{-11}	0	[13]
1.17	$OH + ClO \rightarrow ClOOH$	1.46×10^{-11}	0	[38]
1.18	$H + O_2 + M \rightarrow HO_2 + M$	5.4×10^{-32}	0	[38]
1.19	$H + O_3 \rightarrow OH + O_2$	2.84×10^{-11}	0	[38]
1.20	$Cl + O_2 \rightarrow ClOO$	9.11×10^{-15}	0	[13]

*Analogous rate constant of CH_3CH_2OH used for $ClCH_2CH_2OH$

unknown chemistry between O(^{1}D) radicals and other species while still producing β-HEP in less than 30 μs, the O_2 concentration was decreased until the β-HEP concentration was 3-6 times the detection limit. The ozone concentration was between 3-5 × 10^{16} molecules cm^{-3} in the experiment.

Detection of β-HEP decays was begun 1 ms after the photolysis laser fired because residual reflections from the photolysis pulse interfered with detection by the PMT. Because photolysis of $HOCH_2CH_2Cl$ can form HO_2,[32, 49, 57] absorption of HO_2 was also considered. Three collection wavelengths at 220, 230, and 254 nm provide sufficient data for a least-squares fit to obtain the concentrations of O_3, HO_2, and β-HEP (see supplemental material section S2 for the equations used for the least squares fit and Figure 2.6A and 2.6B for typical decay curves). At each condition, multiple decay curves were measured until k_{obs} was within the 95% confidence interval of the mean. Typically, 9 to 34 β-HEP decay curves were collected at different initial β-HEP concentrations at each water vapor and temperature condition. The HO_2 concentration was always found to be below the detection limit (~1 × 10^{13} molecules cm^{-3})(i.e. the detection limit of the CCD and PMT was 0.006 absorbance units, therefore the detection limit for [HO_2] at 220nm=[0.006 ÷ (3.16×10^{-18} cm^2/molecule × 187 cm)]=1×10^{13} molecule/cm^3), and thus the least-squares fit was reduced to a two-parameter least-squares fit (Equation 1) Derivation of Equation 2-1 is shown in supplemental material section S-2

$$A_x = b\,(\sigma_x^{O_3}[O_3] + \sigma_x^{\beta-HEP}[\beta - HEP]) \qquad \textit{Equation (2.1)}$$

Where b=pathlength, σ=cross section, A=absorbance and x=220, 234 and 254nm.

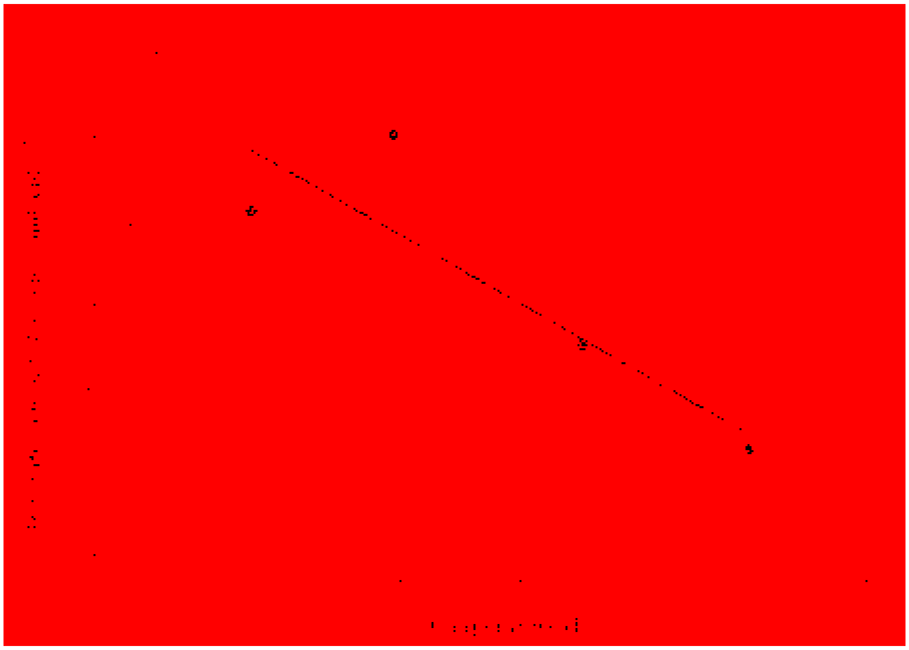

Figure 2.5- Comparison of the measured β-HEP self-reaction rate constant in the absence of water vapor as a function of temperature with the Atkinson et al. (NIST) published values. NIST values represented as solid line in the figure.

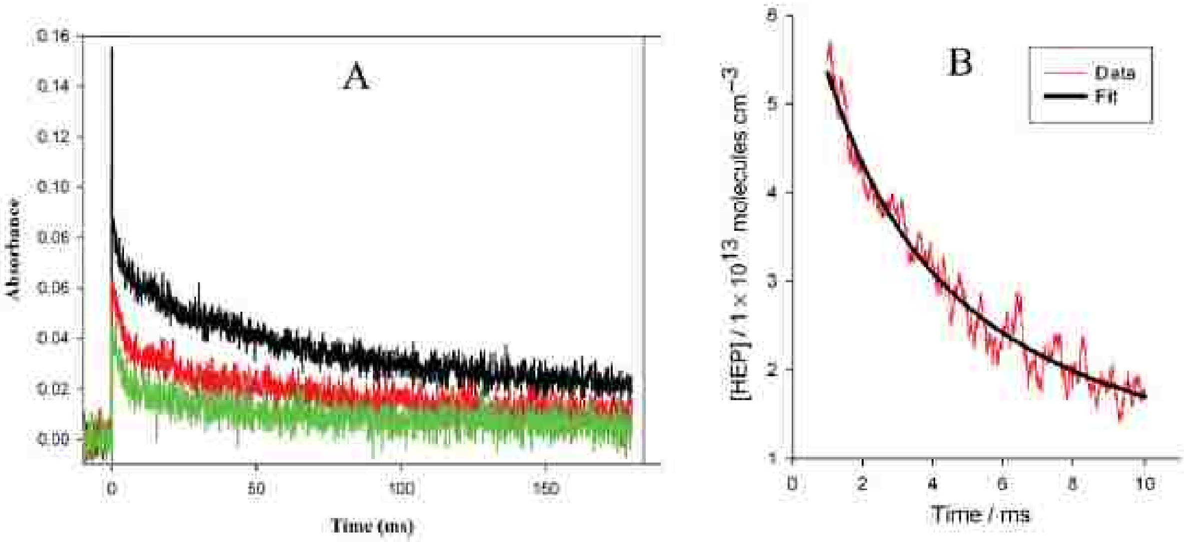

Figure 2.6- (A) Representative data collected at the three wavelengths 220 (green), 230 (red), and 254 (black). (B) A typical fit to the measured decay.

Table 2- k_{obs} and $[\beta\text{-HEP}]_0$ obtained from the model fit and measured dry rate constant as the function of temperature and water vapor concentration.

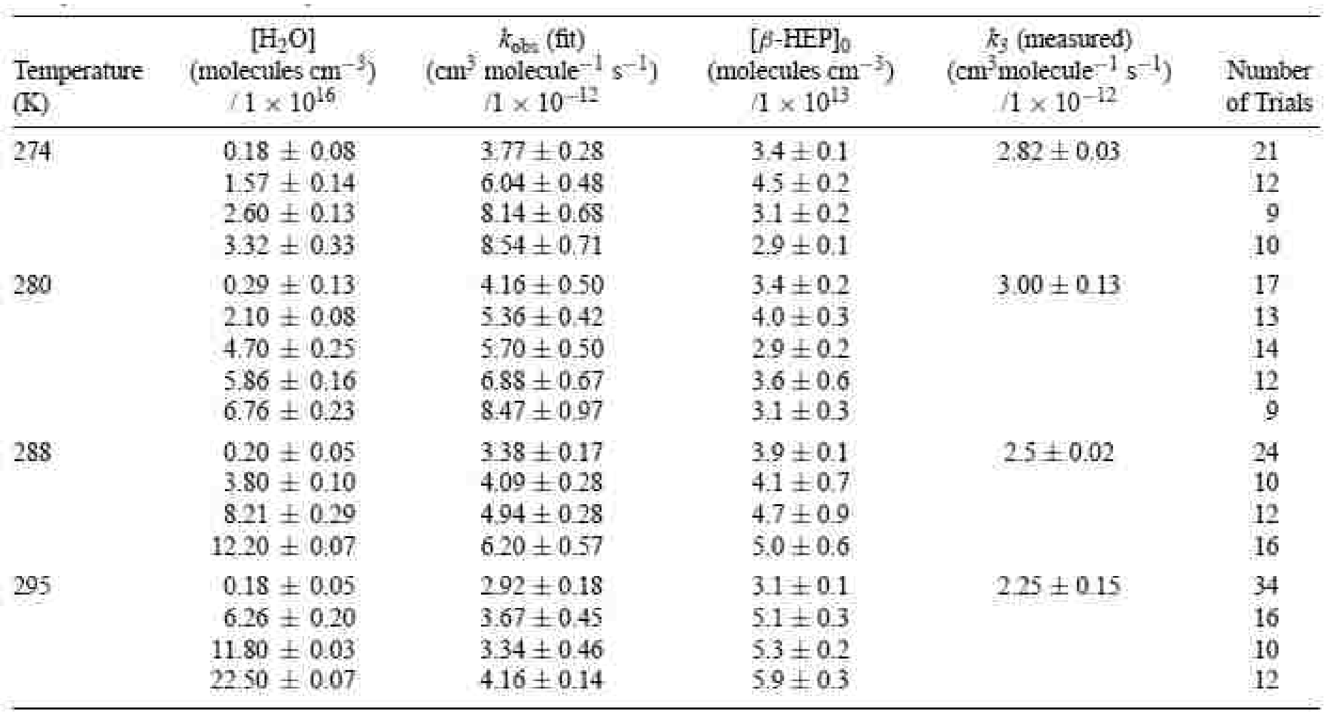

Temperature (K)	$[H_2O]$ (molecules cm^{-3}) $/1 \times 10^{16}$	k_{obs} (fit) (cm^3 $molecule^{-1}$ s^{-1}) $/1 \times 10^{-12}$	$[\beta\text{-HEP}]_0$ (molecules cm^{-3}) $/1 \times 10^{13}$	k_3 (measured) ($cm^3 molecule^{-1}$ s^{-1}) $/1 \times 10^{-12}$	Number of Trials
274	0.18 ± 0.08	3.77 ± 0.28	3.4 ± 0.1	2.82 ± 0.03	21
	1.57 ± 0.14	6.04 ± 0.48	4.5 ± 0.2		12
	2.60 ± 0.13	8.14 ± 0.68	3.1 ± 0.2		9
	3.32 ± 0.33	8.54 ± 0.71	2.9 ± 0.1		10
280	0.29 ± 0.13	4.16 ± 0.50	3.4 ± 0.2	3.00 ± 0.13	17
	2.10 ± 0.08	5.36 ± 0.42	4.0 ± 0.3		13
	4.70 ± 0.25	5.70 ± 0.50	2.9 ± 0.2		14
	5.86 ± 0.16	6.88 ± 0.67	3.6 ± 0.6		12
	6.76 ± 0.23	8.47 ± 0.97	3.1 ± 0.3		9
288	0.20 ± 0.05	3.38 ± 0.17	3.9 ± 0.1	2.5 ± 0.02	24
	3.80 ± 0.10	4.09 ± 0.28	4.1 ± 0.7		10
	8.21 ± 0.29	4.94 ± 0.28	4.7 ± 0.9		12
	12.20 ± 0.07	6.20 ± 0.57	5.0 ± 0.6		16
295	0.18 ± 0.05	2.92 ± 0.18	3.1 ± 0.1	2.25 ± 0.15	34
	6.26 ± 0.20	3.67 ± 0.45	5.1 ± 0.3		16
	11.80 ± 0.03	3.34 ± 0.46	5.3 ± 0.2		10
	22.50 ± 0.07	4.16 ± 0.14	5.9 ± 0.3		12

2.6 Results

2.6.1 β-$HOCH_2CH_2O_2$ Self-Reaction Kinetics

Each curve was fit to a model composed of coupled differential equations describing the reactions given in Table 1. Measured time-dependent concentrations of β-HEP, and calculated concentrations (using the photon flux and quantum yields of O_2 and H_2O photolysis) of oxygen atoms, hydrogen atoms and hydroxy radicals are inputs to the model. The outputs are concentration of β-HEP at time 0, the observed self-reaction rate of β-HEP (k_{obs}), and the HO_2 concentration. Table 2 presents the results of all experiments with 95% confidence intervals for $[H_2O]$, $[\beta\text{-HEP}]_0$, and k_{obs} at 274 K, 280 K, 288 K, and 296 K. Figure 2.6a shows representative decays collected at 220,230 and 254 nm. Figure 2.6b is a typical fit to the measured β-HEP decay. The total experimental error in k_{obs} ranges from 4 to 10% depending on experimental temperature and concentrations of O_3 and water vapor. This error could be reduced by decreasing the amount of O_2 in the cell, but, as noted previously, reducing oxygen would not produce sufficient β-HEP.

Sensitivity of the kinetic model was done to determine the effects of uncertainities in the rate constants on fiting k_{obs}. The rate constants were changed individually by ±30%, and the measured β-HEP decay curve were fit to obtain an adjusted value for k_{obs}, i.e. k'. This k' was compared against the k_{obs} obtained from the fit of the experimental data with the original model. These results are listed in Table 1 as the percent difference between k_{obs} and k'. For example, a 30% change in the rate constant of the O_3 + Cl reaction leads to a 1% change in calculated k_{obs}. The uncertainty in k_{obs} caused by uncertainities in the reactions of the model is estimated to be 2.5% (see table 1). The sensitivity analysis shows that secondary chemistry is dominated by reactions involving O_3 and Cl radicals.

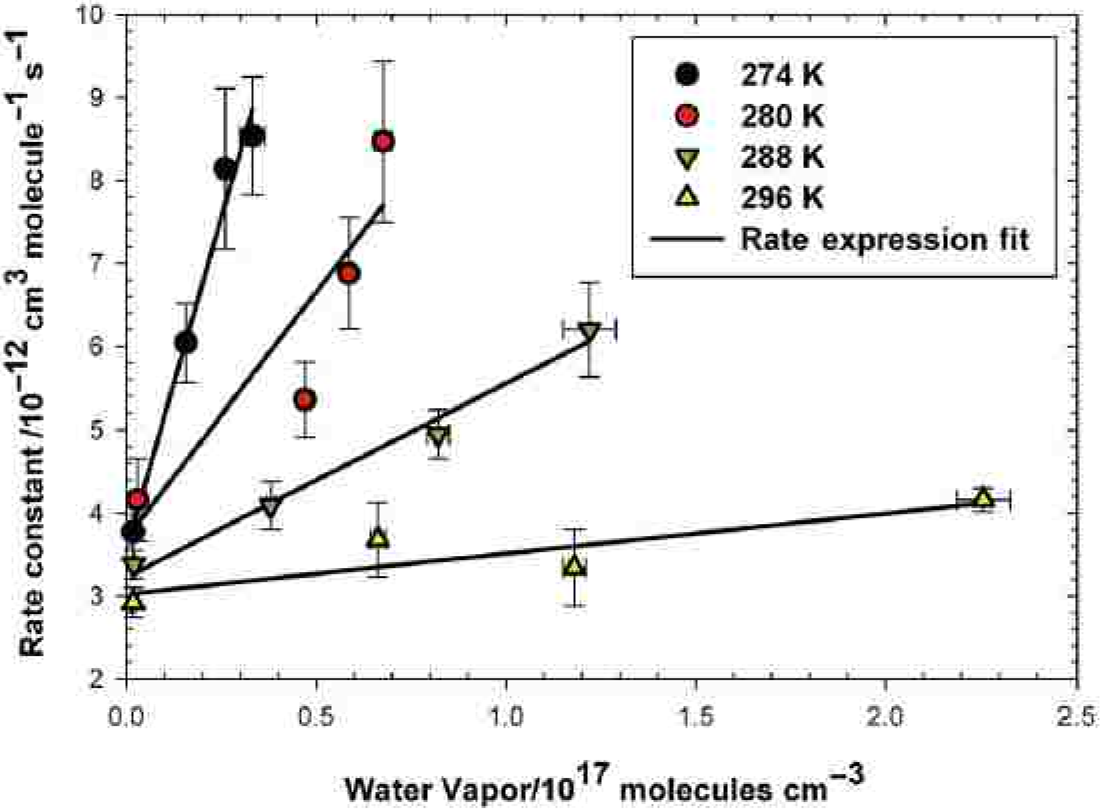

Figure 2.7- Observed rate constant (k_{obs}) for self-reaction of β-HEP versus water vapor concentration. The lines represents the fit to the rate expression (Eq. (III)) describing the rate as a function of both water vapor concentration and temperature.

In their HO_2 and HO_2-H_2O study, Cox and Burrows,[28] Kircher and Sander,[30] and Lii *et al*[31] applied the assumption that HO_2 and complex absorption cross sections are not resolveable in the UV. But Aliosio *et al,*[58] showed that the complex cross section in the UV is red shifted by 59nm, which contradicts above assumption. Therefore, in this study, we account for both complex and β-HEP cross section by assuming the following relationship,

$$\sigma_x^{\beta-HEP-H_2O} = f_x\, \sigma_x^{\beta-HEP}$$

where x = 220, 230 and 254 and $f_x \geq 0$.

An expression that describes the water vapor dependence of the β-HEP self-reaction must include the reactions of β-HEP with both β-HEP and β-HEP-H_2O and the reaction of β-HEP-H_2O with β-HEP-H_2O. A reduced form of the rate law is

$$k_{obs} = k_3 + k_5[H_2O] \qquad \text{Equation (2.2)}$$

where k_3 and k_5 are rate constants for reactions 3 and 5 respectively, and K is the equilibrium constant for reaction 4 (See supplemental material Section S-3 for a derivation of Equation 2). The same expression has previously been used to describe water vapor enhancement of the HO_2 self reaction. Equation 3, which is a functional form of equation 2 was used to obtain the temperature dependence of k_{obs} (see supplemental material section S-4 for the derivation)

$$k_{obs} = k_3\{1 + A \times [H_2O] \times exp(-E/RT)\} \qquad \text{Equation (2.3)}$$

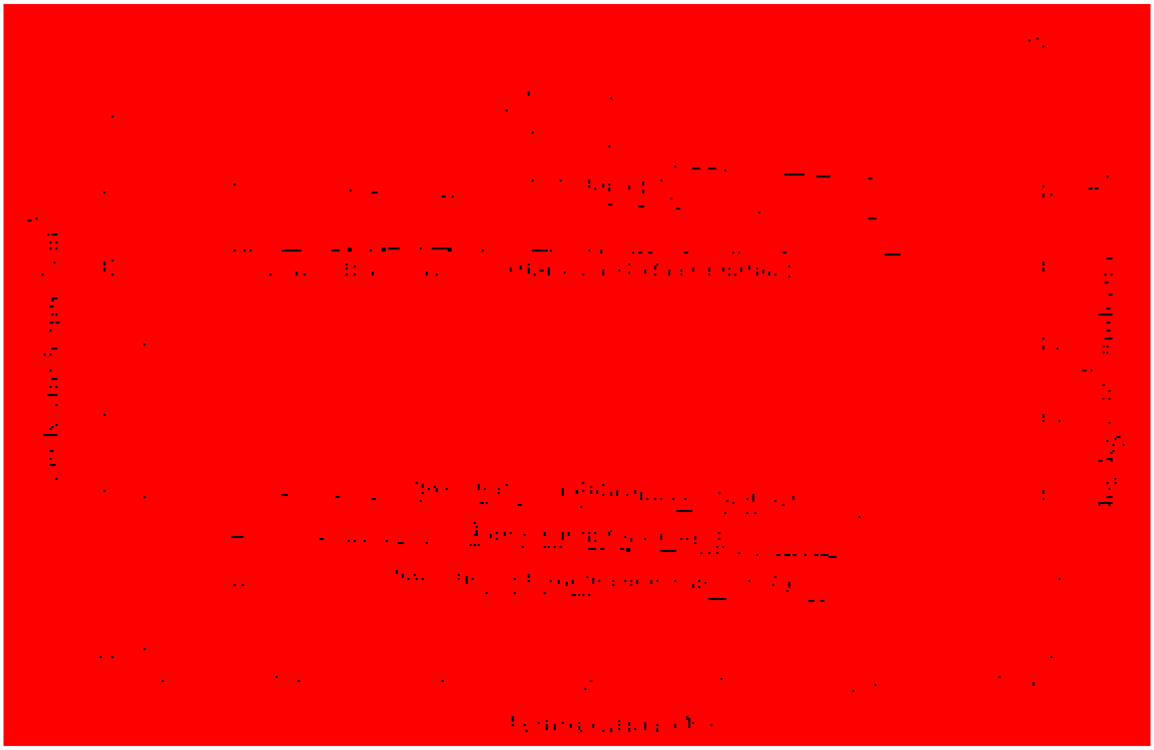

Figure 2.8- Effect of temperature on K and wet rate constant k_5. The solid line represents the change in the wet rate constant k_5, and the dotted line (--*--) represents the change in K. The dashed lines represent the uncertainty in K and k_5. The highlighted area represents the range of k_5 values limited by the hard sphere collision rate constant. Atkinson (NIST) evaluation for the dry rate constant (--**--) as a function temperature.

The measured k_{obs} were fit with Equation 2.3, which includes the contribution from the dry rate constant (k_3), the water vapor dependence, and the temperature dependence of the product, k_5K. Fits to the data in Figure 2.7 with Equation 2.3 are shown as solid lines. The enhancement from water vapor in Equation 3 is taken from the data collected in this work. The dry rate constant (k_3) values from this work are at 4 different temperatures only, therefore we have used the dry rate constant equation from Atkinson's (NIST) evaluation[49] of all previously available data on dry rates. Our data agree with the NIST evaluation (see Figure 2.5). Kircher[30] included a pressure dependent term in the model for the HO_2 self-reaction but no data for the pressure dependence of the β-HEP self-reaction is currently available. The best fit to the data in figure 2.7 yields the following rate expression:

$$k_{obs}(T,[H_2O]) = 7.8\times10^{-14}\exp\left((8.3\pm2.5kJ/mol)/\mathrm{R}T\right)\times\left\{1+(1.7\pm0.2)\times10^{-30}\times[H_2O]\times\exp\left((71\pm17kJ/mol)/\mathrm{R}T\right)\right\}$$

$$= 7.8\times10^{-14}\times\exp\left((8.3\pm2.5\mathrm{kJ/mol})/\mathrm{RT}\right)+(13.2\pm1.56)\times10^{-44}\times\exp\left((79.3\pm17.18\mathrm{kJ/mol})/\mathrm{RT}\right)\times[\mathrm{H_2O}]$$

Equation (2.4)

In their investigation of the kinetics of the HO_2 + HO_2-H_2O reaction, Kanno *et al.*[47] measured *K* and the rate constants independently. In this study, the product of *K* and k_5 is defined by the slopes of plots of k_{obs} vs [H_2O] at each temperature (see Equation 2.2 and Figure 2.7), and *K* and k_5 are inseparable from the data collected. Therefore, the equilibrium constant for the formation of the β-HEP-H_2O complex (*K*) was estimated from *ab initio* calculations, as described previously in the computational method section 2.1. The calculated *K* values as a function of temperature are given in Figure 2.8. The dashed lines around *K* in figure 2.8 are the uncertainty limits in K assuming an uncertainty in β-HEP-H_2O complex binding energy of ±6.3 kJ mol^{-1}.

Dividing the slopes (k_5K) of the fits in figure 2.7 by the calculated *K* yields k_5 values as shown in Figure 2.8. The uncertainty in *K* propogates into the calculation of k_5, shown as dashed lines in Figure 2.8. Since the calculated k_5 values cannot be larger than the hard sphere collision rate constant shown by the solid line in Figure 2.8, the calculated *K* values must be too small. Thus, the true *K* values must be near the upper uncertainty limit, and consequently, the k_5 values must be near the lower uncertainty limit in Figure 2.8. Kanno *et al.*[59] also found the *ab initio* calculated *K* values for the HO_2-H_2O complex to be an order of magnitude smaller than their experimentally determined *K* values. This suggests that *ab initio* calulated values of *K* may in general be an order of magnitude smaller than measured values of *K* for formation of radical-water complexes. In any case, the rate constant for β-HEP + β-HEP-H_2O (k_5) is 1 to 3 orders of magnitude larger than that for β-HEP + β-HEP (See Figure 2.8). To better estimate the effects of water vapor on the β-HEP self-reaction, the equilibrium consatnt K needs to be determined experimentally, but this is beyond the scope of this paper.

2.6.2 HO_2 Production and Secondary Chemistry

The formation of some HO_2 and Cl radicals in our experiments is inevitable. Determining the concentration of HO_2 and the secondary chemistry occuring due to HO_2 and Cl radicals is thus necessary. $HOCH_2CH_2Cl$ has 3 non-equivalent hydrogen atoms, abstraction of either alcohol hydrogen or a hydrogen alpha to the OH group leads to production of HO_2.

Extraction of the alcohol hydrogen from $HOCH_2CH_2Cl$ followed by reaction with O_2 leads to HO_2 formation via the following reactions:

$$HOCH_2CH_2Cl + Cl \rightarrow OCH_2CH_2Cl + HCl \tag{2.7}$$

$$OCH_2CH_2Cl + O_2 \rightarrow HO_2 + ClCH_2CHO \tag{2.8}$$

The fate of the OCH_2CH_2Cl radical has not been investigated in the presence of oxygen, but reactivity of the analogous OCH_2CH_3 radical in air has been reported by Atkinson *et al*[49]. They reported a rate constant of 1.1×10^{-14} cm^3 $molecule^{-1}$ s^{-1} for extraction of the alpha hydrogen by molecular oxygen.

Extraction of an alpha hydrogen by a Cl atom followed by reaction with molecular oxygen also produces HO_2 radical via the following reactions:

$$HOCH_2CH_2Cl + Cl \rightarrow HOCHCH_2Cl + HCl \tag{2.9}$$

$$HOCHCH_2Cl + O_2 \rightarrow HO_2 + ClCH_2CHO \tag{2.10}$$

Attack of a chlorine atom at a beta hydrogen produces 2-chloro-hydroxyethyl peroxy radical.

$$HOCH_2CH_2Cl + Cl \rightarrow HOCH_2CHCl + HCl \tag{2.11}$$

$$HOCH_2CHCl + O_2 \rightarrow HOCH_2CH(O_2)Cl \tag{2.12}$$

To address the question of the relative significance of these reactions, the product branching ratio for extraction of the alcohol, alpha and beta hydrogen was calculated using high level *ab initio* calculations. A slice of the potential energy surface is included in supplementary material Figure S1. Extraction of an alpha hydrogen from $HOCH_2CH_2Cl$ has the lowest energy barrier (19 kJ mol^{-1}) followed in energy by extraction of the beta hydrogen (37 kJ mol^{-1}) and finally the alcohol hydrogen (100 kJ mol^{-1}). The product branching ratio and the rate constant reported by Garzon *et al*[60] and Taatjes et al[61] for Cl + $HOCH_2CH_3$ were used as a surrogate for Cl + $HOCH_2CH_2Cl$ owing to the similar activation barriers reported (7, 18, 111 kJ mol^{-1}). The kinetic model in Table 1 includes the product branching ratios for the reaction of Cl + $HOCH_2CH_2Cl$ and the other possible secondary chemistry reactions of Cl and HO_2 radical that are listed in Table 1. The model predicts the amount of HO_2 formed in the reaction mixture and the amount of Cl atoms that are lost as a function of time.

Reactions 1.15 and 1.8 in Table 1 both have large rate constants, but make a negligible contribution to the loss of chlorine atoms because the concentrations of Cl and HO_2 are very small. Reaction 1.20 is a three-body reaction, but because of the relative high concentration of O_2 and the total pressure in the cell, accounts for 3% of the loss of chlorine atoms. Aside from the reactions of Cl with $HOCH_2CH_2Cl$ (reactions 1.11and 1.12) which account for 52% of Cl atom loss, reaction 1.9 accounts for the largest loss of Cl atoms (44%).

The effect of H and OH radicals on the HO_2 concentration are also included in the model. In this study. The 193 nm light was used to initiate photolysis of $HOCH_2CH_2Cl$ in the cell. This wavelength of light is capable of photolyzing both H_2O and O_2 in the cell, leading to formation of H, OH and O radicals. The photon flux and quantam yields for photolysis of H_2O and O_2 predict the formation of 4.5×10^{13} molecules cm^{-3} of H and OH radicals from H_2O photolysis and 3.6×10^{16} molecules cm^{-3} of O atoms from photolysis of molecular oxygen. These values were included as initial concentrations of H, OH and O in the model. HO_2 is formed in the cell from reactions 1.4, 1.6, 1.12, and 1.18. H and OH radicals have opposing effects on the HO_2 radical concentration. H radical increases the concentration of HO_2 due to the reaction of H and O_2, whereas OH radical remove HO_2 due to the fast reaction between OH and HO_2. H radical is responsible for formation of 34% of HO_2 radical in the cell, whereas OH radical is responsible for 32% of removal of HO_2 radical. Overall, these effects increase formation of HO_2 radical. The model predicts HO_2 concentration to steadily increase after photolysis. But, at 10 ms, the HO_2 concentration is predicted to be 6×10^{12} molecules cm^{-3} and below our detection limit of 1×10^{13} molecules cm^{-3} confirming the experimental observations. HO_2 is not produced in measurable concentration, but can still contribute to the decay of β-HEP and for this reason is included in the model fits.

2.7 Discussion

The current study showed no evidence for significant HO_2 production, but in their investigation of β-HEP self-reaction kinetics with a similar source chemistry, Murrells *et al.*[48] reported measuring significant concentrations of HO_2.. They reported initial concentrations of HO_2 that were twice that of β-HEP and explained that this was due to an unknown source of HO_2 production. One possible explanation for the discrepancy between Murrells *et al.* and this work is that Murrells *et al*. did not include O_3 in their data analysis and it is likely that the signal attributed to HO_2 was instead O_3. No concentrations of precursor gas species were reported by Murrells *et al.* but the published decays of β-HEP have no discernible time delay between the formation of $HOCH_2CH_2$ and β-HEP, suggesting a high concentration of O_2 was used to drive β-HEP formation. A high concentration of O_2 produces a significant amount of O_3 from photolysis at 193 nm. In addition, their wavelength selection of 225 and 260 nm complicates the data analysis. The absorption cross-sections of HO_2, β-HEP, and O_3 are listed in Table 3. At 225 nm the cross sections of HO_2 and O_3 are the same and the cross section of β-HEP is only 28% greaterare within 20% of one another, but at 260 nm, the cross section of O_3 is 30 times larger than the cross section of HO_2, and β-HEP's cross section is 11 times larger than the cross section of HO_2. Thus, the use of 225 and 260 nm as probe wavelengths only provides enough information to deconvolve HO_2 and β-HEP from one another. At 225 nm, O_3 absorption overwhelms the signal attributed to HO_2. The absence of treatment of O_3 in Murrells et al.'s work thus explains the discrepancy between the results of Murrells *et al*. and this work.

Anastasi *et al.*[46] reported a β-HEP self-reaction rate constant of 7.69 (±1.2) $\times 10^{-12}$ cm^3 $molecule^{-1}$ s^{-1} at 300K, 3.4 times larger than the dry rate constant, 2.31×10^{-12} cm^3 $molecule^{-1}$ s^{-1}, others reported.[45, 47, 48, 62] The difference was attributed to the use of different absorption cross sections for β-HEP[48]. However, Anastasi *et al.*[46] used a water vapor concentration of approximately 1×10^{18} molecules cm^{-3}, resulting in formation of the reactive β-HEP-H_2O complex which they did not account for. The rate constant reported by Anastasi *et al.* agrees with the k_{obs} measured in this work (Equation 4).

The data presented in this work describe the relationship between increasing rates of reaction of peroxy radicals and increasing water vapor. *Ab initio* calculations estimated the equilibrium constant to allow determination of both the percentage of β-HEP complexed with water and the rate constant for β-HEP + β-HEP-H_2O (Reaction 5). Enhancement of peroxy radical self-reaction by water depends on the fraction of radical complexed with water and on the nature of the peroxy radical. For example, HO_2 and β-HEP have equilibrium constants of formation with water within an order of magnitude, but at 50% relative humidity and 280 K, the rate constant for β-HEP is 6.1 times larger than the dry rate constant whereas the rate constant for HO_2 is 1.5 times larger than the dry rate constant. The calculated fraction of β-HEP radical complexed with water vapor has a large uncertainty mostly due to the uncertainty in the calculation of K. Future work must measure the K values experimentally to better estimate the enhancement in the β-HEP self-reaction rate.

The contribution of water vapor to the rate of loss of β-HEP and HO_2 is determined by the ratio k_{obs}/k_3 defined here as the enhancement factor. This enhancement factor allows a measure of the contribution of water vapor to the rate of loss of β-HEP and HO_2 at differing temperatures and relative humidities, Figure 2.9. For any given water vapor concentration the rate of loss of β-HEP is faster than the loss of HO_2, e.g. at 298 K the rate of loss of β-HEP is twice that of HO_2.

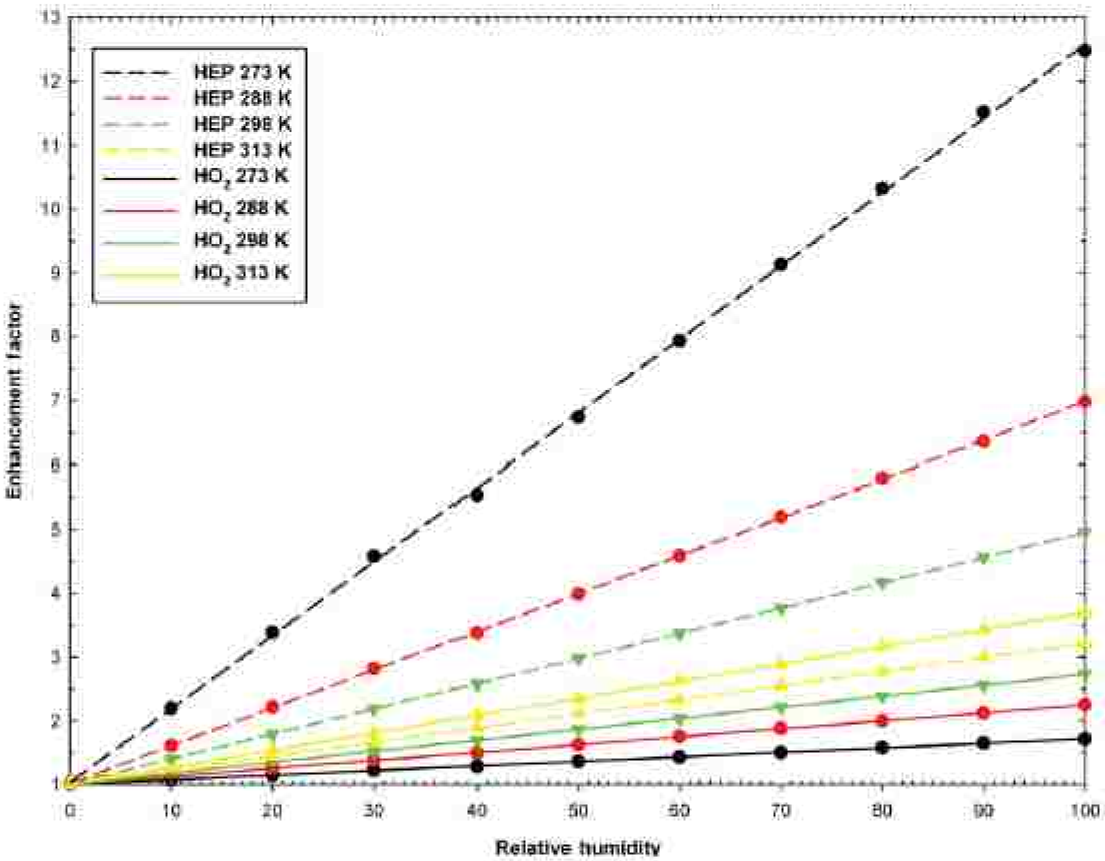

Figure 2.9- Enhancement of the self-reaction of β-HEP and HO2 at various relative humidities and temperatures

2.8 Conclusion

Water vapor catalysis will become increasingly more significant as global warming increases water vapor concentrations in the troposphere. Before the water vapor effect on the HO_2 self-reaction was included in atmospheric models, the models predicted a much higher concentration of HO_2 in the atmosphere. As evidenced by the work of Stockwell,[38] inclusion of the effect of water vapor on the self-reaction rate of HO_2 leads to a 75% decrease in the prediction of tropospheric HO_x and O_3 concentrations. Thus, it is likely that current models overpredict the concentation of β-HEP and other peroxy radicals and consequenlty overestimate the concentration of O_3. β-hydroxy peroxy radicals are atmospherically important because they are productsin the reaction of OH radicals with unsaturated VOC's from diverse emission sources. Isoprene and terpenes are two major examples of biogenic sources that produce β-hydroxy peroxy radicals and should demonstrate a water vapor enhancement of the kinetics. Thus, future studies on the effect of water vapor on the kinetics of peroxy radical reactions should focus on β-hydroxy peroxy radicals and related compounds that form two hydrogen bonds with water and have binding energies greater than 17 kJ mol^{-1}. Most likely inclusion of the effects of water vapor on the kinetics of the β-HEP and HO_2 self-reactions in atmospheric models will lead to predictions of smaller tropospheric O_3 concentations. To correctly predict pollution levels, atmospheric models also need to be adjusted to include the effects of polar molecules such as methanol and ammonia on the rates of radical reactions.

Recognition is made to the National Science Foundation (Grant No. 0924146 and 1238947) for support of the present work.

3 DISCHARGE-FLOW MASS SPECTROMETER

3.1 Origins of the Flow Tube Method

The discharge-flow mass spectrometer (DFMS) is a great resource in studying the kinetics of atmospheric reactions. The purpose of this section is to provide a brief history of the flow tube with emphasis on the developments that have contributed most to its application as a kinetic tool.

In the 1970s and 1980s, there was an increased demand for gas phase reaction rate data. At the time, there were serious environmental, economic, and social implications of gas phase kinetic data. Models based on these data predicted the impact of anthropogenic chemicals on stratospheric ozone and other key atmospheric reactions. Committees and organizations were formed to collect, evaluate, and disseminate this atmospheric kinetic information. With high concern for accuracy in the atmospheric reaction rate constants, many researchers began to utilize the DFMS as a key source for measurements. During this era, the DFMS served as the most prolific source of atmospheric kinetic data.[1] Figure 3.1 shows a schematic of a simple flow cell that gave rise to today's DFMS.

The flow tube kinetic method evolved from early discharge tube studies conducted by Wood and Bonhoeffer in the early 1900's as they experimented with resonance fluorescence in metal atoms.[63] In 1929, Smallwood performed the first flow tube kinetic study, reporting the rate of recombination of hydrogen atoms. Smallwood adapted the Wood-Bonhoeffer type discharge tube in order to create atomic hydrogen,[64] and the atom concentration in the flow tube was measured with a calorimeter attached to the outside of the flow tube.

An important step in DFMS was the invention of the Wrede-Harteck gauge,[65] a simple device for measuring the partial pressure of atoms in a discharged gas mixture. Harteck studied the reactions of atomic oxygen with various compounds. Atomic oxygen was produced by an AC discharge, its concentration estimated using the Wrede-Harteck gauge, and the reactivity determined qualitatively by spectroscopic measurements of its chemiluminescence.

In the late 1950's and 1960's, several important advances were made in flow tube techniques and instrumentation. In 1958, Kaufman[66] demonstrated that the intensity of the chemiluminescence was proportional to the concentrations of the reactants, i.e $I \alpha [A]$. This discovery provided a sensitive and quantitative detection method. Similarly, Kaufman demonstrated that extremely fast gas phase reactions could be quantified by gas phase titrations. The concept of gas phase titrations has now been extended to many different radical species, and serves as a clean, quantitative method in fast stoichiometric reactions.[1]

The use of chemiluminescence as a detection scheme in a flow tube was universal for several years. Clyne et al.[67] were the first to develop UV detectors to monitor atomic oxygen, and Setser et al.[68] reported using an IR detector to study hydrogen extraction. The greatest development in instrumentation of a flow tube, however, was the implementation of a quadrupole mass spectrometer as a detector. Foner and Hudson[69] and Phillips and Schiff[70] were the first to combine mass spectrometer detectors with flow tubes for kinetic measurements. Since then, this combination has been successfully exploited in a wide variety of kinetic application, and resembles mostly to that of today's DFMS.

3.2 Schematic and Technique of a Kinetic Flow Tube

A schematic of a simple flow tube is shown in Figure 3.1. The major component is a glass tube surrounded by a controlled jacket to maintain steady constant temperature. The inner flow tube surface is often treated with a wall coating to inhibit the removal of radicals on the tube's surface.[71]

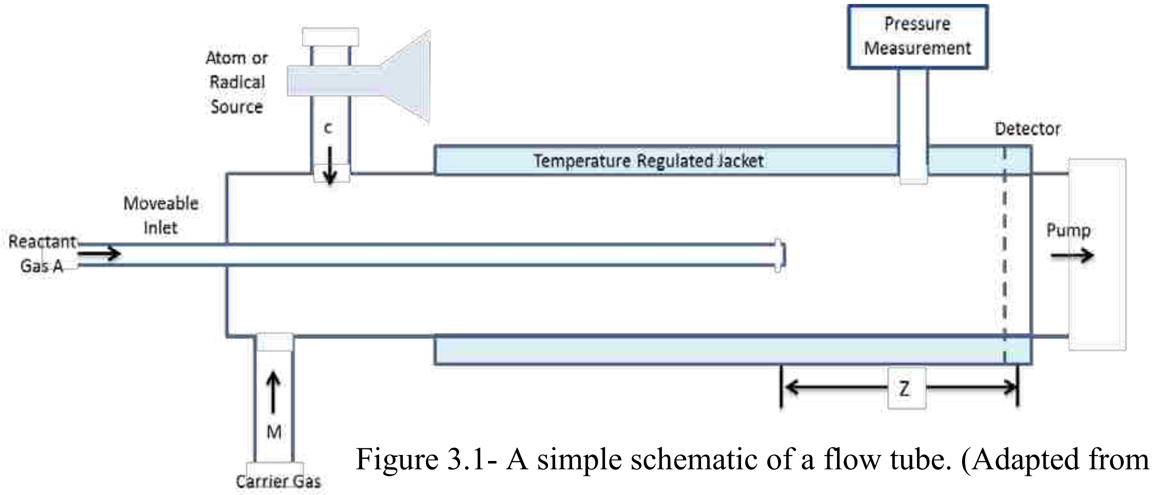

Figure 3.1- A simple schematic of a flow tube. (Adapted from Howard)[1]

The carrier gas (M) enters the flow tube at the left. This gas is the major component in the flow tube and defines the physical properties of the gas stream, such as pressure, flow velocity, heat capacity, viscosity, etc. This gas also acts as a heat bath to maintain the reactants at the temperature of the glass wall, controls diffusion, and serves as a third body in termolecular reactions. Helium traditionally serves as the carrier gas for its inertness and high thermal conductivity.

Atomic or radical reactants (c) are most commonly generated by a microwave discharge. These reactants can be further converted to different atomic or radical species by a titration reaction before being introduced into the flow cell. The radical reactant enters the flow tube via an inlet downstream from the carrier gas entrance. A small flow of He or Ar is used to flush the gas through the radical source.

A pressure port is located at the center of the reaction zone to minimize errors and corrections due to the pressure gradient in the flow tube. The pressure port needs to be oriented properly so as to measure only the static pressure in the flow tube.

Flow tube kinetic measurements usually are made by varying the reaction zone length (Z), which consists of the distance between the point the two reactants meet and the point of detection. The reaction zone length can be changed by either moving the point of mixing or the point of detection. The easiest and most common method is changing the mixing point by using a moveable injector tube as seen in Figure 3.1. The exit orifice on the moveable injector tube consists of a series of small holes around the diameter of the tube. The purpose of this configuration is to provide a rapid mixing of the added gas with the carrier stream. Added reactant A is assumed to be thoroughly mixed with the carrier gas.

Sensitivity is important when determining the detection method. For the best results, the concentration of the radical species, c, should be less than 10^{11} molecules cm^{-3} when radical reactions are studied. Typically, the concentration of the added reactant, A, is much larger by several orders of magnitude, thus creating a pseudo-first order reaction in c.

3.3 Calculating the Kinetics in a Flow Tube

When the flow tube is run under pseudo-first order conditions, i.e. [A]>>[c], the rate equation is

$$\frac{d[c]}{dt} = -k[c] \qquad \text{Equation (3.1)}$$

and only the relative concentrations of c need to be measured.

A basic assumption is made that the radical reactant is mixed homogeneously with the carrier gas and that there are no concentration gradients. A second assumption is made that the carrier gas flow velocity (v) is the same as the radical velocity (usually 300-2000 cm s^{-1}). With these assumptions, the reaction time (t) in the flow tube, $t = Z/v$, is the time from when the radicals and reactants mix at the point of contact to the point of detection. Thus, reaction time and distance are equivalent in the flow system.

A rate constant measurement is made by measuring the radical concentration with the moveable injection tube at several different positions, while the reactant flow rate is held constant (i.e. $= 10cm, 20cm, 30cm, etc$). The data are plotted ln[c] vs. Z and the slope is used to calculate the pseudo-first order reaction rate constant

$$k = -v\,\frac{d(\ln[c])}{dz} \qquad \text{Equation (3.2)}$$

Limitations to this method, i.e. wall loss, axial and radial diffusion, pressure gradients, etc, can all be accounted for and are discussed by Howard.[1] The pseudo-first order rate constant, k, can be converted into a true second order rate constant, k', by plotting the k vs. the concentration of the excess reagent. The slope of this line is the true second order rate constant.

3.4 A Modern Discharge Flow Mass Spectrometer

With the addition of the mass spectrometer to the flow tube, further engineering adjustments had to be made to the simple flow tube design shown in Figure 3.1. While flow tubes are normally operated at pressures approximate to 1 Torr, traditional quadrupole mass spectrometers are not able to properly function above $>10^{-4}$ Torr. In order to couple a flow tube to a quadrupole mass spectrometer, intermediate stages are required to systematically lower the flow tube pressure to ideal quadrupole pressures. Figure 3.2 depicts these intermediate stages, and resembles a modern DFMS system. During the 1970's and 1980's, these intermediate stages were pumped down with diffusion pumps, a very messy and expensive method to achieve high vacuum. A majority of the expense came from the constant need of replenishing liquid N_2 in the diffusion pump cold traps. This required 24 hour monitoring and systems in place to refill the liquid N_2 cold traps when necessary.

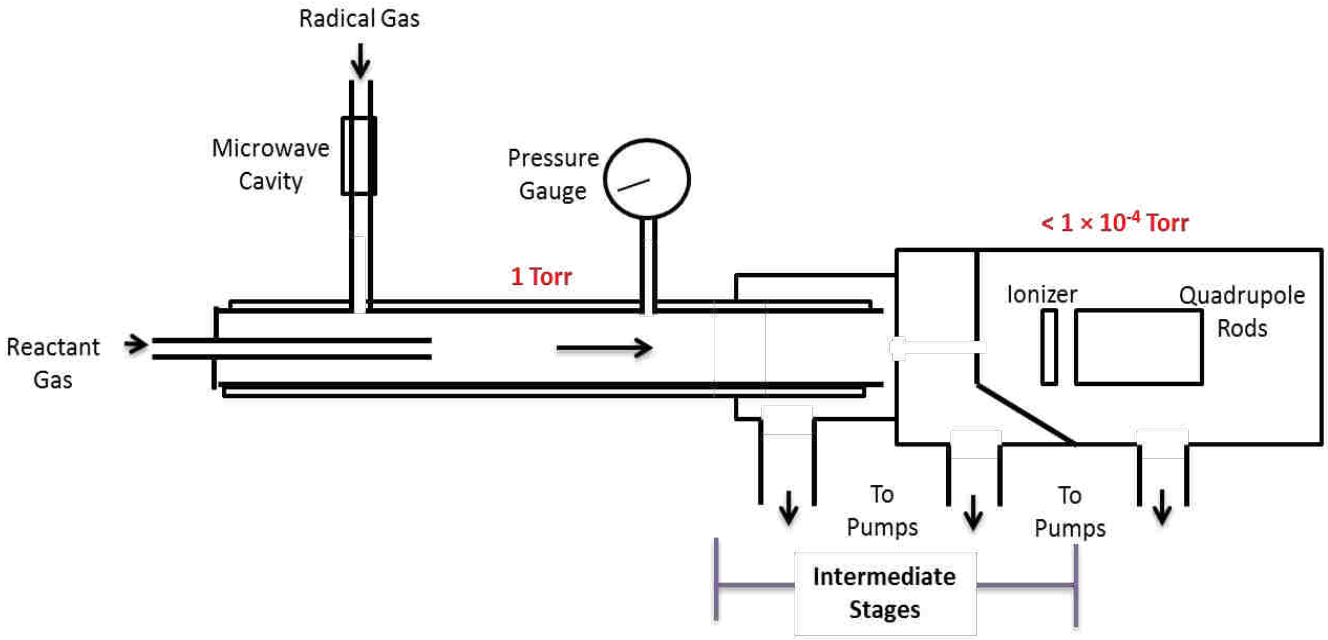

Figure 3.2 - Modern flow tubes require intermediate pump down stages in order achieve pressures suitable for quadrupole mass spectrometry.

As the demand and funds for atmospheric kinetics diminished, many researchers could not afford to maintain the operation of the DFMS systems. In the decades following the 1980's , these systems were shut-down, stored, or repurposed. By the early 2000's, only a dozen or so of DFMS systems were operating globally.

3.5 NASA's Jet Propulsion Laboratory Discharge Flow Mass Spectrometer

Since its inception in 1958, one of NASA's programmatic goals has been to be the top leader in atmospheric science. During the 1970's and 1980's, NASA funded the research of many atmospheric kineticists. A few of these scientists went on to win a Nobel Prize for their research in ozone layer depletion. Many of these researchers employed the use of DFMS in their studies. With time, these researchers could no longer justify the expense of operating the DFMS.

Now, over 30 years later, the need of a functional DFMS is required. Many of the atmospheric rates measured in the 1970's and 1980's are in need of reevaluation. In 2014, Cline[72] demonstrated that atmospheric reaction rates and kinetics can be influenced by the presence of water vapor. With the increase of global temperature, the need to reevaluate atmospheric gas phase reactions as a function of water vapor concentration is required. With this end in mind, Stan Sander of the Jet Propulsion Laboratory and Jaron Hansen of Brigham Young University decided to resurrect an old discharge flow mass spectrometer, and equip it with the most advanced hardware.

Figure 3.3 shows the schematic of the newly engineered DFMS. The initial parts consisted of an inherited two-stage vacuum chamber, a 30 year old Pyrex jacketed flow cell, and a 15 year old mass spectrometer; none-of-which had come from the same system.

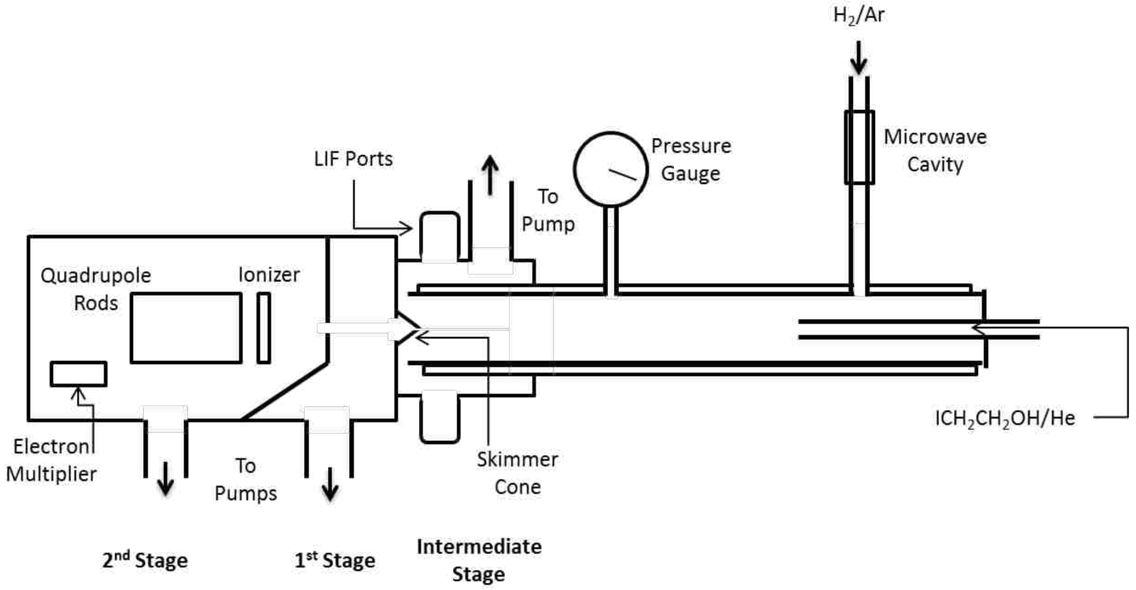

Figure 3.3 – The DFMS engineered at NASA's JPL

The vacuum chamber for the quadrupole mass spectrometer was redesigned to use turbo pumps instead of diffusion pumps to vacuum out the system. The vacuum chamber is a two-stage differentially pumped vacuum system. The first stage is pumped using a Pfeifer Hi Pace 1500 turbo which was backed by an XDS35i scroll pump. The second stage, which houses the quadrupole mass spectrometer, is pumped by a Pfeifer Hi Pace 700 turbo pump, which is backed by a Pfeifer Hi Pace 80 turbo pump, which is then again backed by an XDS15i scroll pump. An MKS Pirani gauge and an MKS Mini-Ion were mounted onto each chamber to monitor chamber pressures. After the new equipment was mounted, the two-stage vacuum chamber was sealed and pumped down. After leak checks and minor adjustments, pressures less than 8×10^{-9} Torr were achieved.

Adjustments were made to the interior of the chambers along the analyte flight path. A mounting plate was built and installed on the entry port to the first stage to allow a new Beam Dynamics skimmer cone to be placed in line with the quadrupole axis (see Figure 3.3). The skimmer currently installed has a 1.0 mm opening and is held in place by a metal collar; the vacuum seal is provided by a thin layer of TorrSeal between the skirt of the skimmer and the mounting plate. A second skimmer with an opening of 0.5 mm is available (but not yet mounted) if working pressures higher than 1 Torr are needed.

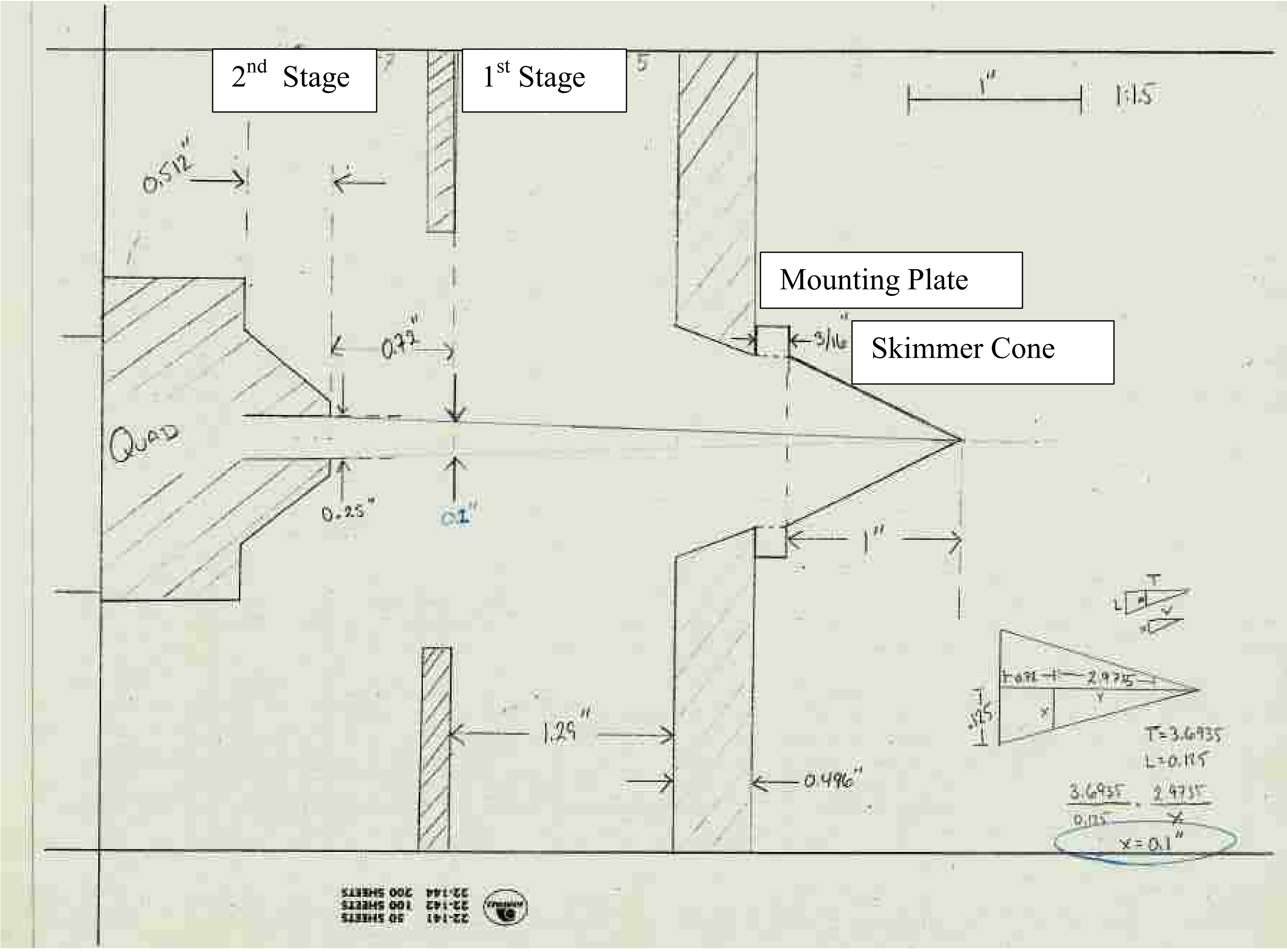

Figure 3.4 – A skimmer cone with a 1mm opening gives entry into the 1st stage.

Between the first and second stage, a 1 mm pinhole plate was designed to narrow the aperture between the stages. This plate also allows for a beam chopper to be mounted to interrupt the analyte path. (see Figure 4.5)

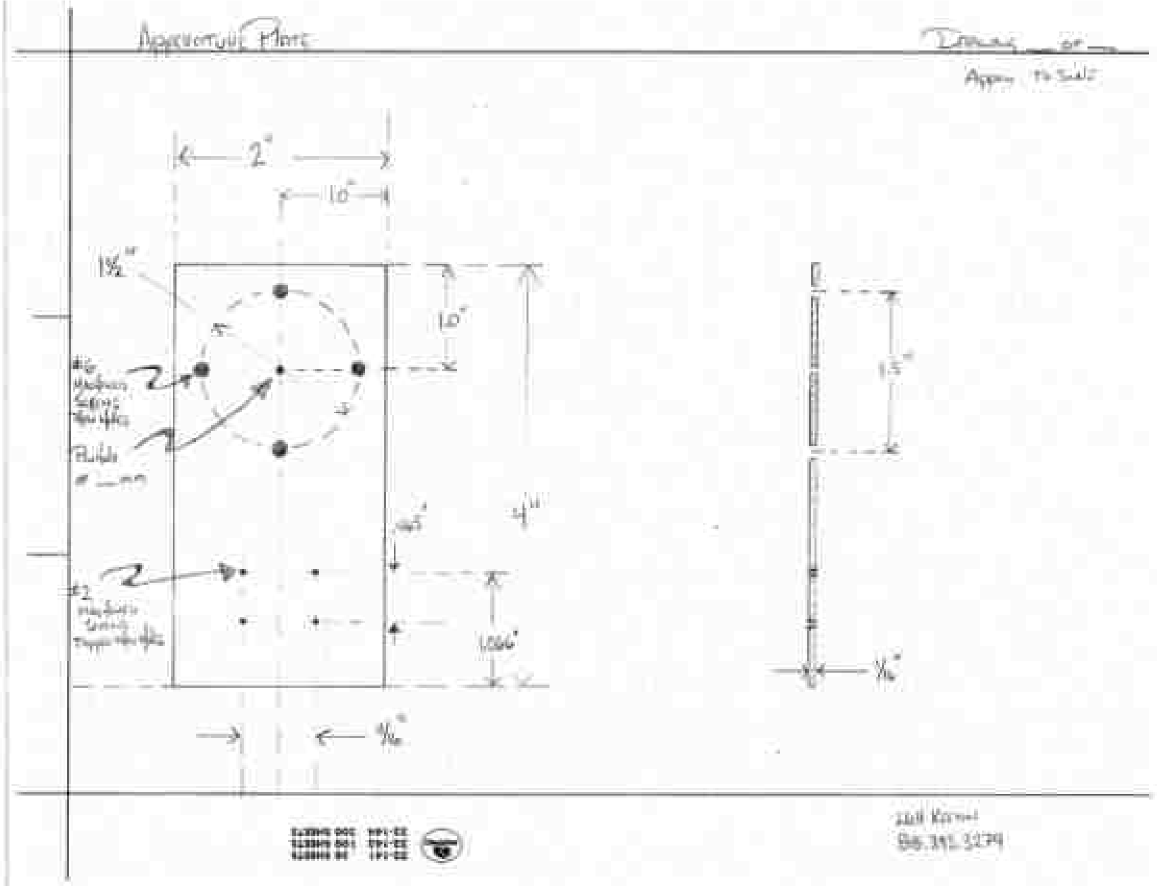

Figure 3.5- The aperture plate that separates the 1st and 2nd chamber

Because the inherited vacuum chamber and the old Pyrex flow cell were originally part of two separate systems, a new intermediate chamber had to be designed to couple them together. From the new intermediate chamber extend five flanges. One radial flange with a KF connection is used to direct the main gas flow to the rotary pump in the channel. Four other radial Conflat flanges are available for LIF detection (see Figure 3.6). A 125 cfm mechanical pump (Edwards Model E2M175) connected to the intermediate stage is employed to maintain a steady state pressure of about 1 Torr in the reactor.

The flow reactor cell consists of an 80-cm-long, 3.75 cm-i.d. Pyrex tube coated with halocarbon wax to reduce radical wall loss. Flows are controlled inside the reaction cell by MKS Flow controllers (2000 sccm, 200 sccm, 100 sccm, and 50 sccm). Pressure in the reaction cell is monitored using MKS Baratron 10 Torr and 1000 Torr gauges.

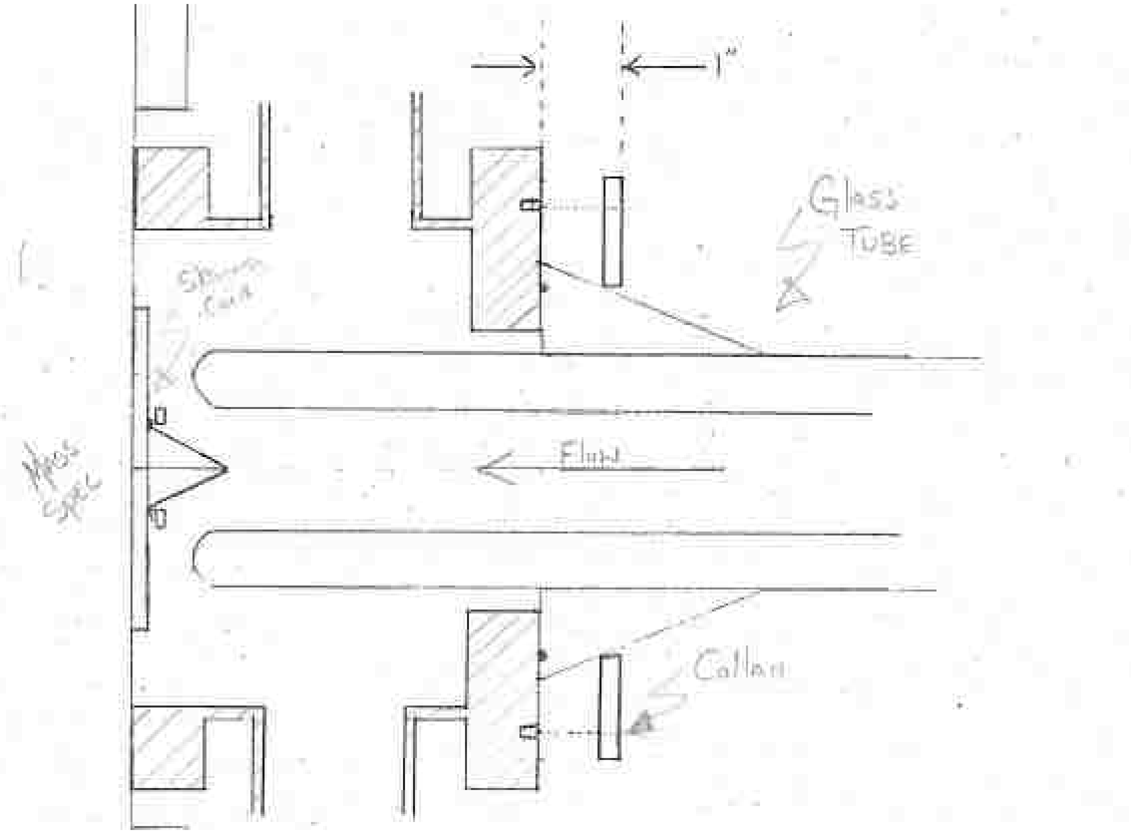

Figure 3.6 – An intermediate stage was machined to couple the vacuum chamber and glass flow cell.

A removable liquid nitrogen trap was placed downstream of the reactor in order to protect the vacuum pump from corrosive reactants and products. Several other small parts had to be designed and machined in order to couple the vacuum chamber to the flow cell. For further interest, the supplementary material section contains most of the technical drawings used to machine necessary parts.

Initial leak testing uncovered minor leaks, that were then fixed. At the present time, with 1 Torr of He in the flow tube, the pressure in the 1st Stage chamber is about 1×10^{-5} Torr and the 2nd Stage is at 3×10^{-7}. If no gas is flowing, the 2nd Stage has reached $3\times^{-8}$ Torr. No bake-out or over-night pumping has been attempted yet. A calculated ratio of pressures between the flow cell and the 1st stage using a 1700 l/s through a 1 mm pinhole was compared to actual pressures observed in the system (see Figure 3.7).

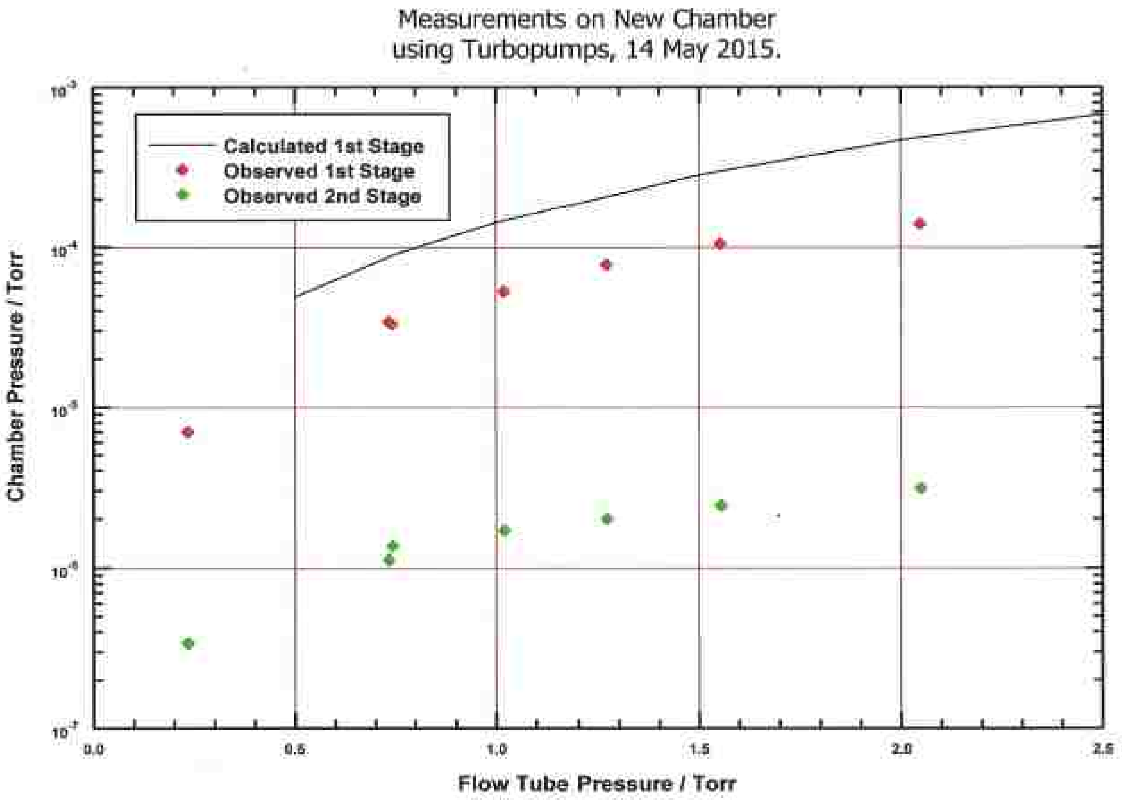

Figure 3.7 – Calculations were done for N_2, measurements with Ar.

The installed quadrupole mass spectrometer is an Extrel Model 150 Model 5221. Alignment of the quadrupole through the vacuum apertures was achieved using a red HeNe laser. Detection was carried out by continuous sampling at the downstream end of the flow tube, through a two-stage beam inlet system. The mass spectrometer was set to emit bombarding electrons with 25 eV of impact energy.

Initial testing of the ion signals was done using 1 Torr of He with a small amount of NO (Figure 3.8). Quadrupole settings were adjusted to optimize signal detection. At constant dynode voltage, the signal at mass 30 increased linearly with filament emission current between 1 and 4 milliamps (see Figure 3.9). At constant emission current, the signal increased rapidly as the dynode voltage was increased from 2.3 to 2.6 kilovolts. But voltages higher than 2.6 kV caused the signal to decrease (Figure 3.10). It was later found that the signal improved significantly when a 50 ohm-to-ground shunt was inserted at the input of the F-100T Amplifier/Discriminator.

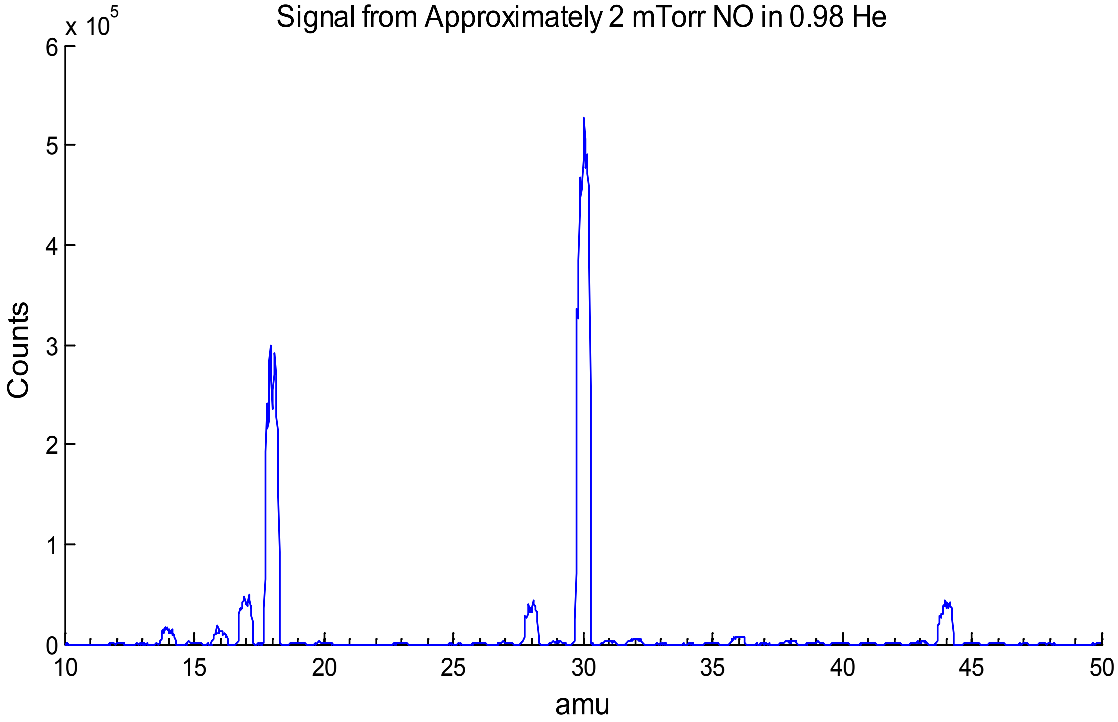

Figure 3.8 – Mass spectrum with emission current 1mA and dynode voltage 2.6kV

Figure 3.9 – Tuning the emission current on the quadrupole for optimal signal.

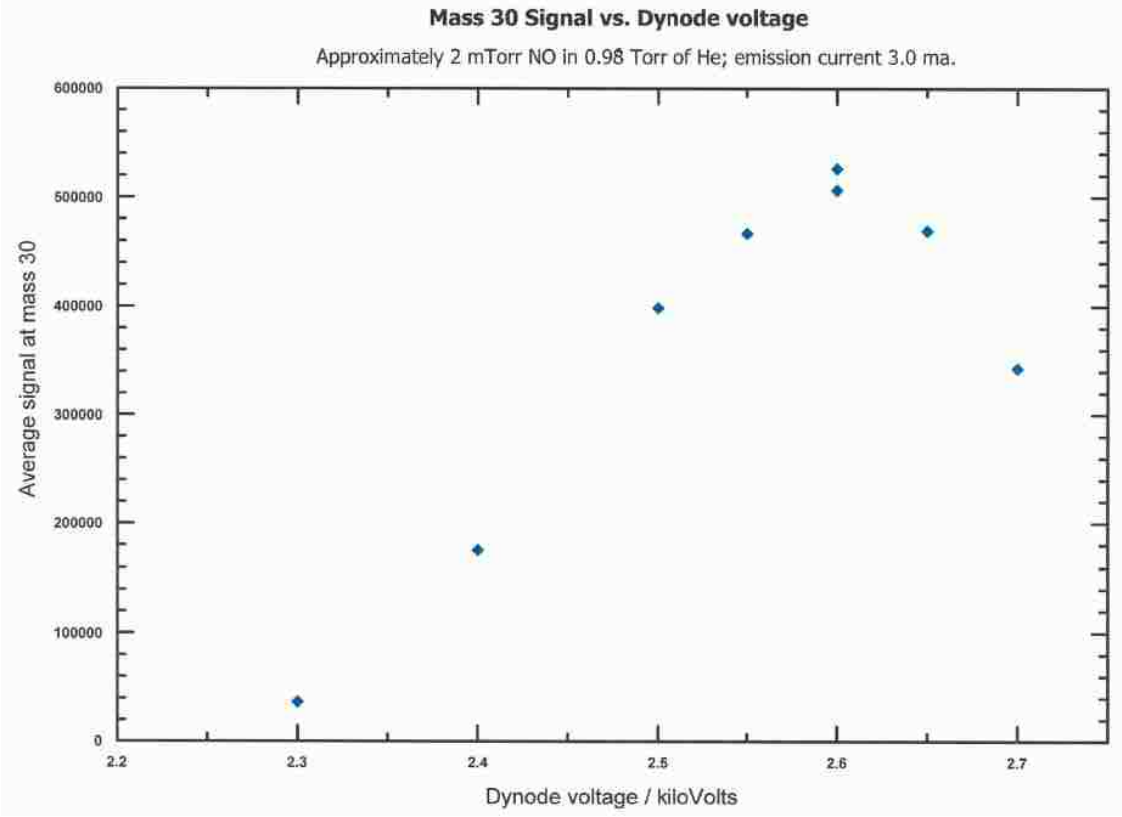

Figure 3.10 – Tuning the dynode voltage for optimal detection.

3.6 Detecting 2-Hydroxyethyl-Peroxy Radical

Attempts were made to make $\cdot CH_2CH_2OH$ radical by reacting hydrogen atoms with 2-iodoethanol.

$$H + ICH_2CH_2OH \rightarrow HI + \cdot CH_2CH_2OH$$

The rate constant for this reaction has not been measured, but similar reactions of H with alkyl iodides are reasonably fast ($k \sim 1\times10^{-11}$ cm^3 molecule^{-1} s^{-1}). Hydrogen atoms were generated by flowing a mixture of 1% H_2/Argon through a microwave discharge. A separate flow of He was bubbled through liquid 2-iodoethanol at room temperature, on the low pressure side of the flow controller. The vapor pressure of iodoethanol is not known. The two flows were combined in the flow tube, approximately 70 cm from the pinhole. The sliding injector was removed for this experiment.

The current quadrupole setup uses ¾ inch diameter rods and a 2.1 MHz 300 watt power supply. According to the Extrel literature, this is designed for the mass range of 1 to 120 amu. The parent peak of iodoethanol is 172. While we have occasionally observed a signal at 172, its appearance depends on the quadrupole tuning and the peak is distorted and much weaker than it should be compared to lower mass peaks. Also for this experiment the masses at 127 (I atoms) and 128 (HI) are useful signals. These were consistently observed, but weaker than expected. The older quadrupole electronics that are in storage have a 1.2 MHz 100 watt power supply; according to Extrel this would extend the upper range to 200 amu.

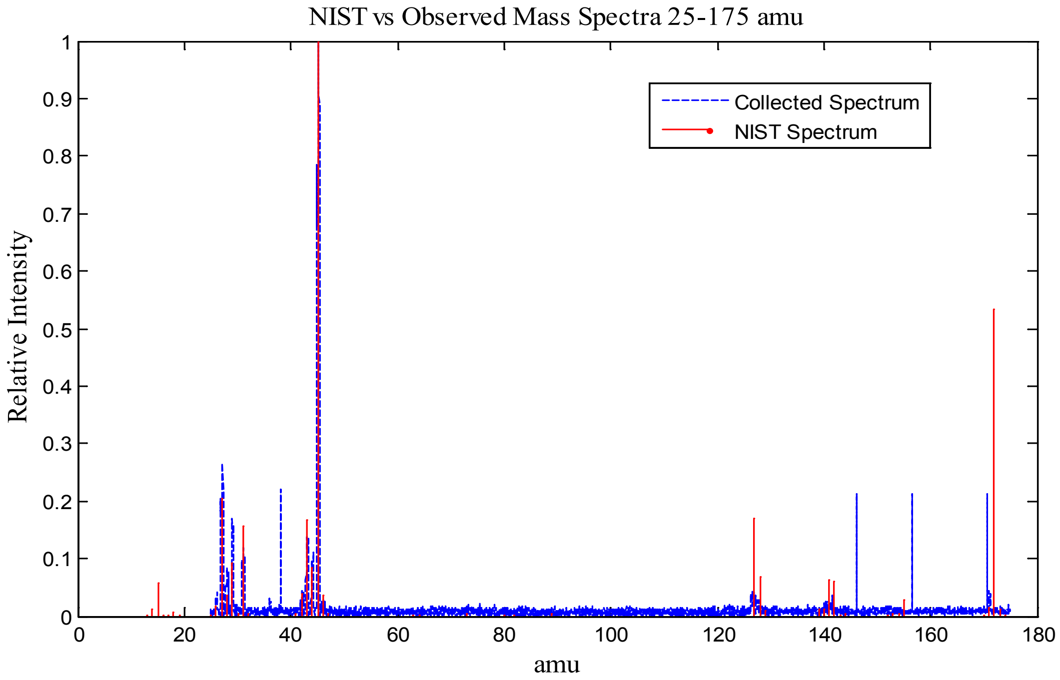

Figure 3.9- NIST data compared to DFMS collected data for iodoethanol

In our system, the strongest peak observed for iodoethanol is at mass 45 ($C_2H_5O^+$), in agreement with the spectrum recorded in the NIST WebBook.(See Figure 3.11) According to the latter, the parent peak at 172 should be next strongest. Other significant peaks occur at 27, 31, 43 and 127.

When the hydrogen discharge is on, evidence for the above reaction is as follows: the signal at mass 45 decreases; the signals at 127 and 128 increase; at the conclusion of flowing for 4 hours, the cold trap protecting the rotary pump has a red deposit (iodoethanol is colorless); when the trap comes to room temperature, a strip of starch iodide paper turns blue, confirming the presence of I_2.

As the flow of He through the bubbler was decreased by a factor of two, and then by another factor of two, the amount of iodoethanol being destroyed, as judged by the decrease in the mass 45 signal, decreased by only ~20%, suggesting that the limiting reagent was the hydrogen atom concentration, not the iodoethanol.

3.7 Conclusion

The DFMS has shown to be a viable working system. The chamber maintains high vacuum, allowing for low background in the mass spectra. The quadrupole mass spectrometer is functional and discriminating masses appropriately; however, its detection limits still need to be tested. The flow cell is holding vacuum and has no sign of leakage. All the parts, gauges, controllers, plumbing, electrical systems, computer software, vacuums, and monitors appear to be in full function allowing for a working discharge-flow mass spectrometer.

4 FUTURE WORK WITH DISCHARGE FLOW MASS SPECTROMETER

4.1 Summary

Future work with the DFMS will investigate the effects of water vapor on the kinetics and product branching ratio of the reaction of organic peroxy radicals with nitric oxide.

4.2 Peroxy Radicals in the Troposphere

Organic peroxy radicals (RO_2) in the atmosphere are intermediates in the combustion of hydrocarbons and serve as precursors for tropospheric ozone formation.[73] Peroxy radicals are produced through hydrogen extraction by atmospheric radicals, followed by the addition of O_2 to the radical site on the hydrocarbon. The reaction mechanism is summarized by reactions 4.1 and 4.2:

$$RH + (OH, Cl, NO_3) \rightarrow R + (H_2O, HCl, HNO_3) \qquad (4.1)$$

$$R + O_2 \rightarrow RO_2 \qquad (4.2)$$

The reaction of RO_2 with NO produces two different products, as shown in reactions 4.3 and 4.4.

$$RO_2 + NO \rightarrow RO + NO_2 \qquad (4.3)$$

$$RO_2 + NO \rightarrow RONO_2 \qquad (4.4)$$

$$NO_2 + h\nu \rightarrow NO + O \qquad (4.5)$$

$$O + O_2 \rightarrow O_3 \qquad (4.6)$$

RO and $RONO_2$ are intermediates to tropospheric pollution, and the photolysis of NO_2 is the primary source of tropospheric ozone (Reactions 4.5 and 4.6). Alkoxy radicals (RO) react with oxygen to produce aldehydes and HO_2. HO_2 is the simplest and most abundant peroxy radical and contributes to pollution by the same mechanism as other peroxy radicals (reactions 4.3 and 4.4). Organic nitrates ($RONO_2$), the product of reaction 4.4, are stable and relatively inert. This inertness and stability permits organic nitrates to be carried by the wind to adjacent regions. They eventually break down (due to heat) into NO_2 and RO radicals, which then allows for reaction 4.3 to occur, leading to ozone production. This cascade of events provides a mechanism for pristine environments to become polluted.

Previous work has been done to understand the branching ratio of reactions 4.3 and 4.4 as a function of the R-group size, but no one has studied the kinetics or branching ratio of these reactions as a function of water-vapor. The branching ratio is defined as the ratio of reaction 4.3 and 4.4 ($k_{4.4}/k_{4.4}$).

Previous experimental work shows that the presence of water vapor perturbs reactions 4.5 and 4.6.

$$HO_2 + NO \rightarrow OH + NO_2 \qquad (4.5)$$

$$HO_2 + NO \rightarrow HONO_2 \qquad (4.6)$$

The product branching ratio ($k_{4.5}/k_{4.6}$) is perturbed in favor of increased nitrate production ($HONO_2$). Butkovskaya et al.[74] showed that at 50% relative humidity production of HNO_3 increased by 800%. They hypothesized that water forms a mono-hydrated complex with peroxy radicals. An HO_2-H_2O complex has been observed experimentally by Suma et al.[34]An analysis of published data by Butkovskaya et al. supports the hypothesis that water complexation of RO_2 leads to increased nitrate production.[74] Butkovskaya et al. depict the reported product branching ratio as a function of the percentage of HO_2 that is complexed with water which shows a clear relationship between increased nitrate production and complexation with water.

Previous work[75] demonstrates that organic peroxy radicals form water complexes and it is proposed that their reactions with NO can lead to increased production of organic nitrates in the troposphere. In a recent high level *ab initio* study, Clark et al.[76] demonstrated theoretically the existence of other peroxy radical-water complexes. Perturbation to the product branching ratio favoring formation of $RONO_2$ is speculated to occur because of the formation of a radical-molecule complex. The production of NO_2 is caused by NO removing oxygen from the peroxy radical at the nitrogen site. The NO bond is formed when the NO_2 rotates to attach to RO. It is proposed that a water complex provides a chaperone whereby the NO_2 is maintained close to the RO through hydrogen bonding. The longer the NO_2 has to interact with the RO at close proximity, the more likely the formation of $RONO_2$. The work presented in Chapter 2 with the β-HEP self-reaction supported the theory that complexation of peroxy radicals with water increases the rate of reaction. Although this discovery is of importance to the atmospheric science community, the perturbation of the branching ratio of β-HEP + NO towards more organic nitrate formation has more direct effects on the atmosphere due to the ability to pollute pristine environments through long-range transport.

4.3 Kinetic Model of HydroxyethylPeroxy Radical and NO

A kinetic model of the reaction mechanism was built using FACSIMILE to aid in the analysis of the kinetic data. This allows for secondary chemistry to be explored in order to assure that significant sources, sinks, or pathways of analyte molecules are accounted for in rate calculations.

$$HOCH_2CH_2O_2 + \text{wall} \rightarrow \text{Products} \tag{4.7}$$

$$HOCH_2CH_2 + O_2 \rightarrow HOCH_2CH_2O_2 \tag{4.8}$$

$$HOCH_2CH_2O_2 + NO \rightarrow HOCH_2CH_2O + NO_2 \tag{4.9}$$

$HOCH_2CH_2O_2 + NO \rightarrow HOCH_2CH_2ONO_2$ (4.10)

$HOCH_2CH_2O_2 + HOCH_2CH_2O_2 \rightarrow$ Products (4.11)

$HOCH_2CH_2O_2 + H_2O \rightarrow HOCH_2CHO_2\text{-}H_2O$ (4.12)

$HOCH_2CH_2O_2\text{-}H2O + NO \rightarrow HOCH_2CH_2ONO_2$ (4.13)

$HOCH_2CH_2O + O_2 \rightarrow HO_2 + HOCH_2CHO$ (4.14)

$HOCH_2CH_2O_2 + HO_2 \rightarrow$ Product (4.15)

$HOCH_2CH_2 + NO \rightarrow$ Products (4.16)

The reactions outlined above constitute the reactions used in the model. This model allows data to be fit and analyzed for determination of the rate constant, and also aids in predicting probable effects from water vapor. These reactions are a small sample to demonstrate the complexity inside the cell. To minimize effects from undesired chemistry, the concentration of ICH_2CH_2OH in the model is orders of magnitude smaller than $[O_2]$. This will produce pseudo first-order conditions whereby the relative concentrations of O_2 will remain unchanged. Figure 4.1 show the results of the model run for 40 milliseconds. As suspected, CH_2CH_2OH reacts

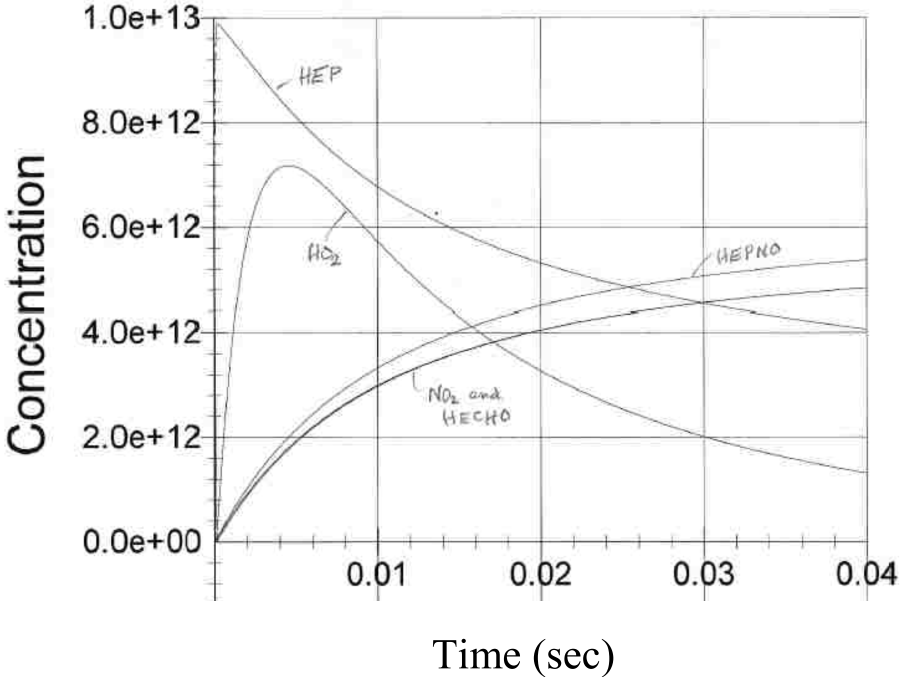

Figure 4.1- The kinetic model of HEP + NO with no H_2O present

quickly with O_2 to form HEP. As HEP reacts with NO, both NO_2 and $HOCH_2CH_2ONO_2$ are formed.

4.4 Experimental Method

The detection method for the HEP + NO reaction must include sufficient selectivity, sensitivity, and response time to obtain the necessary kinetic information. It is necessary to measure the time-resolved concentration of the reactants and products simultaneously. The DFMS described in Chapter 3 should be suitable for this reaction.

Figure 4.2 outlines the proposed settings of the DFMS. The primary He gas flow will introduce various water-vapor concentrations into the system. Atomic hydrogen will be produced through a microwave discharge and introduced into the cavity. Through the sliding injector,

$HOCH_2CH_2I$ along with O_2 will be added to the system. The appropriate NO, NO_2, CH_2CH_2OH, $HOCH_2CH_2OO$, HI peaks will monitored on the mass spectra

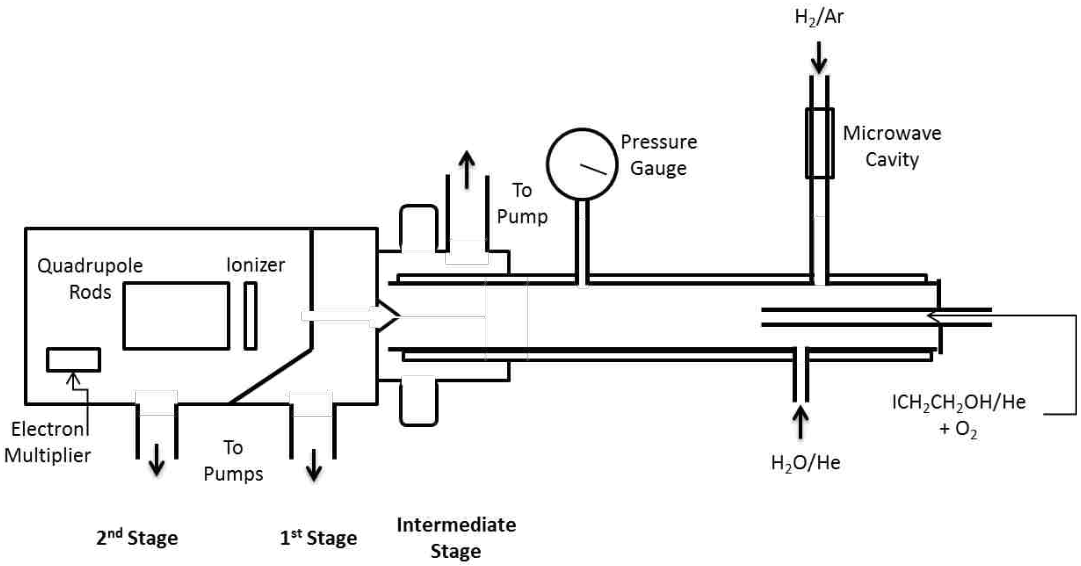

Figure 4.2 – DFMS setup for studying the kinetics of the HEP + NO reaction

5 SUMMARY

This thesis was written to present studies related to the field of atmospheric chemistry. The first portion outlines the importance for understanding atmospheric reactions and their relation to pollution. The β-HEP self-reaction results, combined with the work from Butkovskaya on water enhancement of HO_2 + NO, provides motivation for further investigation into the effects of water on other peroxy radical reactions. To further these investigations, a discharge flow mass spectrometer was engineered. The DFMS serves as a simple and ideal way to investigate water vapors effects on peroxy radical reactions. To correctly predict pollution levels, atmospheric models need to be adjusted to include the rate enhancements demonstrated in this work. The implications of these findings promote the path of further discovery of peroxy radical reactions enhancements through the formation of pre-reactive complexes between radicals and polar molecules such as water, methanol, and ammonia. Furthermore, water vapor catalysis will become increasingly more significant in light of global warming increasing water vapor concentrations in the troposphere.

BIBLIOGRAPHY

1. Howard, C. J., KINETIC MEASUREMENTS USING FLOW TUBES. *Journal of Physical Chemistry* **1979,** *83* (1), 3-9.

2. Bell, M. L.; Davis, D. L.; Fletcher, T., A retrospective assessment of mortality from the London smog episode of 1952: The role of influenza and pollution. *Environmental Health Perspectives* **2004,** *112* (1), 6-8.

3. Lindsey, A. J., THE PHOTOCHEMISTRY OF AIR POLLUTION. *Chemistry & Industry* **1962,** (2), 86-87.

4. EPA What Are the Six Common Air Pollutants? http://www.epa.gov/airquality/urbanair/.

5. EPA State Implementation Plan Development Process. http://www.epa.gov/air/urbanair/sipstatus/process.html.

6. Schonbein, C., Ber. Verh. Nat. Ges. Basel. 1849; Vol. 8, pp 4-5.

7. Fabry, C.; Buisson, H., Journal de Physique. 1913; Vol. 5, pp 196-206.

8. Leighton, P. A., Photochemistry of Air Pollution.

9. Mudway, I., Ozone and the lung: a sensitive issue. Kelly, F., Ed. Molecular Aspects of Medicine: 2000; Vol. 21, pp 1-48.

10. Schlink, U.; Herbarth, O.; Richter, M.; Dorling, S.; Nunnari, G.; Cawley, G.; Pelikan, E., Statistical models to assess the health effects and to forecast ground-level ozone. *Environmental Modelling & Software* **2006,** *21* (4), 547-558.

11. Fraga, J.; Botelho, A.; Sa, A.; Costa, M.; Quaresma, M., The Lag Structure and the General Effect of Ozone Exposure on Pediatric Respiratory Morbidity. *International Journal of Environmental Research and Public Health* **2011,** *8* (10), 4013-4024.

12. Bell, M. L.; McDermott, A.; Zeger, S. L.; Samet, J. M.; Dominici, F., Ozone and short-term mortality in 95 US urban communities, 1987-2000. *Jama-Journal of the American Medical Association* **2004,** *292* (19), 2372-2378.

13. Miller, P. R.; Debauer, M. D.; Nolasco, A. Q.; Tejeda, T. H., COMPARISON OF OZONE EXPOSURE CHARACTERISTICS IN FORESTED REGIONS NEAR MEXICO-CITY AND LOS-ANGELES. *Atmospheric Environment* **1994,** *28* (1), 141-148.

14. Ashmore, M. R., Assessing the future global impacts of ozone on vegetation. *Plant Cell and Environment* **2005,** *28* (8), 949-964.

15. Avnery, S.; Mauzerall, D. L.; Liu, J. F.; Horowitz, L. W., Global crop yield reductions due to surface ozone exposure: 1. Year 2000 crop production losses and economic damage. *Atmospheric Environment* **2011,** *45* (13), 2284-2296.

16. Avnery, S.; Mauzerall, D. L.; Liu, J. F.; Horowitz, L. W., Global crop yield reductions due to surface ozone exposure: 2. Year 2030 potential crop production losses and economic damage under two scenarios of O-3 pollution. *Atmospheric Environment* **2011,** *45* (13), 2297-2309.

17. Haagen-Smit, A., Industrial and Engineering Chemistry Research. 1952; Vol. 44, pp 1342-1346.

18. Wallington, T. J.; Dagaut, P.; Kurylo, M. J., Chemical Reviews. 1992; Vol. 92, pp 667-710.

19. Monks, P., Chemical Society Reviews. 2005; Vol. 34, pp 376-395.

20. Finlayson-Pitts, B. J., *Chemistry of the upper and lower atmosphere: theory, experiments, and applications*. San Diego, Ca, USA, 2000.
21. Creasy, D. J.; Evans, G. E.; Heard, D. E.; Lee, J. D., Journal of Geophysical Research. 2003; Vol. 108, p 4475.
22. Roehl, C. M.; Orlando, J.; Tyndall, G.; Shetter, R.; Vasquez, G.; Cantrell, C.; Calvert, J., The Journal of Physical Chemistry. 1994; Vol. 98, pp 7837-7843.
23. Wayne, R.; Barnes, I.; Biggs, P.; Burrows, J.; Canosa-Mas, C.; Hjorth, J.; Lebras, G.; Moortgat, G. K.; Perner, D.; Poulet, G.; Restelli, G.; Sidebottom, H., Atmospheric Environment 1991; Vol. 25A, pp 1-203.
24. Du, J.; Cooper, F.; Fueglistaler, S., Statistical analysis of global variations of atmospheric relative humidity as obserevd by AIRS. *J Geophys Res-Atm* **2012,** *117*, D12315; Gu, G.; Adler, R., Large-scale, inter-annual relations among surface temperature, water vapour and precipitation with and without enso and volcano forcings. *Int J Clim* **2012,** *32*, 1782-1791.
25. Finlayson-Pitts, B. J.; Pitts, J. N., *Chemistry of the Upper and Lower Atmosphere: Theory, Experiments and Applications*. Academic: San Diego, 2000.
26. Sawada, S.; Totsuka, T., Natural and anthropogenic sources and fate of atmospheric ethylene. *Atmos Environ* **1986,** *20*, 821-832.
27. Hamilton, E. J., Jr., Water-vapor dependence of kinetics of self-reaction of HO_2 in gas phase. *J. Chem. Phys.* **1975,** *63*, 3682-3683.
28. Cox, R. A.; Burrows, J. P., Kinetics and mechanisim of the disproportionation of ho2 in the gas phase. *J. Phys. Chem.* **1979,** *83*, 2560-2568.
29. DeMore, W. B., Reaction of HO_2 with O_3 and the effect of water-vapor on HO_2 kinetics. *J. Phys. Chem.* **1979,** *83*, 1113-1118; Hamilton, E. J., Jr.; Lii, R., Dependence on H_2O and on NH_3 of kinetics of self-reaction of HO_2 in gas-phase formation of HO_2-H_2O and HO_2-NH_3 complexes. *Int. J. Chem. Kinet.* **1977,** *9*, 875-885; Sander, S. P.; Peterson, M.; Watson, R. T.; Patrick, R., Kinetics studies of the HO_2 + HO_2 and DO_2 + DO_2 reactions at 298 K. *J. Phys. Chem.* **1982,** *86* (8), 1236-1240.
30. Kircher, C. C.; Sander, S. P., Kinetics and mechanisim of HO_2 and DO_2 disproportionations. *J. Phys. Chem.* **1984,** *88* (10), 2082-91.
31. Lii, R.-R.; Gorse, R. A., Jr. ; Sauer, M. C., Jr.; Gordon, S., Temperature-dependence of the gas-phase self-reaction of HO_2 in the presence of NH_3. *J. Phys. Chem.* **1980,** *84* (8), 813-817.
32. Sander, S. P.; Abbat, J.; Burkholder, J. B.; Friedl, R. R.; Kolb, C. E.; Golden, D. M.; Huie, R. E.; Kurylo, M. J.; Moortgat, G. K.; Orkin, V. L.; Wine, P. H., Chemical Kinetics and Photochemical Data for use in Atmospheric Studies. *Evaluation No. 17, JPL publication 10-6* **2011,** *Jet Propulsion Laboratory, Pasadena*.
33. Kanno, N.; Tonokura, K.; Tezaki, A.; Koshi, M., Water Dependence of the HO2 Self Reaction: Kinetics of the HO2-H2O Complex. *J. Phys. Chem. A* **2005,** *109* (14), 3153-3158; Tang, Y. X.; Tyndall, G. S.; Orlando, J. J., Spectroscopic and kinetic properties of HO_2 radicals and the enhancement of the HO_2 self reaction by CH_3OH and H_2O. *J Phys Chem A* **2011,** *135* (2), 8; Stone, D.; Rowley, D. M., Kinetics of the gas phase HO2 self-reaction: Effects of temperature, pressure, water and methanol vapours. . *Phys Chem Chem Phys* **2005,** *7* (10), 2156.
34. Suma, K.; Sumiyoshi, Y.; Endo, Y., The rotational spectrum of the water-hydroperoxy radical (H2O-HO2) complex. *Science* **2006,** *311* (5765), 1278-1281.
35. Hansen, J. C.; Francisco, J. S., Radical-molecule complexes: Changing our perspective on the molecular mechanisms of radical-molecule reactions and their impact on atmospheric chemistry. *Chem Phys Chem* **2002,** *3* (10), 833–840; Vaida, V., Perspective: Water cluster

mediated atmospheric chemistry. *J Chem Phys* **2011,** *135* (2), 8; Sennikov, P. G.; Ignatov, S. K.; Schrems, O., Complexes and clusters of water relevant to atmospheric chemistry: H2O complexes with oxidants. *Chem Phys Chem* **2005,** *6* (3), 392-412; Staikova, M.; Donaldson, D. J., Water complexes as catalysts in atmospheric reactions. *Physics and Chemistry of the Earth Part C-Solar-Terrestial and Planetary Science* **2001,** *26* (7), 473-478; Grotheer, H. H.; Riekert, G.; Meier, U.; Just, T., Kinetics of the reactions of CH_2OH radicals with O_2 and HO_2. *Phys Chem Chem Phys* **1985,** *89*, 187-191.

36. Clark, J.; Call, S.; Austin, D.; Hansen, J., Computational study of isoprene hydroxyalkyl peroxy radical-water complexes ($C_5H_8(OH)O_2$-H_2O). . *J Phys Chem A,* **2010,** *114* 6534–6541.

37. English, A. M.; Hansen, J. C.; Szente, J. J.; Mariq, A. M., The effects of water vapor on the CH_3O_2 self-reaction and reaction with HO_2. *J Phys Chem A* **2008,** *112* (39), 9220-9228.

38. Stockwell, W. R., On the HO2+HO2 Reaction - Its Misapplication in Atmospheric Chemistry Models. *J Geophys Res-Atm* **1995,** *100* (D6), 11695-11698.

39. Butkovskaya, N.; Rayez, M. T.; Rayez, J. C.; Kukui, A.; Bras, G. L., Water vapor effect on the hno3 yield in the ho2 + no reaction: Experimental and theoretical evidence. *J Phys Chem A* **2009,** *113* (42), 11327-11342.

40. Aloisio, S.; Francisco, J. S., Existence of a hydroperoxy and water (HO2 center dot H2O) radical complex. *J Phys Chem A* **1998,** *102* (11), 1899-1902.

41. Clark, J.; English, A. M.; Fransisco, J.; Hansen, J. C., Computational Study on the Existence of Organic Peroxy Radical-Water Complexes (RO2-H2O). *J. Phys. Chem. A.* **2008,** *112* (7), 1587-1595.

42. Khan, M. A. H.; Cooke, M. C.; Utembe, S. R.; Archibald, A. T.; Derwent, R. G.; Jenkin, M. E.; Morris, W. C.; South, N.; Hansen, J. C.; Francisco, J. S.; Percival, C. J.; Shallcross, D. E., Global analysis of peroxy radicals and peroxy radical-water complexation using the STOCHEM-CRI global chemistry and transport model. *Atmospheric Environment* **2015,** *106* (0), 278-287.

43. Vohringer-Martinez, E.; Hansmann, B.; Hernandez, H.; Francisco, J. S.; Troe, J.; Abel, B., Water catalysis of a radical-molecule gas-phase reaction. . *Science* **2007,** *315* (5811), 497-501; Gerber, R. B.; McCoy, A. B.; Garciavela, A., Photochemical reaction in weakly-bound clusters. *Ann. Rev. Phys. Chem.* **1994,** *45*, 275-314.

44. Bauer, D.; Crowley, J. N.; Moortgat, G. K., The UV spectrum of ethyl peroxy radical and its self-reaction kinetics between 218 and 333 K,. *J. Photochem. and Photobiol. A: Chemistry* **1992,** *A65*, 3530-3538; Boyd, A. A.; Lesclaux., R., The temperature dependence of the rate coefficients for beta-hydroxyperoxy radical self-reactions. *Int. J Chem Kin* **1997,** *29* (5), 323-331.

45. Jenkin, M. E.; Cox, R. A., *J. Phys. Chem.* **1991,** *95*, 3229; Jenkin, M. E.; Hayman, G. D., Kinetics of reactions of primary, secondary and tertiary beta-hydroxyperoxyl radicals - application to isoprene degradation. *J Chem Soc-Faraday Transactions* **1995,** *91* (13), 1911; Jenkin, M. E.; Hurley, M. A.; Wallington, T. J., Investigation of the radical product channel of the ch3och2o2 + ho2 reaction in the gas phase. *J Phys Chem A* **2010,** *114* (1), 408.

46. Anastasi, C.; Muir, D. J.; Simpson, V. J.; Pagsberg, P., Spectrum and mutual kinetics of hoch2ch2o2 radicals. *J Phys Chem A* **1991,** *95* (15), 5791.

47. Lightfoot, P. D.; Cox, R. A.; Crowley, J. N.; Destriau, M.; Hayman, G. D.; Jenkin, M. E.; Moortgat, G. K.; Zabel, F., Organic Peroxy radicals: Kinetics, spectroscopy, and tropospheric chemistry. *Atmos. Environ.* **1992,** *26A*, 1805-1961.

48. Murrells, T. P.; Jenkin, M. E.; Shalliker, S. J.; Hayman, G. D., Laser flash-photolysis study of the uv spectrum and kinetics of reactions of $HOCH_2CH_2O_2$ radicals. . *J Chem Soc. - Faraday Transactions* **1991,** *87* (15), 2351-2360.
49. Atkinson, R.; Baulch, D. L.; Cox, R. A.; Crowley, J. N.; Hampson, R. F.; Hynes, R. G.; Jenkin, M. E.; Rossi, M. J.; Troe., J., Evaluated kinetic and photochemical data for atmospheric chemistry: Volume iii - gas phase reactions of inorganic halogens. *Atmos Chem and Phys* **2007,** *7*, 981-1191.
50. Frisch, M. J.; Trucks, G. W.; Schlegel, H. B.; Scuseria, G. E.; Robb, M. A.; Cheeseman, J. R.; Montgomery, J. A. J.; Vreven, T.; Kudin, K. N.; Burant, J. C. e. a., *Gaussian 03* **2004**.
51. Chang Kon; Kim, J. W., Chan Kyung; Kim, Effects of the basis set superposition error on optimized geometries of trimer complexes (Part I). *Chemical Physics Letters* **2012,** *545*, 112-117.
52. McClurg, R. B.; Flagan, R. C.; Goddard, W. A., The hindered rotor density of states interpolation function. *J Chem Phys* **1997,** *106* (16), 6675-6680; McQuarrie, D. A.; Simon., J. D., *Physical Chemistry: A Molecular Approach.* **1997,** *University Science Books,* , 981-985.
53. Hintsa, E. J.; Zhao, X. S.; Lee., Y. T., Photodissociation of 2-bromoethanol and 2-chloroethanol at 193 nm. *J Chem Phys* **1990,** *92* (4), 2280-2286.
54. Keller-Rudek, H.; Moortgat, G. K., Max-Planck Intitut fur Chemie, Atmospheric Chemistry Division. *MPI-Mainz-UV-Vis Spectral Atlas of Gaseous Molecules* **2013**.
55. K Bogumil, J. O., J. Hormann, S. Voigt, P. Speitz, O.C. Fleischmann, A. Vogel, M. Hartmann, H Kromminga, and H. Bovensmann. et. al Measurements of molecular absorption spectra with the sciamachy pre-flight model: Instrument characterization and reference data for atmospheric remote-sensing in the 230-2380 nm region. *J Photochem Photobio A-Chem* **2003,** *157*, 2; Crowley, J. N.; Simon, F. G.; Burrows, J. P.; Moortgat, G. K.; Jenkin, M. E.; Cox, R. A., The HO_2 radical absorption-spectrum measured by molecular modulation, uv diode-array spectroscopy. *J. Photochem. and Photobiol. A: Chem.* **1991,** *60*, 1-10.
56. Rothman, L. S.; Rinsland, C. P.; Goldman, A.; Massie, S. T.; Edwards, D. P.; Flaud, J. M.; Perrin, A.; Camy-Peyret, C.; Dana, V.; Mandin, J. Y.; Schroeder, J.; McCann, A.; Gamache, R. R.; Wattson, R. B.; Yoshino, K.; Chance, K. V.; Jucks, K. W.; Brown, L. R.; Nemtchinov, V.; Varanasi, P., The HITRAN molecular spectroscopic database and HAWKS (HITRAN Atmospheric Workstation): 1996 edition. *J. Quant. Spectrosc. Radiat. Transfer* **1998,** *60* (5), 665-710.
57. Caralp, F.; Forst, W.; Rayez., M. T., Chemical activation in oh radical-oxidation of 1-n-alkenes. *Phys Chem Chem Phys* **2003,** *5* (3), 476-486; Orlando, J. J.; Tyndall, G. S.; Bilde, M.; Ferronato, C.; Wallington, T. J.; Vereecken, L.; Peeters., J., Laboratory and theoretical study of the oxy radicals in the oh- and cl-initiated oxidation of ethene. *J Phys Chem A* **1998,** *102* (42), 8116-8123.
58. S. Aloisio, Y. L., and J. Francisco, Complete active space self-consistent field and multireference configuration interaction studies of the differences between the low lying excited states of HO2 and HO2-H2O. *Journal of Chemical Physics* **1999,** *110* (18), 9017.
59. Kanno, N.; Tonokura, K.; Koshi, M., Equilibrium constant of the HO2-H2O complex formation and kinetics of HO2+HO2-H2O: Implications for tropospheric chemistry. *J Geophys Res-Atm* **2006,** *111* (D20).
60. Garzon, A.; Cuevas, C. A.; Ceacero, A. A.; Notario, N.; Albaladejo, J., Atmospheric reactions Cl + CH_3-$(CH_2)_n$-OH (n=0-4): A kinetic and theoretical study. *J Chem Phys* **2006,** *125*, 104305.

61. Taatjes, C. A.; Christensen, L. K.; Hurley, M. D.; Wallington, T. J., *J. Phys. Chem. A* **1999,** *103*, 9805.

62. Bauer, D.; Crowley, J. N.; Moortgat, G. K., The UV absorption spectrum of the ethyl peroxy radical and its self-reaction kinetics between 218 333 K. *J. Photochem Photobiol. A: Chem.* **1992,** *A65*, 329-344.

63. Wood, R. W., Phil. Mag.: 1918; Vol. 6, p 1905.

64. SmallWood, H. M., J. Am. Soc.: 1929; Vol. 51, p 1985.

65. Wrede, E., Z. Phys.: 1929; Vol. 54, p 53.

66. Kaufman, F., Proc. R. Soc. Ser. A: London, 1958; Vol. 247, p 123.

67. Clyne, M. A. A.; Thrush, B. A., MECHANISM OF CHEMILUMINESCENT COMBINATION REACTIONS INVOLVING OXYGEN ATOMS. *Proceedings of the Royal Society of London Series a-Mathematical and Physical Sciences* **1962,** *269* (1338), 404-&.

68. Bogan, D. J.; Setser, D. W.; Sung, J. P., HF IR CHEMILUMINESCENCE - VIBRATIONAL AND ROTATIONAL ENERGY DISPOSAL FOR REACTIONS OF FLUORINE-ATOMS WITH FORMALDEHYDE, ACETALDEHYDE, BENZALDEHYDE, AND DIMETHYL ETHER. *Journal of Physical Chemistry* **1977,** *81* (9), 888-898.

69. Foner, S. N.; Hudson, R. L., MASS SPECTROMETRY OF HO2 FREE RADICAL. *Journal of Chemical Physics* **1962,** *36* (10), 2681-&.

70. Phillips, L. F.; Schiff, H. I., MASS SPECTROMETRIC STUDIES OF ATOM REACTIONS .1. REACTIONS IN ATOMIC NITROGEN-OZONE SYSTEM. *Journal of Chemical Physics* **1962,** *36* (6), 1509-&.

71. Ogryzlo, E. A., HALOGEN ATOM REACTIONS .1. ELECTRICAL DISCHARGE AS A SOURCE OF HALOGEN ATOMS. *Canadian Journal of Chemistry-Revue Canadienne De Chimie* **1961,** *39* (12), 2556-&.

72. Kumbhani, S. R.; Cline, T. S.; Killian, M. C.; Clark, J. M.; Keeton, W. J.; Hansen, L. D.; Shirts, R. B.; Robichaud, D. J.; Hansen, J. C., Water Vapor Enhancement of Rates of Peroxy Radical Reactions. *International Journal of Chemical Kinetics* **2015,** *47* (6), 395-409.

73. Finlayson-Pitts, B. J.; Pitts, J. N. J., Chemistry of the Upper and Lower Atmosphere:Theory, Experiments and Apllications. Academic Press: San Diego, 2000.

74. Butkovskaya, N.; Rayez, M.-T.; Rayez, J.-C.; Kukui, A.; Le Bras, G., Water Vapor Effect on the HNO3 Yield in the HO2 + NO Reaction: Experimental and Theoretical Evidence. *Journal of Physical Chemistry A* **2009,** *113* (42), 11327-11342.

75. Stone, D.; Rowley, D. M., Kinetics of the gas phase HO(2) self-reaction: Effects of temperature, pressure, water and methanol vapours. *Physical Chemistry Chemical Physics* **2005,** *7* (10), 2156-2163.

76. Clark, J.; Call, S. T.; Austin, D. E.; Hansen, J. C., Computational Study of Isoprene Hydroxyalkyl Peroxy Radical Water Complexes (C5H8(OH)O-2-H2O). *Journal of Physical Chemistry A* **2010,** *114* (23), 6534-6541.

SUPPLEMENTARY

Technical Drawings

The technical drawings include the technical drawings of the parts designed and machined for the discharge flow mass spectrometer. The machining was done by Hamilton Tools and Engineering, MDC Vacuum, or 80/20 Inc.

This is the collar that clamps down over the skimmer cone onto the skimmer mounting plate.

This is mounting plate for the skimmer cone. This covers the entrance into the first stage of the vacuum chamber.

This is the collar that goes over that glass flow cell. It clamps the glass cell to the new intermediate stage, providing the pressure needed to create the seal around the O-ring.

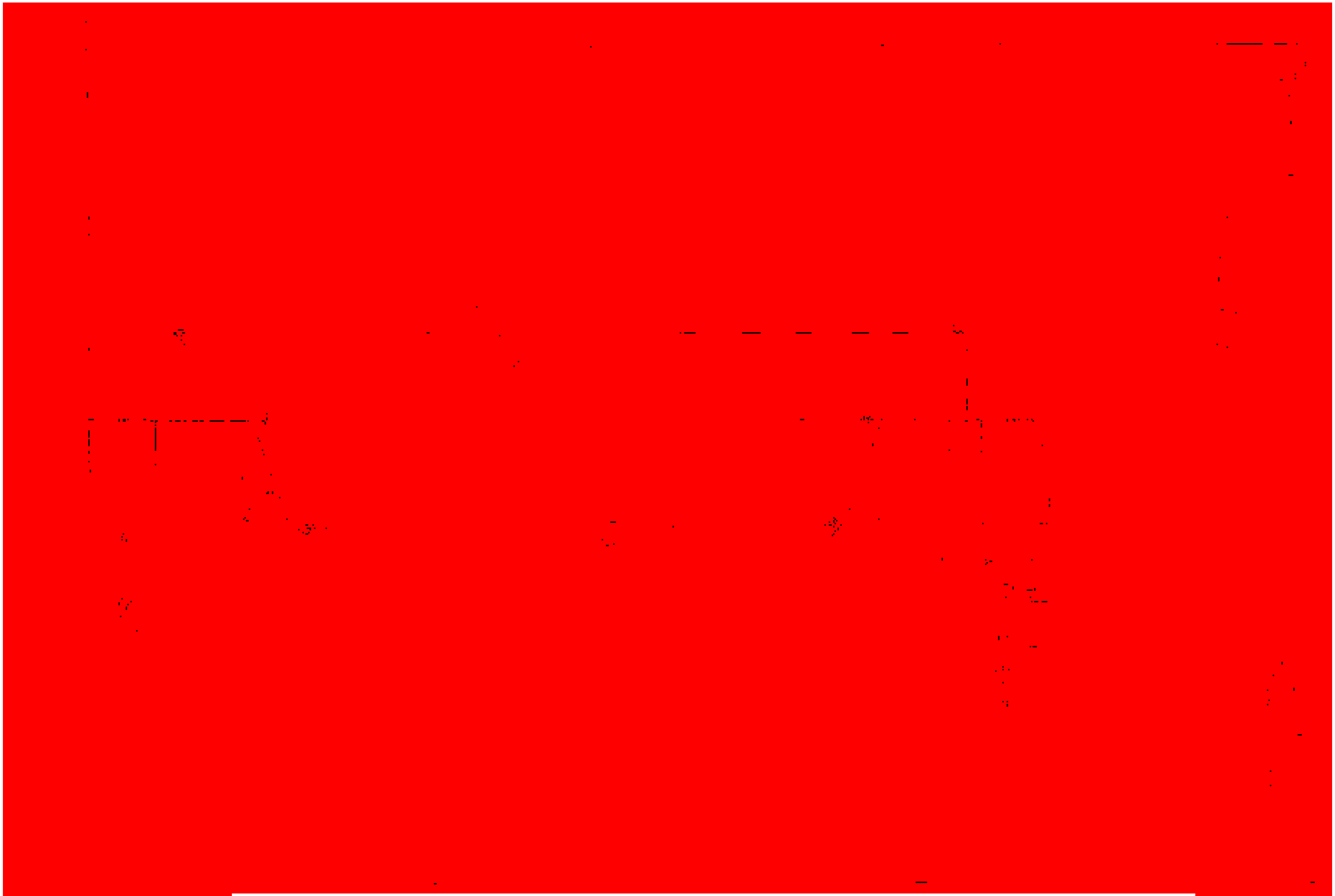

A cut view of the glass flow cell collar.

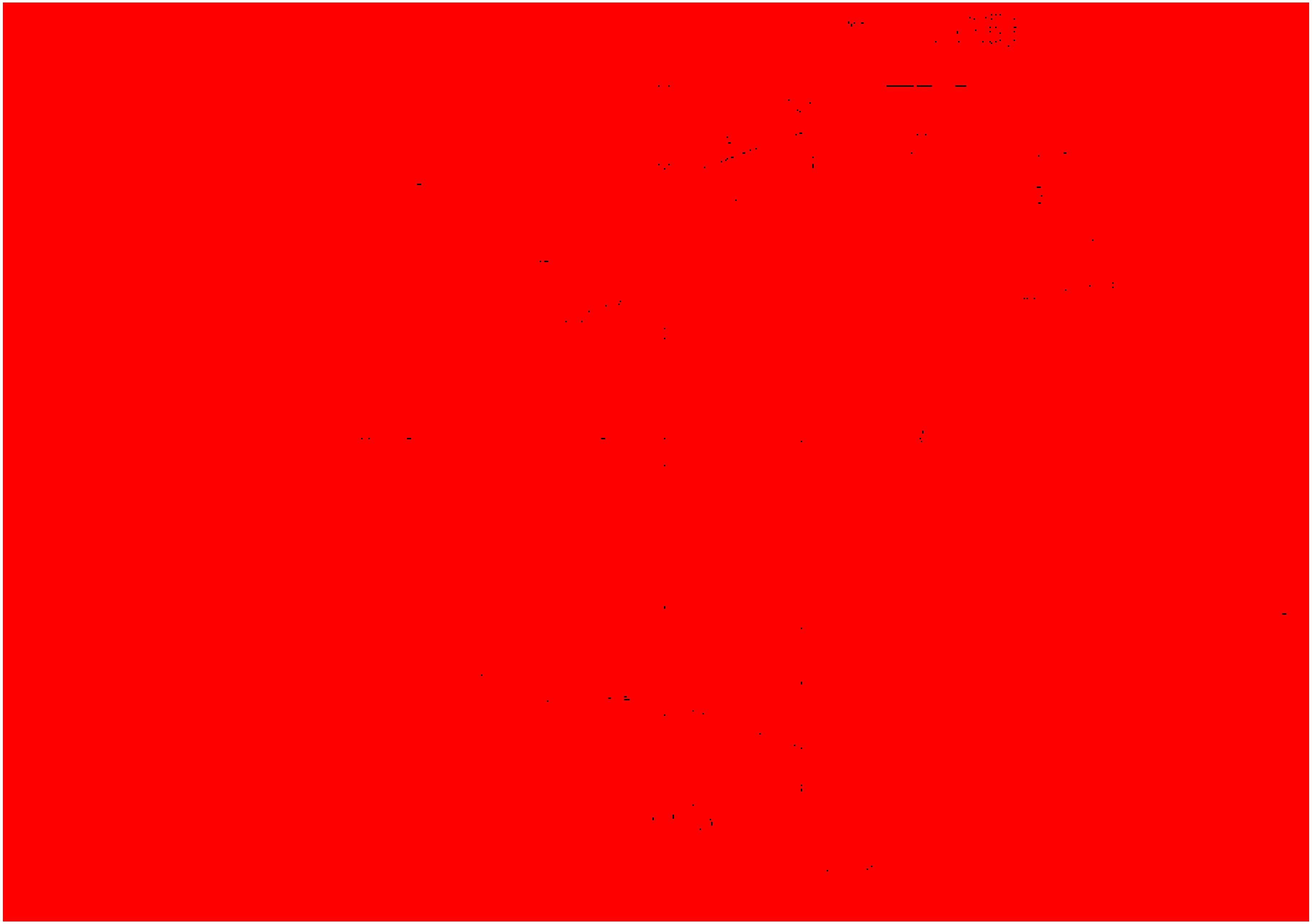

Dimensions of the glass cell flow tube.

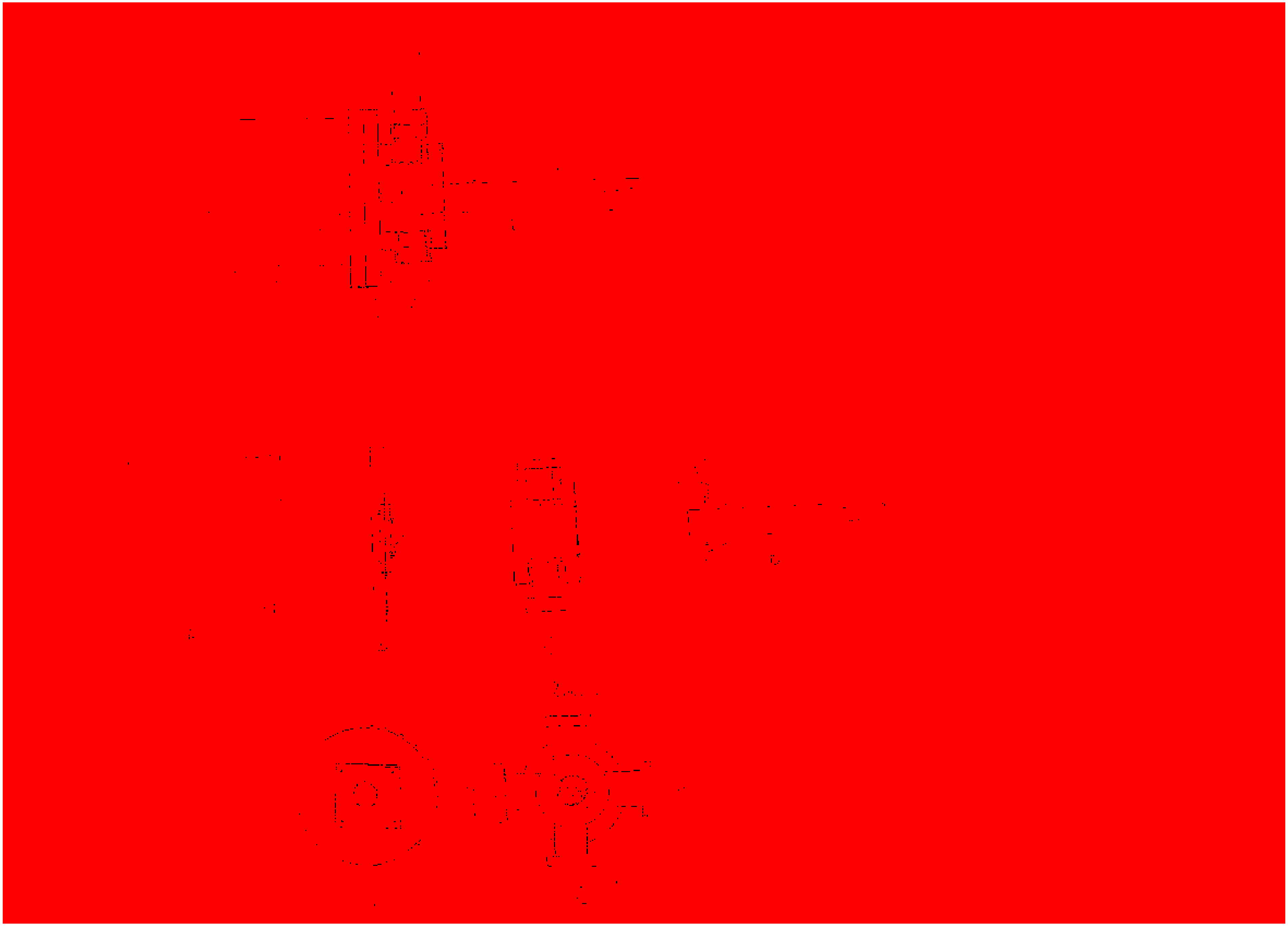

A sketch of how the vacuum chamber (A), the skimmer cone plate (B), the intermediate stage (C), and the flow cell (D) couple together.

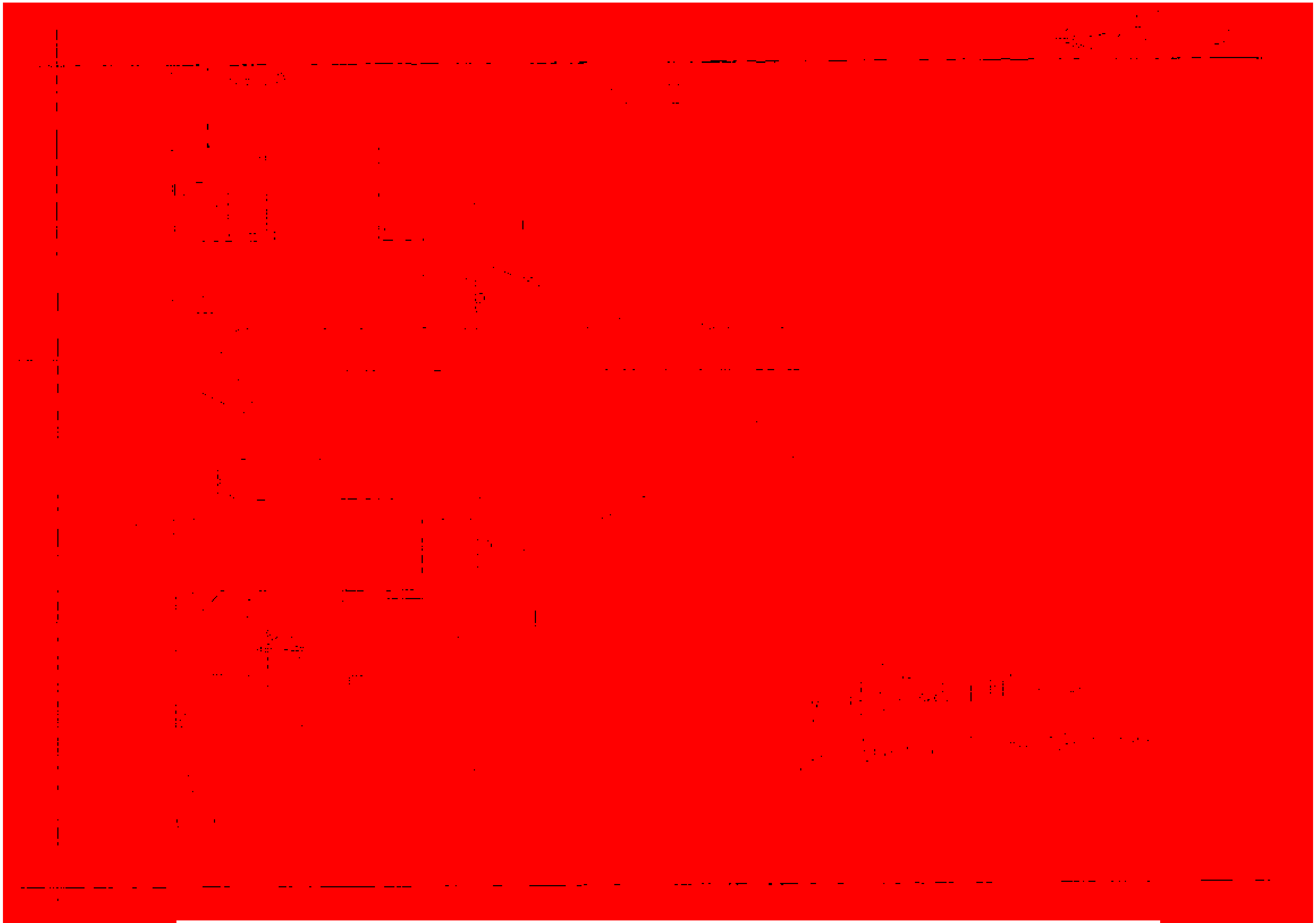

Measurements of the vacuum chamber coupled to the flow cell via the intermediate stage.

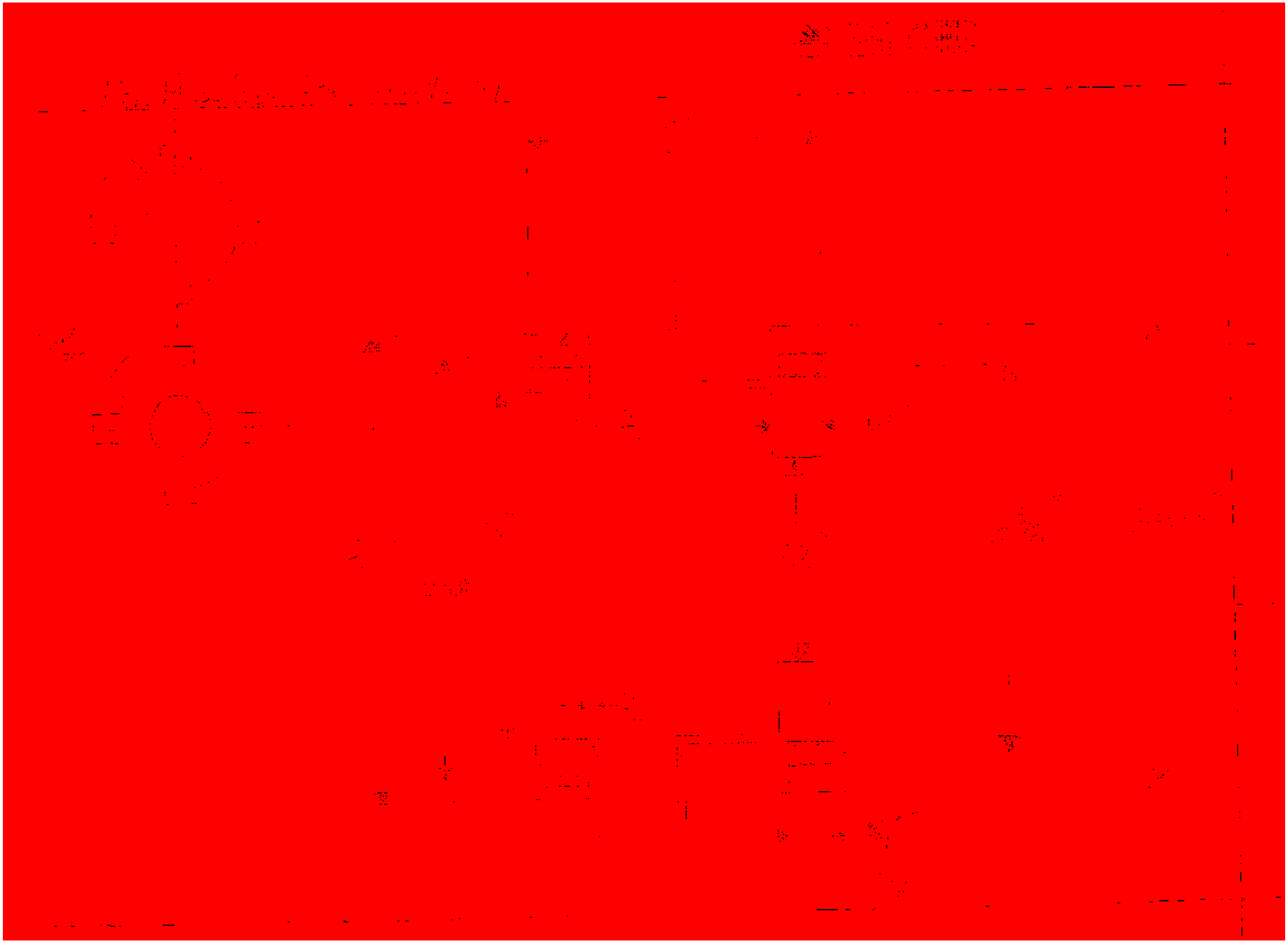

Dimensions of the intermediate stage.

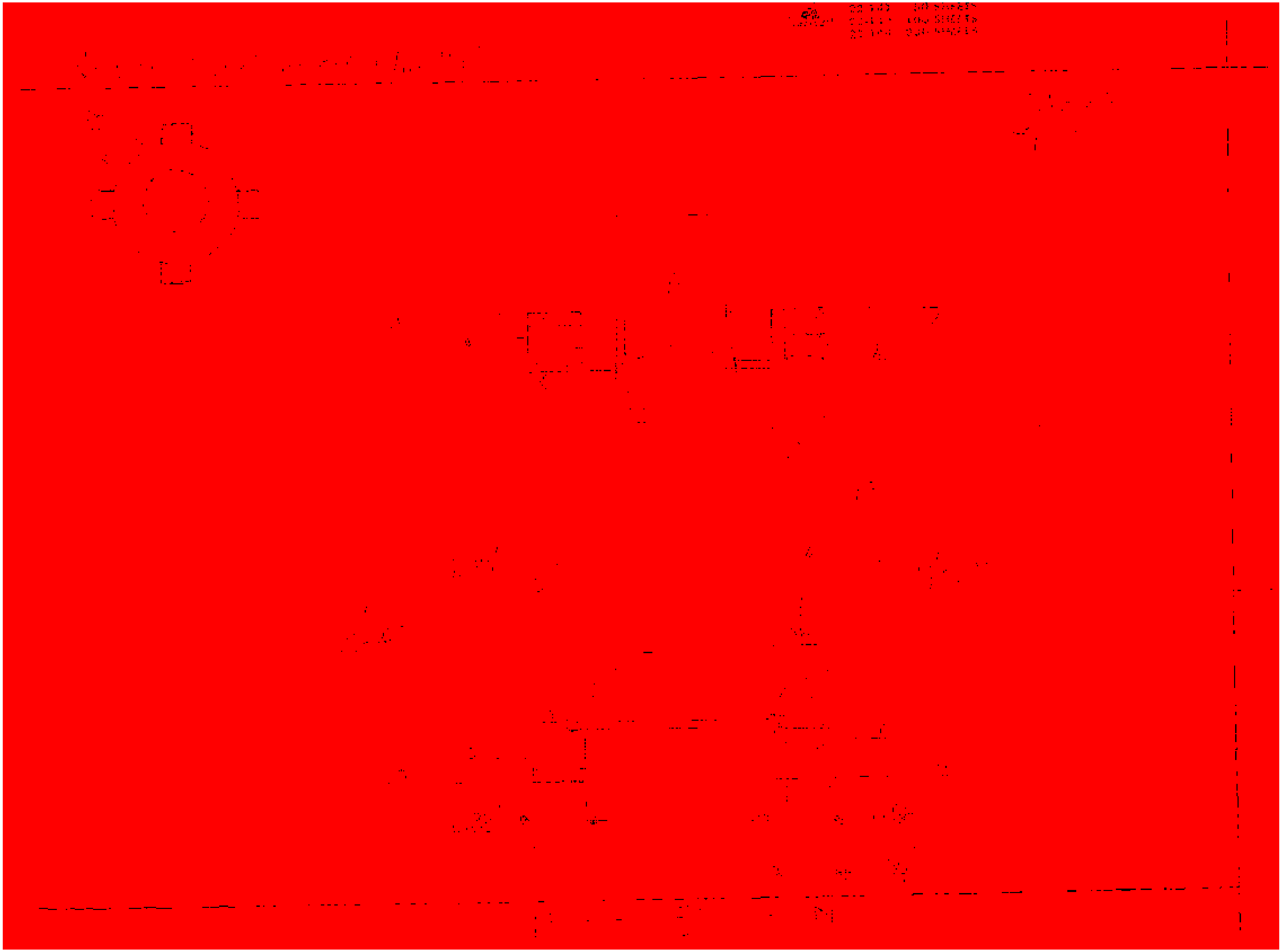

Dimensions of the intermediate stage.

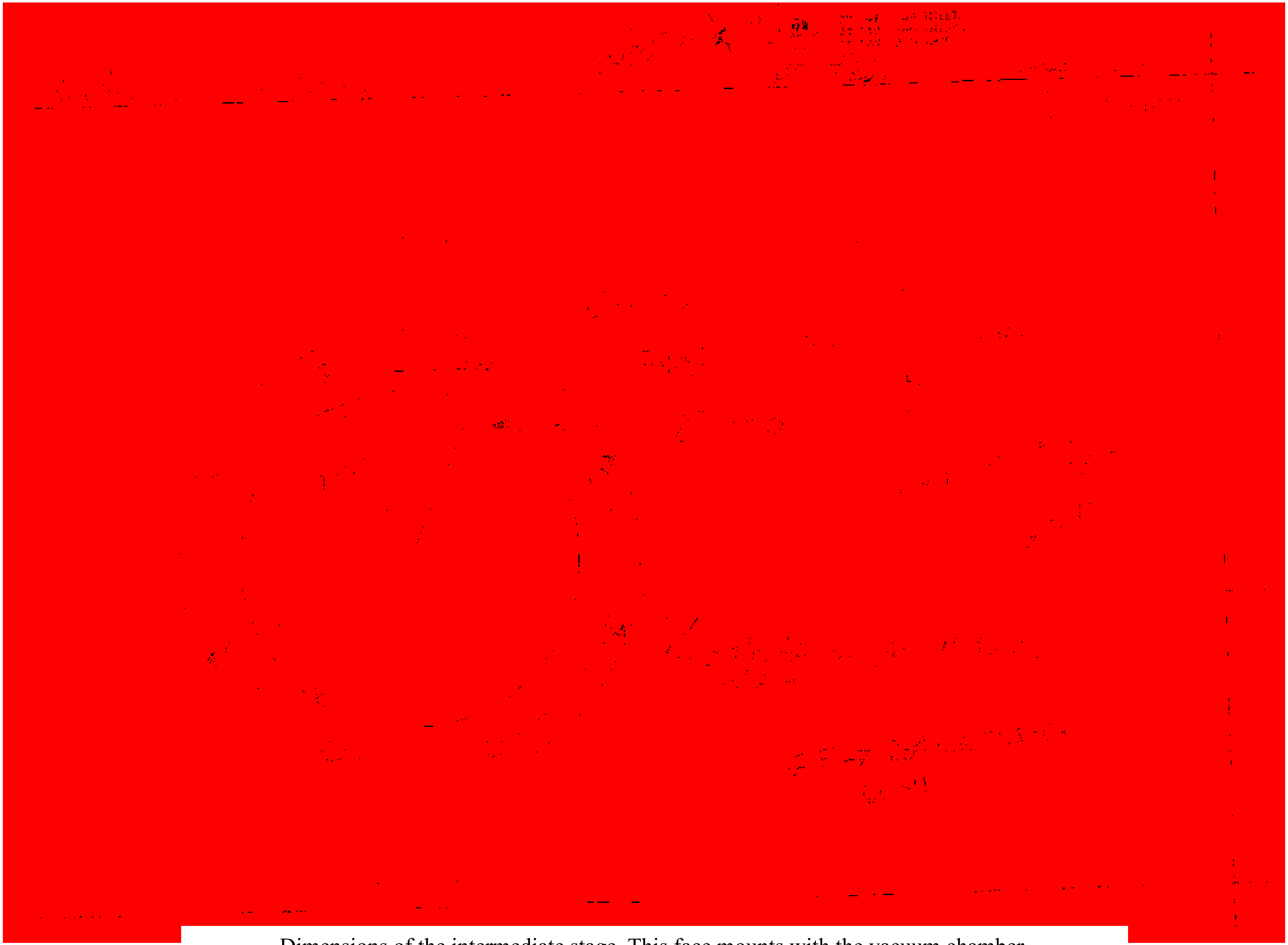

Dimensions of the intermediate stage. This face mounts with the vacuum chamber.

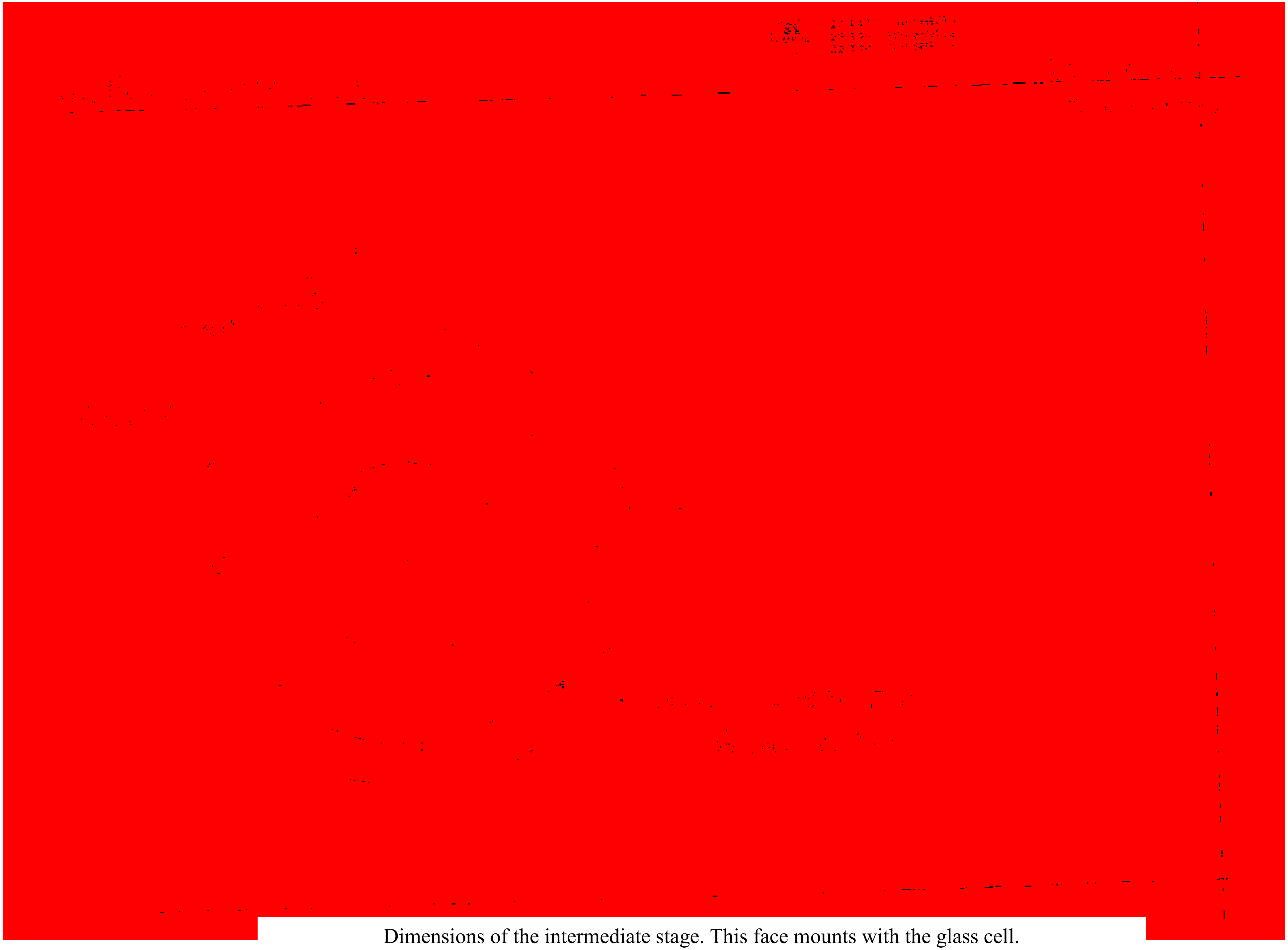

Dimensions of the intermediate stage. This face mounts with the glass cell.

Dimensions of the intermediate stage.

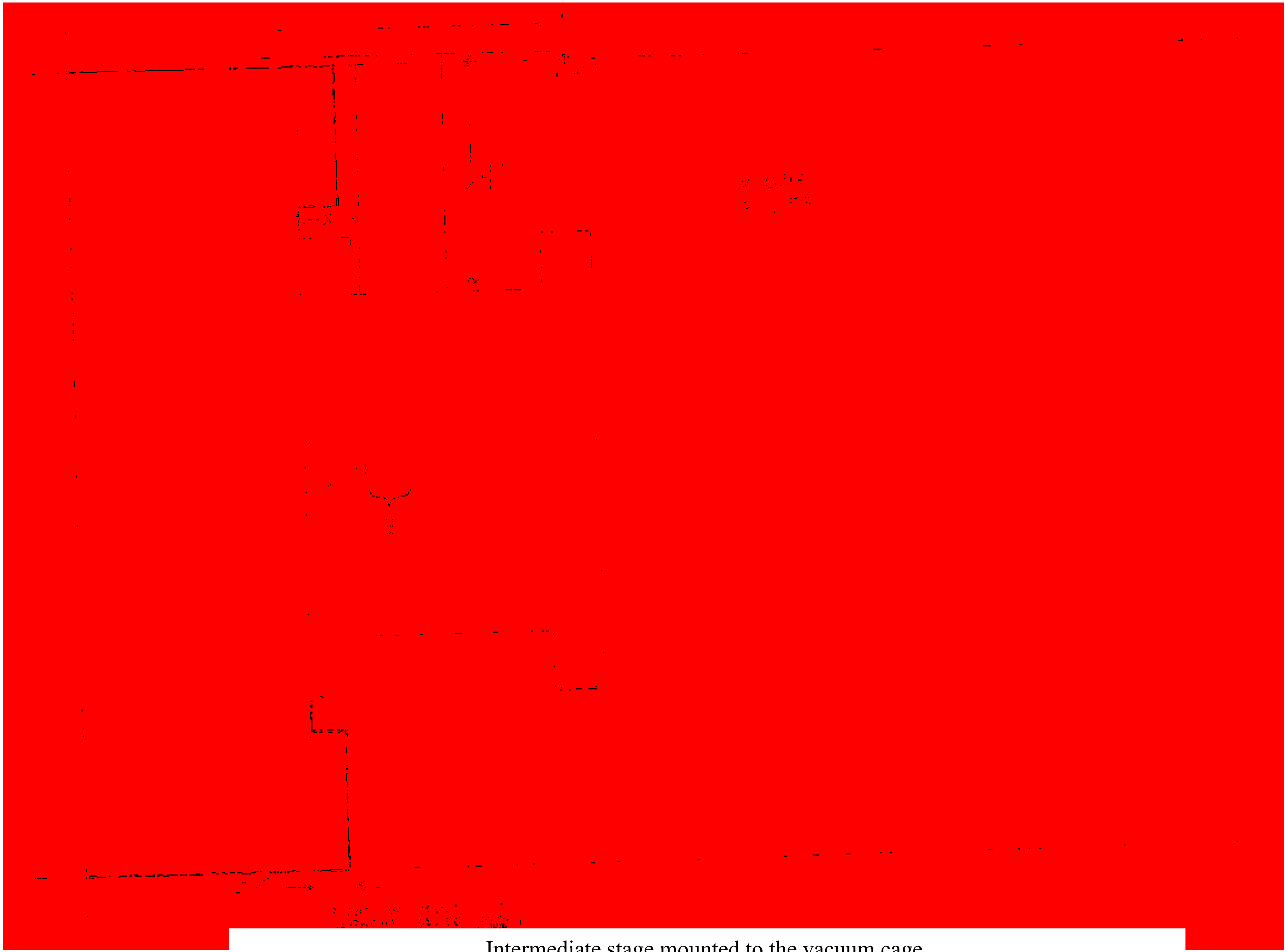

Intermediate stage mounted to the vacuum cage.

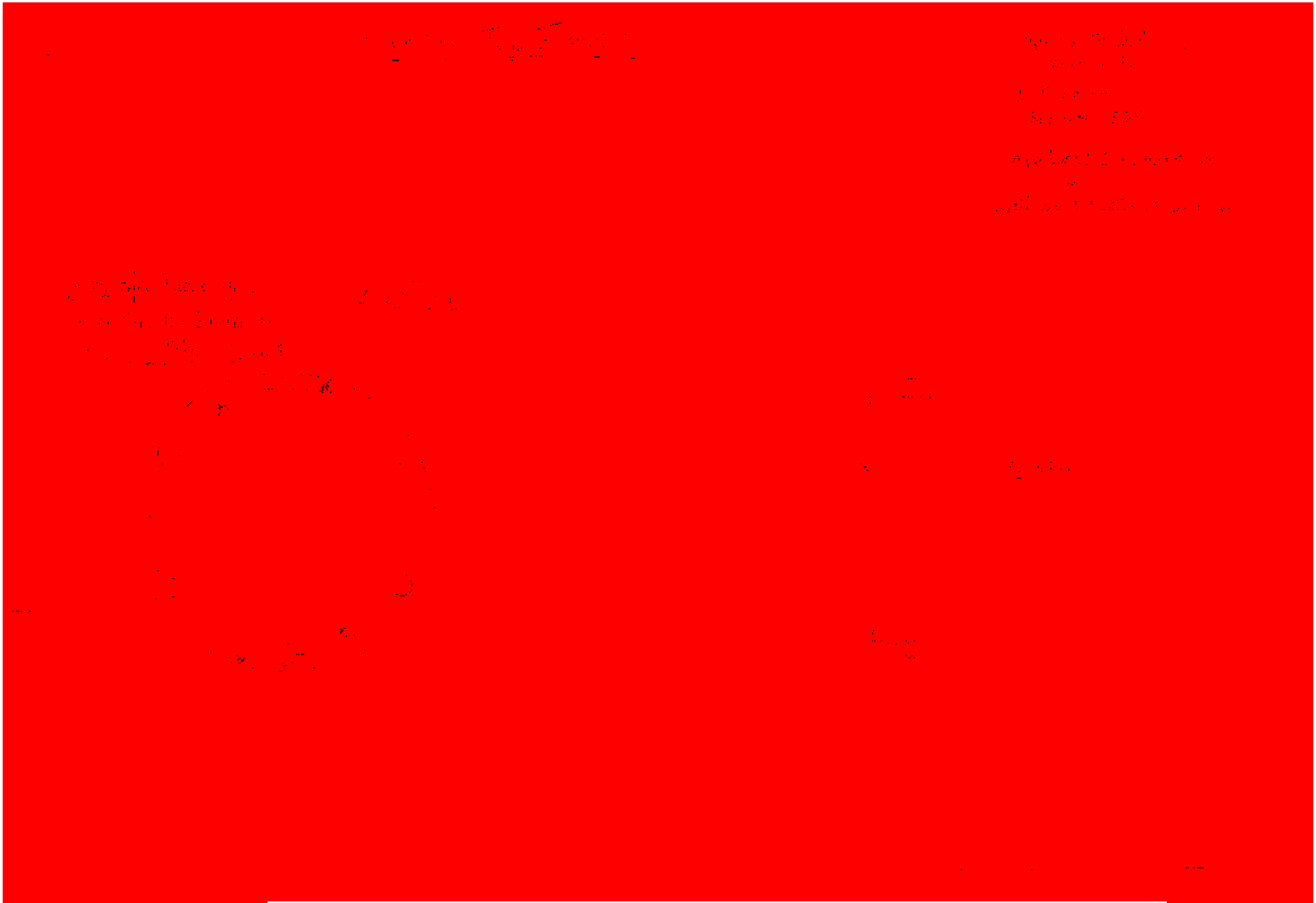

Flanges that cover the LIF ports on the intermediate stage.

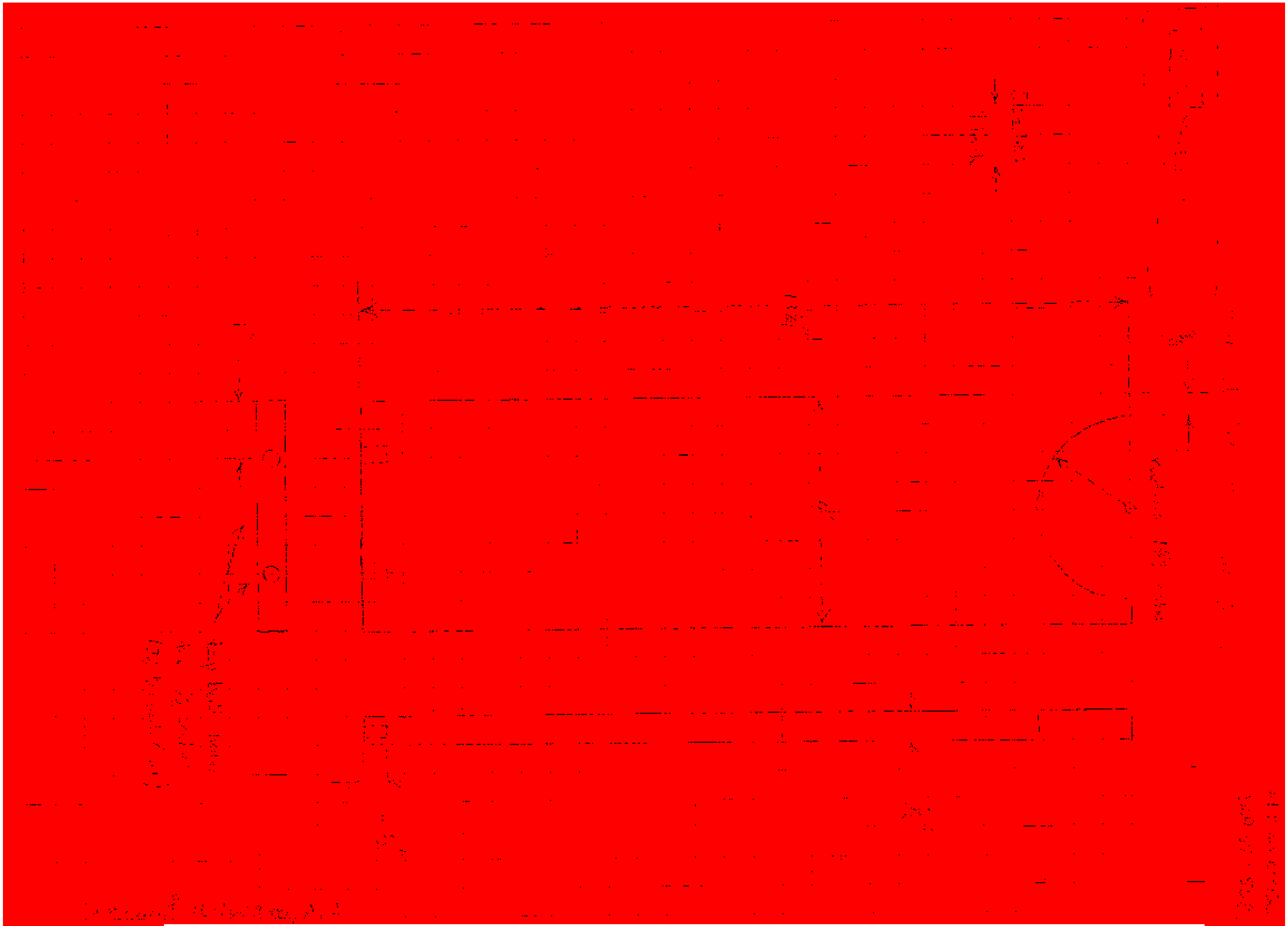

Support beams for the flow cell. These are adjustable up-and-down and side-to-side to allow optimal positioning of the flow cell into the intermediate stage.

Mounting plates for the flow cell support beams to the bread board table top.

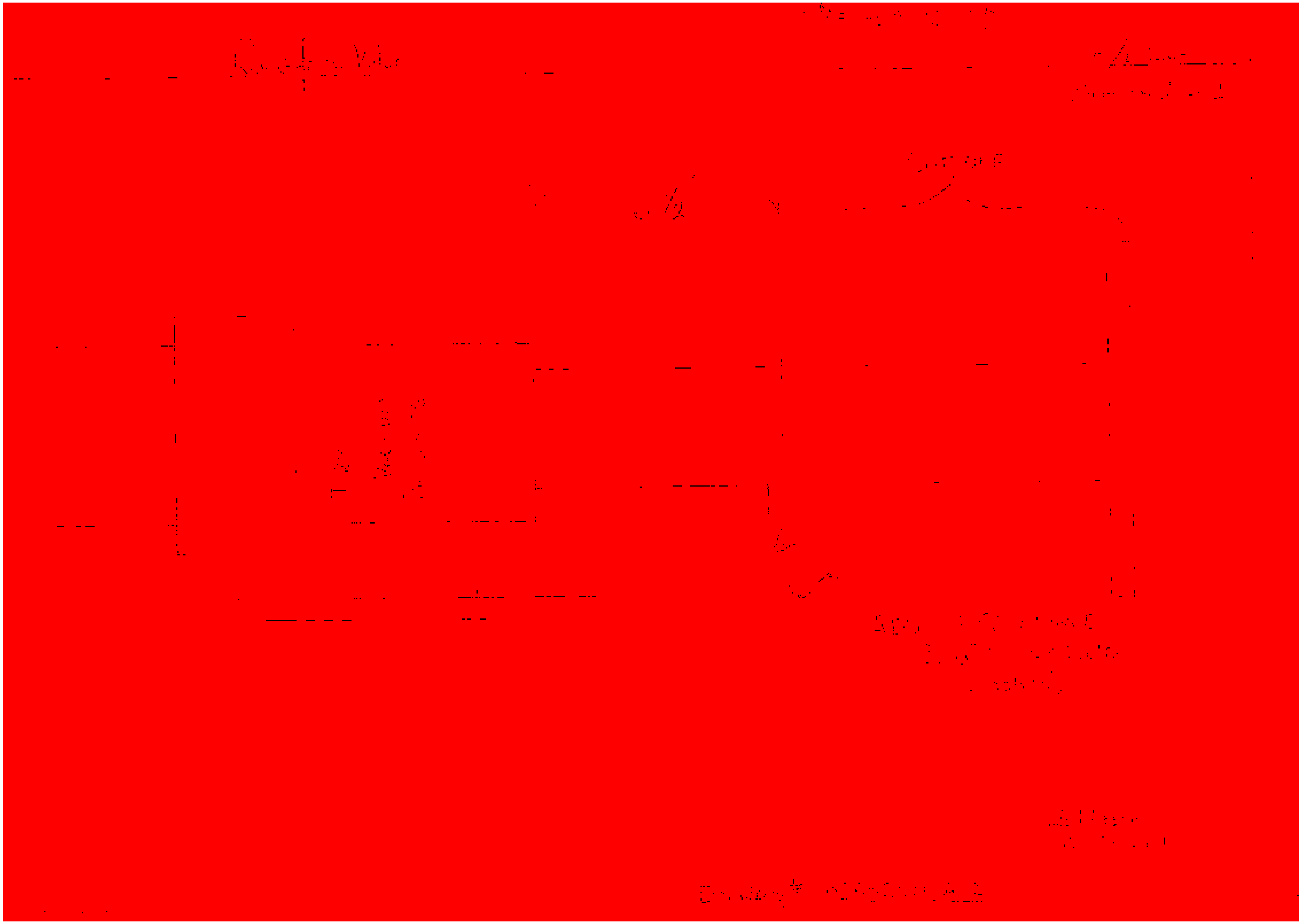

The valve that seals the channel vacuum pump to the intermediate stage.

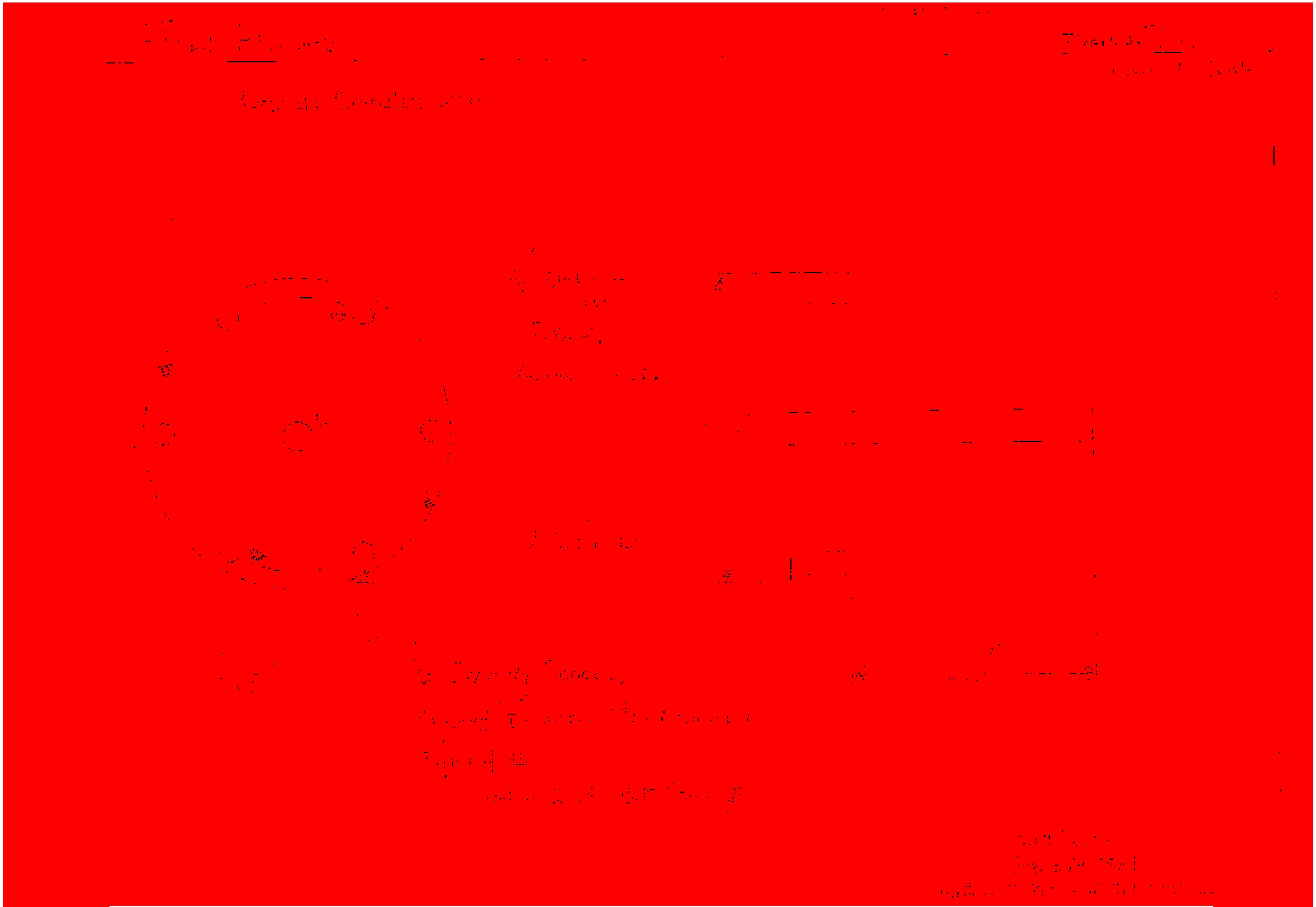

These flanges mount to a port on the vacuum chamber and on the intermediate chamber. They allow the vacuum chamber to be brought back up to atmospheric pressure.

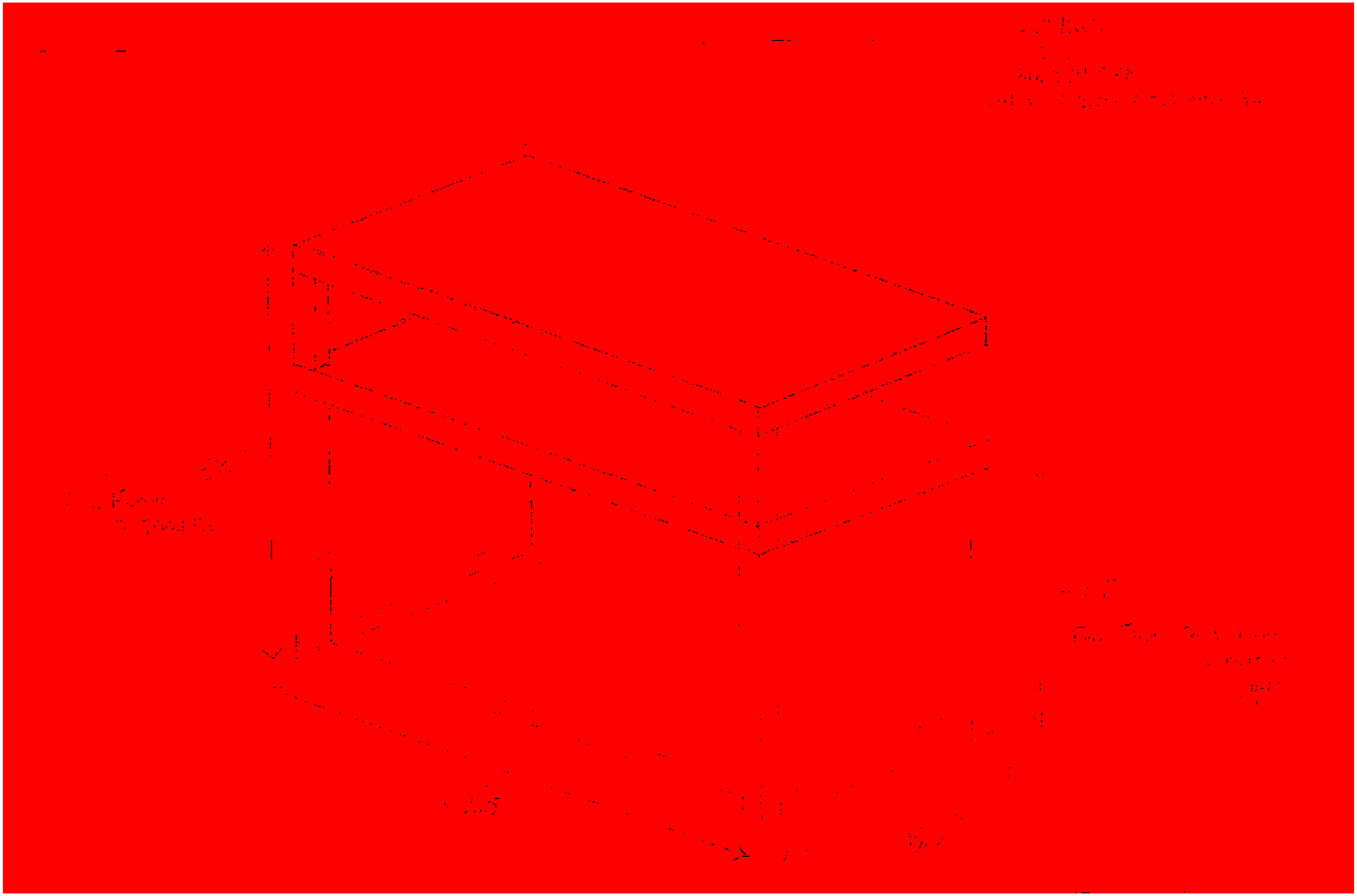

Designs for a table. This table supports the flow cell and couples the vacuum chamber support to another table top.

SUPPLEMENTAL MATERIAL TO CHAPTER 2

S-1 Computational Methods

S.1.1 Partition function calculations

From the Gaussian 03 calculations, the partition function of each conformation of each molecule was calculated according to the theory by McQuarrie and Simon.[43] The overall partition function for a molecule is approximated by the product of its translational, rotational, electronic, and vibrational partition functions, which are assumed to be separable. The expressions for the translational, rotational, and electronic partition functions are:

$$q^T = \frac{V\left(2\pi mkT\right)^{3/2}}{h^3} \qquad \text{(S1)}$$

where V is the volume of the reaction cell, m is the mass of the molecule, k is Boltzmann's constant, h is Planck's constant, and T is temperature;

$$q^R = \left(\frac{kT}{hc}\right)^{3/2}\left(\frac{\pi}{ABC}\right)^{1/2} \tag{S2}$$

where c is the speed of light and A, B, and C are the rotational constants of the molecule;

$$q^E = ge^{-E/(RT)} \tag{S3}$$

where g is the degeneracy of the electronic ground state and E is the zero-point energy of the ground vibrational state. Note that the energy in the partition function for all molecules and geometries must be in reference to the same reference energy.

S.1.2 Vibrational partition function

The vibrational partition function for a molecule is the product of the partition functions for each of its vibrational modes, assuming that the normal vibrational modes of the molecule are independent. The partition function of a vibrational mode can be calculated as the sum of the contributions from each vibrational state,

$$q^V = \sum_v e^{-\beta E_v} \tag{S4}$$

where $\beta = (kT)^{-1}$. The energies of the vibrational states can be calculated according to several models for the vibrational motions. In this calculation, the harmonic oscillator, Morse oscillator, and hindered rotor models were used for each mode according to the model that best approximated the vibrational motion of the mode.

S.1.3 Harmonic oscillator

A harmonic approximation assumes that the energy levels of a vibrational mode are equally spaced. This approximation is accurate for the lowest vibrational states and therefore can be made when only the ground and first excited states are occupied. For a harmonic oscillator, equation S4 becomes

$$q^V = \sum_v e^{-\beta v h c \tilde{\nu}} = \frac{1}{1 - e^{-\beta h c \tilde{\nu}}} \qquad \text{(S5)}$$

where $\tilde{\nu}$ is the fundamental frequency of the vibrational mode. In this calculation, the fundamental anharmonic frequency calculated in Gaussian was used for $\tilde{\nu}$.

S.1.4 Morse oscillator

A Morse oscillator can be used to model vibrational modes that are dissociative. A harmonic oscillator model assumes that all vibrational states are equally spaced and does not account for the possibility that a bond can dissociate with sufficient energy. Therefore, the partition function based on the harmonic oscillator tends to underestimate the true partition function of the mode. The Morse oscillator accounts for the decreasing spacing between the vibrationally excited states and eventually the dissociation of the bond.

The energy levels for the Morse oscillator potential are given by,

$$G(v) = \nu_e\left(v+\frac{1}{2}\right)+x_e\left(v+\frac{1}{2}\right)^2 \tag{S6}$$

where ν_e is the fundamental harmonic vibrational frequency, v is the vibrational quantum number, and x_e is the diagonal element of the X-matrix corresponding to the vibrational mode. If x_e is negative, the bond will eventually dissociate, whereas if x_e is positive there are infinitely many bound states. The bond will dissociate when $G(v)$ achieves a maximum, or at $v^* = -\frac{\nu_e}{2x_e}-\frac{1}{2}$.

Therefore, at the highest energy bound state, $v_{max} = \lfloor v^* \rfloor$ and there are $N = v_{max} + 1$ bound states. For some states, if the vibration primarily involved the stretching of a hydrogen bond, $\widetilde{x}_e$ was calculated from the dissociation energy for the breaking of the hydrogen bond, D,

$$\tilde{x}_e = -\frac{\nu_e^2}{4D} \tag{S7}$$

N was then calculated as $-\frac{\nu_e}{2\tilde{x}_e}$ and rounded to the nearest integer. The partition function was then calculated,

$$q^V = \sum_{v=0}^{v_{max}} e^{-hc(G(v)-G(0)/(kT)} \tag{S8}$$

from $\tilde{x}_e$ to calculate $G(v)$ and $G(0)$.

S.1.5 Hindered rotor

A hindered rotor model was used to model vibrations that involve the rotation of a functional group on the molecule. The calculation of the partition function for a hindered rotor vibration was based on McClurg *et al.*[42]

$$q^V = q_{HO}\left(\frac{r\pi}{\theta}\right)^{1/2} e^{-r/(2\theta)} I_0\left(\frac{r}{2\theta}\right) \tag{S9}$$

where q_{HO} is the partition function calculated as a harmonic oscillator using the fundamental harmonic frequency , and r and θ are defined as

$$r = \frac{\sqrt{2Iw}}{\hbar} \tag{S10}$$

$$\theta = \frac{kT}{\hbar}\sqrt{\frac{2I}{w}} \tag{S11}$$

where w is the barrier height for the hindered rotor (for this complex, the strength of one or two hydrogen bonds), and I is the moment of inertia for the rotation.

S.1.6 Local minima weighting

Three local minimum geometries for the complex and two local minimum geometries for β-HEP are all accessible at room temperature. Therefore the partition function for each of these geometries contributes to the overall equilibrium constant for complex formation. The partition function for a molecule is

$$q = \sum_i e^{-\beta E_i/(kT)} \tag{S12}$$

where *i* denotes all of the states for the molecule. Therefore the partition functions for β-HEP-H_2O and β-HEP are equal to the sums of the partition functions for each of the local minimum geometries if they have a common reference energy. Therefore, the equilibrium constant for the complex formation is equal to

$$K_e = \frac{\dfrac{q_{[HEP-H2O]_1} + q_{[HEP-H2O]_2} + q_{[HEP-H2O]_3}}{V}}{(\dfrac{q_{[HEP]_1} + q_{[HEP]_2}}{V}) \times (\dfrac{q_{[H2O]}}{V})} \tag{S13}$$

Figure S 1 Potential energy surface for Cl + $HOCH_2CH_2Cl$ reaction

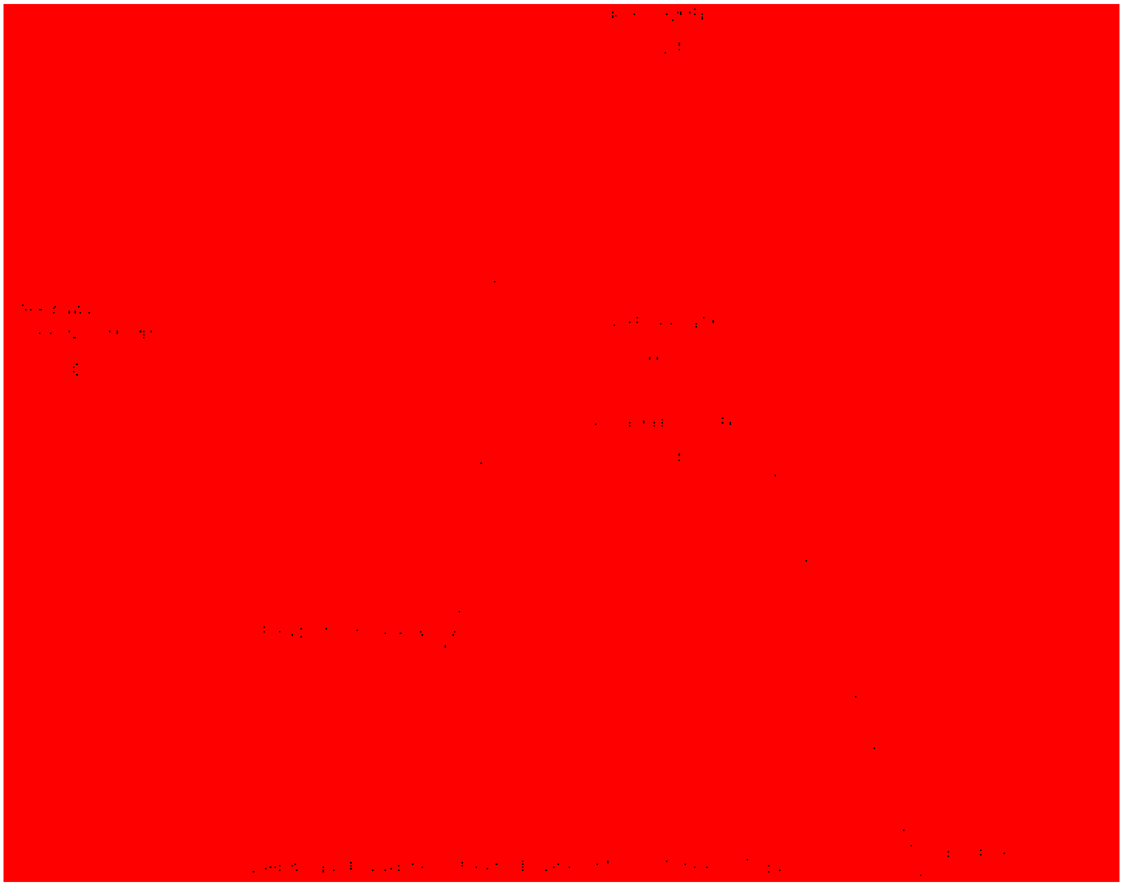

Figure S-1: Potential energy surface diagram for the reaction of Cl + $HOCH_2CH_2Cl$ calculated at MP2/6-311++G(3df,3pd). Energies reported in kcal mol^{-1}. The energies of both reactants (Cl and $HOCH_2CH_2Cl$), pre-reactive complex and transition states were optimized using the B3LYP/6-311++G(3df,3pd) method/basis set. Single point calculations were computed at the

MP2/6-311++G(3df,3pd) level for all species using the optimized geometry computed at the B3LYP/6-311++G(3df,3pd) level.

S-2 Calculation of concentrations of O_3, HO_2, β-HEP and β-HEP-H_2O from measured absorbances

From the Beer-Lambert Law, where b is pathlength, σ is absorption cross section, and [ ] indicates concentrations

$$A_{220} = b\begin{pmatrix} \sigma_{220}^{O_3}[O_3] + \sigma_{220}^{HO_2}[HO_2] + \sigma_{220}^{\beta-HEP}[\beta - HEP] + \\ \sigma_{220}^{\beta-HEP-H_2O}[\beta - HEP - H_2O] \end{pmatrix}$$

(S14)

$$A_{230} = b\begin{pmatrix} \sigma_{230}^{O_3}[O_3] + \sigma_{230}^{HO_2}[HO_2] + \sigma_{230}^{\beta-HEP}[\beta - HEP] + \\ \sigma_{230}^{\beta-HEP-H_2O}[\beta - HEP - H_2O] \end{pmatrix}$$

(S15)

$$A_{254} = b\begin{pmatrix}\sigma_{254}^{O_3}[O_3] + \sigma_{254}^{HO_2}[HO_2] + \sigma_{254}^{\beta-HEP}[\beta - HEP] + \\ \sigma_{254}^{\beta-HEP-H_2O}[\beta - HEP - H_2O]\end{pmatrix}$$

(S16)

Since the cross sections of the β-HEP-H_2O complex is unknown, we assume

$$\sigma_x^{\beta-HEP-H_2O} = f_x\, \sigma_x^{\beta-HEP} \quad \text{(S17)}$$

Where $f_x \geqslant 0$ and $x = 200 - 400$ nm.

Substituting Equation S17 into the last two terms of equation S14,15 and 16 yields,

$$\begin{matrix}\sigma_x^{\beta-HEP}[\beta - HEP] + \\ \sigma_x^{\beta-HEP-H_2O}[\beta - HEP - H_2O]\end{matrix} = \sigma_x^{\beta-HEP}[\beta - HEP] + f_x\, \sigma_x^{\beta-HEP}[\beta - HEP - H_2O]$$

(S18)

The equilibrium constant for the formation of the β-HEP-H_2O complex is,

$$K = \frac{[\beta - HEP - H_2O]}{[\beta - HEP][H_2O]}$$

Solving for β-HEP-H_2O gives,

$$[\beta - HEP - H_2O] = K[\beta - HEP][H_2O]$$

(S19)

Substituting Equation S19 into S18 yields,

$$\begin{matrix} \sigma_x^{\beta-HEP}[\beta - HEP] + \\ \sigma_x^{\beta-HEP-H_2O}[\beta - HEP - H_2O] \end{matrix} = \sigma_x^{\beta-HEP}[\beta - HEP] + f_x K \sigma_x^{\beta-HEP}[\beta - HEP][H_2O]$$

(S20)

Factoring out $\sigma_x^{\beta-HEP}[\beta - HEP]$ yields Equation S21

$$\begin{matrix} \sigma_x^{\beta-HEP}[\beta - HEP] + \\ \sigma_x^{\beta-HEP-H_2O}[\beta - HEP - H_2O] \end{matrix} = \sigma_x^{\beta-HEP}[\beta - HEP][1 + f_x K[H_2O]]$$

(S21)

Thus the equations for absorbance at 220, 230 and 254 reduce to,

$$A_{220} = b\left(\sigma_{220}^{O_3}[O_3] + \sigma_{220}^{HO_2}[HO_2] + \sigma_{220}^{\beta-HEP}[\beta - HEP]\{1 + f_{230}K[H_2O]\}\right)$$

(S22)

$$A_{230} = b\left(\sigma_{220}^{O_3}[O_3] + \sigma_{220}^{HO_2}[HO_2] + \sigma_{220}^{\beta-HEP}[\beta - HEP]\{1 + f_{230}K[H_2O]\}\right)$$

(S23)

$$A_{254} = b\left(\sigma_{220}^{O_3}[O_3] + \sigma_{220}^{HO_2}[HO_2] + \sigma_{220}^{\beta-HEP}[\beta - HEP]\{1 + f_{254}K[H_2O]\}\right)$$

(S24)

If, $0 \leq f_{220}, f_{230}, f_{254} \leq 10$, the product of $f_{220}K[H_2O], f_{230}K[H_2O], f_{254}K[H_2O] \approx 0$. Thus the observed β-HEP concentration in this experiment is,

$$[\beta - HEP]_{observed} = [\beta - HEP][1 + f_xK[H_2O]] \approx [\beta - HEP]$$

(S25)

If f_x=0, the two cross sections do not overlap and the observed signal in this experiment is only due to β-HEP. If $f_x > 0$ there is an overlap between the two cross sections and the observed signal in this experiment is due to both β-HEP and β-HEP-H_2O complex. In either case, the equations to solve for the concentrations of ozone, β-HEP and HO_2 reduce to

$$A_{220} = b\left(\sigma_{220}^{O_3}[O_3] + \sigma_{220}^{HO_2}[HO_2] + \sigma_{220}^{\beta-HEP}[\beta - HEP]\right)$$

(S26)

$$A_{230} = b\left(\sigma_{230}^{O_3}[O_3] + \sigma_{230}^{HO_2}[HO_2] + \sigma_{230}^{\beta-HEP}[\beta - HEP]\right)$$

(S27)

$$A_{254} = b\left(\sigma_{254}^{O_3}[O_3] + \sigma_{254}^{HO_2}[HO_2] + \sigma_{254}^{\beta-HEP}[\beta - HEP]\right)$$

(S28)

The HO_2 concentration calculated by solving equation S26, 27, 28 was always below our detection limit of 1×10^{13} molecules/cm^3. Thus the general form of the measured absorbance is given by Equation 1 in the paper

$$A_x = b\,(\sigma_x^{O_3}[O_3] + \sigma_x^{\beta-HEP}[\beta - HEP])$$

Equation 1

S-3 Kinetic Equations

To derive Equation 2, we define the following variables

Concentration of un-complexed [β-HEP] = $[u]$

Concentration of complexed β-HEP [β-HEP-H_2O] = $[c]$

Concentration of observed β-HEP = $[o]$

Concentration of water = $[w]$

Observed rate constant = k_o

From elementary reactions 3 and 5, the rate of loss of un-complexed β-HEP is given by

$$\frac{d[u]}{dt} = -2k_3[u]^2 - k_5[u][c] \tag{S29}$$

From elementary reactions 5 and 6, the rate of loss of β-HEP-H_2O is given by

$$\frac{d[c]}{dt} = -k_5[u][c] - 2k_6[c]^2 \tag{S30}$$

To obtain k_3,k_5 *and* k_6 as functions of k_o we introduce the relationship,

$$\frac{d[o]}{dt} = -2k_o[o]^2$$

(S31)

Substituting equation S25 (the observed concentration of β-HEP in our experiment) in equation S31 yields,

$$\frac{d[o]}{dt} = -2k_o([u][1 + fK[w])^2$$

$$= -2k_o[u]^2([1 + fK[w])^2$$

(S32)

Adding Equations S-29 and S-30 gives the theoretically observed loss of β-HEP in this experiment

$$\frac{d[o]}{dt} = \frac{d[u]}{dt} + \frac{d[c]}{dt} = -2k_3[u]^2 - 2k_5[u][c] - 2k_6[c]^2$$

(S33)

Equating S-32 and S-33 gives,

$$-2k_o[u]^2([1+fK[w])^2 = -2k_3[u]^2 - 2k_5[u][c] - 2k_6[c]^2$$

(S34)

The equilibrium constant for complex formation is given by

$$K = \frac{[c]}{[u][w]}$$

Thus, $$[c] = K[u][w]$$ (S35)

Substituting Equation S-35 into Equation S34 gives,

$$-2k_o[u]^2([1+fK[w])^2 = -2k_3[u]^2 - 2k_5[u]^2K[w] - 2k_6[u]^2[w]^2K^2$$

(S36)

Dividing Equation S36 by -2$[u]^2$ on both sides yields,

$$k_o([1 + fK[w])^2 = k_3 + k_5[u]K[w] + k_6[u]^2[w]^2K^2$$

Solving for k_o gives,

$$k_o = \frac{k_3 + k_5[u]K[w] + k_6[u]^2[w]^2K^2}{([1 + fK[w])^2}$$

(S37)

From calculated values of the equilibrium constant (Figure 8) and the slopes of the experimental data (Figure 7), $k_6[u]^2[w]^2K^2 << k_3 + k_5[u]K[w]$. Further within the uncertainty, there is no evidence for curvature in data in Figure 7.

Also, if $f = 1$ the cross section of β-HEP and the complex are equal then $1 + fK[w] \approx 1$. If $f = 0$ the cross section of β-HEP and the complex are distinguishable, then $1 + fK[w] = 1$. In either case Equation S -37 reduces to Equation 2 in the manuscript as,

$$k_o = k_3 + k_5K[w]$$

Equation 2

S-4 Derivation of Equation 3

Following is the derivation of equation of Equation 3 from Equation 2

$$k_o = k_3\{1 + \frac{k_5}{k_3} K\ [w]\}$$

(S38)

From the Arrhenius expression for the temperature dependence of the rate coefficients and van't Hoff equation for the temperature dependence of the equilibrium constant,

$$k_3 = A_3 e^{\left(\frac{-E_3}{RT}\right)}$$

(S39a)

$$k_5 = A_5 e^{\left(\frac{-E_5}{RT}\right)}$$

(S39b)

$$K = C * e^{\left(\frac{-\Delta H}{RT}\right)}$$

(S39c)

Substituting S-39a, S39b, S39c into Equation S-38 gives,

$$k_o = k_3\{1 + \frac{A_5 e^{\left(\frac{-E_5}{RT}\right)}}{A_3 e^{\left(\frac{-E_3}{RT}\right)}} C e^{(\frac{-\Delta H}{RT})}[w]\}$$

$$k_o = k_3\{1 + \frac{A_5 * C}{A_3} e^{(\frac{-(\Delta H + E_5 - E_3)}{RT})}[w]\}$$

(S40)

Combining parameters, A_5C/A_3 = A and (E_5+ΔH-E_3)= E reduces Equation S40 to Equation 3 in the manuscript.

$$k_o = k_3\,\{1 + Ae^{(\frac{-E}{RT})}[w]\}$$

Equation 3